Modulation of atrial fibrillation susceptibility by gp91^{phox}-containing NADPH oxidase

Alexandra S. Mighiu

Jesus College

Department of Cardiovascular Medicine

A thesis submitted for the degree of

Doctor of Philosophy in Cardiovascular Medicine

University of Oxford

Trinity Term 2018

Acknowledgements

The work presented in this thesis would not have been possible without the advice and support of a number of colleagues, collaborators, and mentors. First and foremost, I would like to acknowledge my primary academic supervisor, Barbara Casadei. I am extremely grateful for the opportunity to come to Oxford and for the continued support and encouragement. A special thank you to my second supervisor, Dr Jillian Simon, who has been an outstanding source of encouragement and direction. Thank you for being generous with your time, sharing your knowledge and expertise, and motivating me to the end.

My time in Oxford was also made memorable by a few wonderful individuals who have now become dear friends. Thank you for making the lab and Oxford a great place to be. Special thanks to Klemen Ziberna, for being a tremendous source of insight and for the bottomless coffee.

I would also like to acknowledge the Radcliffe Department of Medicine Scholars Programme and the Clarendon Fund for supporting me during this work, as well as the British Heart Foundation for supporting this research. Thank you also to Jesus College for the generous scholarships and travel allowances, which have greatly enriched my doctoral training experience.

Above all, my deepest thanks to my family. To my sister Patricia, thank you for being there for me through everything and for being an endless source of friendship. Mom and dad, you have given me the opportunity to accomplish so much. I am forever grateful for your love, patience, encouragement, and unwavering support.

Abstract

Modulation of atrial fibrillation susceptibility by gp91^{phox}-containing NADPH oxidase
Thesis submitted for the degree of DPhil in Cardiovascular Medicine
Michaelmas Term 2018

Alexandra S. Mighiu
Jesus College
Department of Cardiovascular Medicine, University of Oxford

Atrial fibrillation (AF) is the most frequently encountered cardiac rhythm disorder in humans, with affected individuals facing an increased risk of stroke and mortality. Published findings implicate oxidative stress in triggering the new onset of AF and in promoting the atrial electrical and structural changes that drive disease progression. NOX2-containing NADPH oxidases are a significant source of superoxide production in atrial tissues. Previous work showed that a NOX2-mediated increase in superoxide accompanies AF in patients and animal models of tachypacing-induced AF, and further reported a strong independent association between atrial NOX2 activity and post-operative AF in patients undergoing cardiac surgery. However, a direct causal role for NOX2 in AF has not been investigated. This thesis aimed to test the hypothesis that superoxide released specifically from NOX2 directly contributes to the development of AF.

To investigate the role of NOX2 in AF, mice with cardiac-specific overexpression of the human *NOX2* gene (NOX2-Tg) were characterized. Atrial homogenates from these mice were found to show approximately 3-fold higher expression of NOX2 protein compared with wild-type controls, which was associated with a significant increase in NADPH-stimulated superoxide production. AF susceptibility assessed *in vivo* by transesophageal atrial burst stimulation was significantly higher in NOX2-Tg mice compared with wild-type, in the absence of significant alterations in cardiac function. However, dietary administration of atorvastatin (30 mg/kg daily for two weeks) did not eliminate AF susceptibility in NOX2-Tg mice, despite preventing the increase in NADPH-stimulated superoxide production in the left and right atria of these animals. Instead, atorvastatin significantly reduced the duration of pacing-induced AF, an effect which was found to be independent of genotype, and thus independent of NOX2 inhibition.

Mechanistic studies do not support a role for NOX2 in promoting electrical or structural remodelling, as high-resolution optical mapping of di-4-ANEPPS-stained atrial tissue preparations revealed no significant differences in action potential duration or conduction velocity between wild-type and NOX2-Tg mice. Instead, NOX2 overexpression was associated with impaired atrial Ca^{2+} handling. In left atrial myocytes of NOX2-Tg mice, the RyR2 Ca^{2+} leak-SR load ratio was lower when compared with wild-type, despite an increase in SR Ca^{2+} load. In the right atria, the leak-load ratio was similar between NOX2-Tg and wild-type myocytes, but the proportion of myocytes with ‘leaky’ RyR2 channels was greater among NOX2-Tg mice. RyR2 phosphorylation at Ser-2814 and Ser-2808 was not significantly different between WT and NOX2-Tg atrial homogenates, indicating that the changes in diastolic leak are not caused by differences in CaMKII or PKA activity.

Contents

List of Figures

List of Tables

List of Abbreviations

2-OHE	2-hydroxyethidium
AF	Atrial fibrillation
Ang-II	Angiotensin II
ANOVA	Analysis of variance
AP	Action potential
APD	Action potential duration
ATV	Atorvastatin
BSA	Bovine serum albumin
BPM	Beats per minute
$[Ca^{2+}]_i$	Ca^{2+} concentration, intracellular
$[Ca^{2+}]_o$	Ca^{2+} concentration, extracellular
$[Ca^{2+}]_{SR}$	Ca^{2+} concentration, sarcoplasmic reticulum
CaMKII	Ca^{2+}/Calmodulin kinase type 2
Ct	Cycle threshold
CTGF	Connective tissue growth factor
CV	Conduction velocity
DCF	Dichlorofluorescein
DHE	Dihydroethidium
DNA	Deoxyribonucleic acid
DPI	Diphenyleneiodonium
E	Ethidium
ECG	Electrocardiogram
GAPDH	Glyceraldehyde 3-phosphate dehydrogenase
GSH	Glutathione
GSSG	Glutathione disulfide
GTP	Guanosine triphosphate
EF	Ejection fraction
FS	Fractional shortening
HEPES	4-(2-hydroxyethyl)-1-piperazine-ethane sulfonic acid
HPLC	High performance liquid chromatography
H_2O_2	Hydrogen peroxide
I_{CaL}	L-type Ca^{2+} current
I_{K1}	Background K^+ current
I_{Kr}	Rapidly-activating delayed rectifier K^+ current
I_{Ks}	Slowly-activating delayed rectifier K^+ current
I_{Kur}	Ultra-rapid delayed rectifier K^+ current
I_{Na}	Na^+ current
I_{NCX}	Na^+/Ca^{2+} exchange inward current
IVCT	Isovolumetric contraction time
IVRT	Isovolumetric relaxation time
LA	Left atria
LDL	Low-density lipoprotein

LV	Left ventricle
NADPH	Nicotinamide adenine dinucleotide phosphate
NO	Nitric oxide
NOS	Nitric oxide synthase
NOX	NADPH oxidase
NOXA1	NADPH oxidase activator 1
NOXO1	NADPH oxidase organiser 1
$O_2^{\bullet -}$	Superoxide
OH-	Hydroxyl radical
ONOO-	Peroxynitrite
PBS	Phosphate buffered saline
PBST	Phosphate buffered saline – Tween 20
PCR	Polymerase chain reaction
PKA	Protein kinase A
PLN	Phospholamban
qRT-PCR	Quantitative reverse transcription polymerase chain reaction
SD	Standard deviation
SERCA	Sarcoplasmic/endoplasmic reticulum Ca^{2+} ATPase pump
SH3	SHC homology domain 3
SR	Sinus rhythm
RA	Right atria
RNA	Ribonucleic acid
ROS	Reactive oxygen species
RyR	Ryanodine receptor Ca^{2+} release channel
TBS	Tris buffered saline
TBST	Tris buffered saline – Tween 20
Tg	Transgenic
TGF-β	Transcription growth factor β
TNF-α	Tumour necrosis factor α
WT	Wild-type
XOR	Xanthine oxidoreductase

1 Introduction

Cardiac rhythm is initiated and regulated by a specialized group of cells within the sinoatrial (or sinus) node, the primary cardiac pacemaker, that generate spontaneous electrical activity [1-3]. Electrical impulses are then propagated sequentially and uniformly through the atria, the atrioventricular node, and the ventricles by the cardiac conduction system [2, 3]. The sequential propagation of this electrical signal ensures rhythmic and coordinated contractions of the atria and ventricles, and is essential for proper cardiac function and efficient pumping of blood through the circulation to meet the body's metabolic needs. Any significant perturbations to this tightly regulated process can lead to dyssynchronous and irregular cardiac contractions which are broadly referred to as cardiac arrhythmias.

Among the most common, atrial fibrillation (AF) is a disorder that occurs when electrical conduction in the heart does not solely arise from the sinus node, but instead originates spontaneously from sites around the atria, leading to disordered conduction and a rapid and irregular heart rhythm [2, 4]. The precise mechanisms underlying AF are complex but fundamentally involve atrial remodelling that generates ectopic *triggers* and vulnerable tissue *substrates* which act to maintain disorganized atrial conduction patterns. Investigations into the biological pathways driving the disease process have suggested that oxidative stress, an imbalance between the production of reactive oxygen species and anti-oxidant defenses [5], likely plays a role in AF. In particular, the NOX2-containing NADPH oxidase has emerged as a major initiating source for increased reactive oxygen species production in AF. This chapter summarizes the fundamentals of AF pathophysiology as well as how alterations in atrial redox signalling may be involved in the development and maintenance of the arrhythmia.

1.1 Atrial Fibrillation

1.1.1 Clinical Features

AF is a supraventricular tachyarrhythmia characterized by rapid, uncoordinated atrial electrical activity, which in turn causes ineffective contractions of the atria [6]. On an electrocardiogram (ECG), this manifests in the absence of distinct regular P waves, irregular atrial activity (rapid oscillations or fibrillatory waves), and irregular R-R intervals (when atrioventricular conduction is not compromised) [2]. The appreciation for the progressive nature of AF has led to its classification based on duration and response to treatment and falls into four general categories: paroxysmal (intermittent), persistent, long-standing persistent, and permanent [7, 8]. AF often presents first in a paroxysmal form, defined as recurrent arrhythmic episodes (two or more) that are terminated, either spontaneously or by direct-current electrical cardioversion, in less than seven days and usually within 48 hours [7-9]. Persistent AF describes episodes that last longer than seven days and are only terminated by pharmacological therapy or electrical cardioversion while long-lasting persistent classifies continuous AF lasting more than one year, at which point a rhythm control treatment strategy is adopted. Permanent AF, which is irreversible, shows no response to either medication or cardioversion [7, 8].

Further classification can be made on the basis of the underlying condition: AF secondary to structural heart disease (AF in patients with left ventricular systolic or diastolic dysfunction, long-standing hypertension, or other structural heart disease), polygenic (AF in carriers of common gene variants associated with early onset AF), post-operative (AF in patients after major surgery, typically cardiac, who were in sinus rhythm prior to surgery and had no history of AF), valvular AF (AF in patients with mitral valve stenosis or after mitral valve surgery), and monogenic (AF in patients with inherited cardiomyopathies and channelopathies) [7].

1.1.2 Epidemiology, Predisposing Conditions and Complications

AF is the most commonly encountered arrhythmia affecting 1.0 - 1.5% of the general population [10, 11]; worldwide data estimates that approximately 20.9 million men and 12.6 million women are currently living with AF [12, 13]. Older age is a strong risk factor for the disorder, with prevalence increasing from approximately 1% among adults <60 years of age to up to 12% of adults aged >75 to 80 years [14, 15]. The global prevalence of AF is expected to double or triple within the next two or three decades [15, 16], which can be partially attributed to an ageing population as well as the growing burden of obesity, diabetes, coronary artery disease, hypertension and heart failure – all risk factors for AF [17, 18].

In addition, AF contributes significantly to population morbidity and mortality. Patients with AF generally experience more hospital admissions [19] and a lower quality of life [20-22] than those who do not have the arrhythmia. Affected individuals also face a number of serious complications among which are a four- to five-fold increased risk of stroke [23, 24] and a two- to three-fold increased risk of heart failure [25]. It has been suggested that the absence of synchronized atrial contraction during AF enables blood to pool and form thromboemboli, accounting for approximately 20-25% of all thromboembolic strokes [26]. The rapid and irregular ventricular rate during AF also makes the heart less efficient which can promote *de novo* heart failure [27]. Incident AF is also associated with a nearly two-fold increased risk of mortality in women and a 1.5-fold increase in men, even among asymptomatic cases of the disorder [28-30].

1.1.3 Pathophysiology of Atrial Fibrillation

1.1.3.1 Atrial Cellular Electrophysiology

The initiation and coordinated contraction of the myocardium is maintained by the orderly propagation of electrical signal called action potentials, which activate (depolarize) individual cardiomyocytes and stimulate contraction through a process called excitation-contraction coupling [31]. The morphology of the action potential depends on the expression and biophysical properties

of mainly voltage-gated ion channels located in the outer membrane (sarcolemma) of individual cardiomyocytes (reviewed in [32] and [33]). The sequential opening, inactivation, and closure of a series of ion channels gives rise to 5 distinct phases of the action potential (numbered 0-4). In a typical human atrial myocyte, activation (phase 0) occurs when action potentials propagated from neighbouring cells depolarize the cardiomyocyte to the threshold potential of voltage-gated Na^+ channels (the potential at which the conformation of the channel changes from a closed to an open state [34]), causing a rapid influx of Na^+. This large inward Na^+ current (I_{Na}) further depolarizes the cell (to between +30 mV and +40 mV) and marks the beginning of a new action potential. Phase 1, early repolarization, occurs immediately after the peak of depolarization; Na^+ channels are inactivated and the activation of both the transient outward K^+ current (I_{to}) [35] and the ultra-rapid delayed rectifier K^+ current (I_{Kur}) (unique to atrial myocytes [36]) generates a small downward deflection in the action potential waveform.

The action potential plateau (phase 2) follows and is maintained by a balance between an inward Ca^{2+} current (I_{CaL}) through the L-type Ca^{2+} channel and outward K^+ currents (largely driven by the rapidly-activating delayed rectifier K^+ (I_{Kr}) current). Finally, phase 3 represents repolarization and occurs when the outward K^+ current outweighs the inward current (due to inactivation of the L-type Ca^{2+} channel) thereby bringing the membrane potential to rest (phase 4). The two main repolarizing K^+ currents that sum to terminate the plateau phase and initiate final repolarization are I_{Kr} and a slowly-activating delayed rectifier K^+ current (I_{Ks}). Under normal conditions, the resting membrane potential of cardiomyocytes is negative; it is stabilized between -65 mV and -80 mV predominantly by the inward rectifier K^+ background current (I_{K1}), with contributions from the electrogenic Na^+/Ca^{2+} exchanger (NCX) and the Na^+/K^+-ATPase pump.

The major ionic currents depicted above are common for both human and mouse atrial myocytes (reviewed in ref. [37]); however several differences contribute to the variation in action potential morphology and duration (hundreds *vs* tens of milliseconds) between the two species. For example, despite sharing similar current-voltage relationships, the magnitude of I_{CaL} is reduced in mouse atrial myocytes [38], partly accounting for the less prominent plateau phase than observed in human cells [39]. Mouse atrial myocytes also have two additional voltage-gated K^+ currents:

$I_{K,slow}$, which is rapidly activating and slowly inactivating, and I_{ss}, a Ca^{2+}-independent, depolarization-activated slowly activating current important in late repolarization [40, 41].

The opening of L-type Ca^{2+} channels during the action potential leads to a small influx of Ca^{2+} into the cell that serves as a signal for the opening of specialized Ca^{2+}-sensitive channels called ryanodine receptors (RyR, with type 2 (RyR2) as the predominant isoform in cardiac cells) located within the membrane of the sarcoplasmic reticulum (SR, intracellular Ca^{2+} store) [31]. This causes a much larger release of Ca^{2+}, via a process called *Ca^{2+}-induced Ca^{2+} release* [43], that drives Ca^{2+}-troponin binding and initiates mechanical contraction of the cell. Diastole is initiated by the re-uptake of Ca^{2+} into the SR by a Ca^{2+} pump, the sarco/endoplasmic reticulum Ca^{2+} ATPase (SERCA, with SERCA2a as the cardiac isoform), and its extrusion across the sarcolemma via NCX in order to balance the cytosolic Ca^{2+} load. SERCA activity is regulated by the inhibitory protein phospholamban (PLN), where PLN phosphorylation facilitates SR Ca^{2+} uptake.

In ventricular myocytes, Ca^{2+}-induced Ca^{2+} release is facilitated by the presence of an extensive network of membrane invaginations (transverse tubular network, t-tubules) that brings the L-type Ca^{2+} channels in close proximity (within ~10 nm) to RyR2 channels, creating functional domains known as 'dyadic' clefts [44]. It is estimated that ~100 RyR2 channels are associated with 10-25 L-type Ca^{2+} channels within the dyadic cleft to form a 'couplon' (local SR Ca^{2+} release unit). The activation of spatially discrete clusters of RyR2 (~6-20) produces local Ca^{2+} transients, called Ca^{2+} sparks (elementary units of Ca^{2+} release) [45]. Whole-cell Ca^{2+} transients are then produced when the spatial and temporal summation of multiple Ca^{2+} sparks causes a global increase in the cytoplasmic Ca^{2+} concentration ($[Ca^{2+}]_i$).

In small mammals, atrial myocytes are somewhat different in structure and therefore show a different pattern of Ca^{2+} release (reviewed in refs. [46] and [47]). In contrast to ventricular cells, the t-tubule network in the atria is far less complex or entirely absent (depending on the species) [48-50]. As a consequence, atrial cells have two distinct populations of SR Ca^{2+} stores (and therefore RyR2 populations [51]), junctional (which are adjacent with the sarcolemma) and non-junctional (located deeper within the cell), that produce spatially inhomogeneous Ca^{2+} release. At the junctional SR, RyR2 channels are in close proximity with L-type Ca^{2+} channels creating distinct

Ca^{2+} release units (spaced ~2 μm apart [52]) similar to the couplons described in ventricular cells. Upon membrane depolarization, junctional RyR2 channels become activated and $[Ca^{2+}]_i$ increases along the periphery without any rise of $[Ca^{2+}]_i$ in the centre of cell. Diffusion of Ca^{2+} away from these peripheral sites activates non-junctional RyR channels deeper inside the myocyte and causes additional Ca^{2+} release from central regions of the cell, eventually producing a global Ca^{2+} transient [53].

1.1.3.2 Electrophysiological Mechanisms of AF

AF occurs when the normal electrophysiology of the atrial myocardium is perturbed. Experimental evidence supports three possible patterns of impulse conduction/propagation that initiate and/or sustain the arrhythmia [4]. First, rapidly firing atrial ectopic foci (triggers) may be present, with irregular conduction towards the rest of the atria. Secondly, a single primary re-entry circuit (or rotor) may produce local activation with fibrillating conduction causing AF. Alternatively, a *multiple wavelet theory* was proposed, according to which multiple simultaneous re-entry circuits lead to fibrillation [54].

1.1.3.2.1 Atrial Ectopic Activity

Broadly defined, ectopic foci are groups of excitable cells outside the sinoatrial node region that acquire the ability to generate spontaneous action potentials [2]. As early as 1896, Engelman [55] suggested that individual cardiac muscle fibers could generate spontaneous activity and proposed the *hyperectopia* theory, which posited that AF could be maintained by multiple self-sustaining foci of triggered activity. Shortly thereafter, Winterberg [56] proposed that a single rapidly-firing ectopic focus underlies AF (*tachysystole* theory). It was not until several decades later that triggered activity, in particular originating from the pulmonary veins, was observed in AF patients and shown to play a prominent role in initiating the arrhythmia. Using intracardiac mapping of the left atrium and pulmonary veins in a cohort of 45 patients, Haissaguerre *et al.* [57] were able to localize the origin of ectopic beats to the pulmonary veins. In a majority of patients,

the ectopic foci were capable of initiating frequent bouts of AF; importantly, radiofrequency ablation could terminate up to 90% of these episodes. Other non-pulmonary ectopic beats have also been observed near the coronary sinus, the superior vena cava, the crista terminalis, and the interatrial septum [58-60].

Triggered activity is believed to arise from *afterdepolarizations*, abnormal membrane depolarizations that can provoke new action potentials if they reach the threshold voltage of depolarizing currents [42]. Those occurring after full repolarization of a normal action potential are referred to as *delayed* afterdepolarizations, while *early* afterdepolarizations describe abnormal membrane oscillations that occur during the repolarization phase of a prolonged action potential (typically at the end of phase 2 or early in phase 3 of the action potential) [42, 61]. Delayed after-depolarizations are favoured by conditions that produce a diastolic rise in $[Ca^{2+}]_i$ and activate an inward NCX (I_{NCX}) current: the exchange of intracellular Ca^{2+} for extracellular Na^+ (which occurs in a 3:1 ionic ratio) generates a net inward movement of positive ions that can trigger a new action potential [61, 62]. Early after-depolarizations are caused by increases in inward currents (*e.g.*, I_{CaL} or I_{Na}) or reduced outward currents (*e.g.*, I_K) that prolong repolarization allowing I_{CaL} to recover from inactivation and produce an additional inward 'window' current [63]. Because of overlapping voltage thresholds for inactivation and activation, L-type Ca^{2+} channels are able to undergo rapid transformations from inactivated to closed and open states, such that a fraction of channels that are inactivated during the plateau can re-open and allow Ca^{2+} to enter [63, 64].

1.1.3.2.2 Re-entry

Re-entry is a disorder of impulse propagation that permits a wave of excitation to travel repeatedly around a closed circuit. The earliest demonstration of this phenomenon was provided in 1906 by Mayer in experiments using a ring-like preparation of muscle cut from the jellyfish *Cassiopea xamachana* [65]. He showed that by applying electrical pulses to these rings, a wave could be induced to propagate continuously in one direction around a distinct anatomical structure. Shortly thereafter, Mines [66] observed similar effects in rings of dog cardiac tissue and

formulated the concept of *circus movement re-entry*, according to which a single excitation wave drives fibrillation. For re-entry to occur, the speed of a propagating wave must be slow enough to allow sufficient time for the tissue ahead of it in the circuit to recover from its refractory period so that it can be re-excited. Therefore, both the refractory period and the conduction velocity of the wavefront (*e.g.*, the speed of a propagating action potential) determine the likelihood of re-entry. The product of the refractory period and conduction velocity, known as the wavelength, then determines the distance travelled by the wave during one refractory period. If the wavelength is smaller than the physical dimensions of the atria then an "excitable gap" is produced and re-entry can occur.

Re-entry also requires an area of unidirectional block within the tissue. This area of unexcitable tissue can be created by fixed anatomical obstacles, as originally postulated by Mines [66] and Mayer [65], or functional obstacles (due to depolarization). Allessie *et al.* [67] were the first to demonstrate *functional re-entry* in rabbit left atrial tissue without anatomical barriers. The investigators applied premature extra-stimuli to induce atrial tachycardia in the tissue preparations and then recorded the electrical activity near the centre of the re-entry circuit. Recordings in the central region showed only sub-threshold responses, effectively making the tissue unexcitable. According to this model, the tissue at the centre of the circulating wave is maintained in a refractory state due to electrotonic effects and consequently, electrical activity rotates around this region. These 'rotors' have been proposed to be the major drivers of fibrillation in this model. Subsequent studies of functional re-entrant rhythms led to the notion of spiral waves, which are smaller waves of excitation emitted by the rotor that propagate into nearby cardiac muscle and give rise to turbulent electrical activity [68].

Finally, the *multiple wavelet* theory of re-entry was proposed by Gordon Moe [54] to try and explain both the chaotic nature of AF as well as the fact that AF often persists for a long time (months or years). According to his theory, AF is maintained by multiple waves of depolarization with continuously changing trajectories. Computer simulations demonstrated that individual waves interact with each other and break to produce new wavelets, regions of conduction block, and chaotic activation patterns [69]. Using high-resolution electrode mapping, Allessie *et al*. [70] were

able to demonstrate the presence of multiple waves *in vivo*. In their experiments, AF was induced in canine atria in the presence of acetylcholine and up to 6 wavelets were observed to sustain the arrhythmia. Subsequent studies from the same group of investigators mapped electrical patterns during AF in humans and observed up to three different wavelets that meandered through the atria in response to regional conduction block [71]. Moe's original mathematical model also predicted that changes in refractoriness, conduction velocity, and heterogeneities of membrane properties and atrial structure played dominant roles in the stability of multiple wavelets [69].

1.1.3.3 Molecular Mechanisms of AF

The abnormal patterns of atrial impulse formation and/or propagation described above are not mutually exclusive. In reality, multiple mechanisms likely co-exist in an individual patient depending on the degree of irreversible changes to the underlying tissue substrate. These changes, termed *atrial remodelling*, occur at the cellular/molecular level and include: 1) alterations in the expression and/or function of ion channels, 2) changes in atrial architecture, and 3) abnormalities in calcium handling, described in detail below.

1.1.3.3.1 Electrical remodelling and refractoriness

Electrical remodelling consists of molecular changes (typically to ion channel currents) that shorten the wavelength required for a re-entry circuit to occur. The hallmark feature of electrical remodelling in AF is a shortening of the atrial effective refractory period (synonymous with the action potential duration (APD) of individual cardiomyocytes) that facilitates the progression of paroxysmal to persistent AF. In their seminal study, Wijffels *et al.* [72] began to outline the electrophysiological changes of the atrial myocardium during AF using a goat model of rapid atrial pacing. When short bursts of electrical stimulation were applied, AF episodes could be initiated but were terminated spontaneously within seconds. However, when AF was repetitively re-induced, the episodes of AF gradually became longer until they no longer self-terminated. The progression from short self-terminating episodes of AF to chronic AF was accompanied by a reduction in the

APD (as much as 45%) [72]. A reversion of the physiological rate adaptation was also noted. Importantly, an abbreviation of the action potential is often observed in human AF, where patients with persistent AF have shorter atrial APD compared with patients in normal sinus rhythm [73-75].

As mentioned previously, the duration of the action potential is determined by the balance between inward currents (primarily Ca^{2+}, which tend to keep the cell depolarized) and outward currents (primarily K^+, which repolarize the cell). In right atrial myocytes from persistent AF patients, there is a significant reduction in the density of I_{CaL} [39, 76] with a corresponding decrease in the mRNA [77-80] and protein content of the α1 pore-forming subunit [77, 80]. As a result, decreased I_{CaL} shortens the APD and creates a substrate for re-entrant AF. Changes in the activity of protein phosphatases (protein phosphatase type 2A [81], calcineurin [82]) and kinases (src type tyrosine kinases [83]), as well as post-translational modifications [84], have also been documented and may contribute to the reported reduction in I_{CaL}.

Among the repolarizing K^+ currents, AF-associated changes include increases in I_{K1} [85] and reductions in I_{to} and I_{Kur} [86, 87]. Increased I_{K1} density parallels the increase in both mRNA and protein expression of Kir2.1, the α-subunit of the channel complex [85]. According to computer simulations of 2-dimensional human atrial cell preparations, increases in I_{K1} are predicted to shorten the action potential and stabilize rotors [88]. A gain of function mutation in Kir2.1 has also been described in patients with familial AF and further supports a role for increased I_{K1} in AF pathogenesis [89]. Furthermore, downregulation of I_{to} has been consistently reported in AF patients [75, 90, 91] and animal models of AF-induced remodelling [86], the impact of which is a higher plateau voltage and markedly prolonged APD at late repolarization [41]. I_{Kur} plays a significant role in atrial, but not ventricular, repolarization and both the amplitude and current density are reduced in right atrial myocytes of chronic AF patients compared with sinus rhythm [87].

1.1.3.3.2 Structural remodelling and conduction disturbances

Atrial structural changes that promote AF include interstitial fibrosis, inflammation, and hypertrophy and are commonly observed in AF patients with underlying structural heart disease (*e.g.,* heart failure, cardiomyopathy) and as a consequence of AF itself [92]. In particular, tissue fibrosis (the excessive accumulation of extracellular matrix proteins in the interstitial space [92]) features prominently in AF [93, 94]. Increased collagen deposition has been observed in atrial biopsies from AF patients [95, 96] and correlates with both post-operative AF [97] and the frequency of AF recurrence [98, 99]. Moreover, mice with cardiac overexpression of constitutively active transforming growth factor-β1 (TGF-β1) develop selective atrial interstitial fibrosis which increases the sensitivity to AF by transesophageal burst pacing [100, 101].

These structural abnormalities are accompanied by conduction disturbances in the atrial tissue. For instance, atrial fibrosis in TGF-β transgenic hearts reduces conduction velocity in the right atria and heterogeneously alters impulse conduction in the left atria [101]. In a canine model of heart failure-induced AF (ventricular tachypacing model), interstitial fibrosis was shown to create discrete regions of conduction slowing and promote conduction heterogeneity [102]. Disorganized collagen fibrils distributed between myocyte bundles are thought to disrupt cell-to-cell coupling by increasing the membrane resistance between adjacent myocytes [103]. Consequently, conduction is slowed and propagation becomes extremely complex and non-uniform which creates an environment suitable for unidirectional conduction and re-entry in small circuits [103, 104].

Further structural changes include gap junction remodelling. These are clusters of intercellular channels (composed of six connexins, with connexins 40 (Cx40) and 43 (Cx43) forming gap junction in cardiomyocytes [105]) that are localized at the intercalated discs of individual myocytes and are critical for anisotropic impulse conduction in cardiac tissue. There is evidence that these channels undergo significant remodelling in experimental [106, 107] and clinical AF [108, 109]. For instance, Cx40 and Cx43 expression is reduced in atrial samples of patients with persistent AF and heterogeneously re-distributed to lateral margins of myocytes

instead of being confined to the intercalated discs [110]. By decreasing electrical coupling between cells, these changes are accompanied by slowed and heterogeneous impulse conduction, key determinants of re-entrant AF.

1.1.3.3.3 Ca^{2+}-handling abnormalities and triggered activity

In addition to the reduction of I_{CaL}, AF-induced atrial remodelling has direct effects on intracellular Ca^{2+} homeostasis [4]. Abnormalities in Ca^{2+} handling promote spontaneous diastolic Ca^{2+} release from SR stores which enhances NCX-mediated Ca^{2+} extrusion in favour of an afterdepolarization-generating inward current [111] and are commonly observed in both animal models of AF [112, 113] as well as patients with AF [111, 114]. Spontaneous diastolic SR Ca^{2+} release has been attributed to an increase in RyR2 Ca^{2+} sensitivity or to an increase in SR Ca^{2+} content (high SR $[Ca^{2+}]_i$ has a stimulatory effect on RyR activity [115]) both of which increase the propensity of the channels to open [116, 117]. An increase in SR Ca^{2+} content has been described in atrial myocytes from paroxysmal AF patients [118] as well as canine models of congestive heart failure-related AF [119], and seems to be mediated by hyper-phosphorylation of PLN (inhibitor of SERCA in its dephosphorylated state) which enhances local Ca^{2+} uptake by SERCA.

RyR2 Ca^{2+} sensitivity is modulated by receptor phosphorylation (as well as other post-translational modifications), with hyper-phosphorylation increasing Ca^{2+} sensitivity and spontaneous release. Notably, RyR2 hyper-phosphorylation caused by protein kinase A (PKA) and/or Ca^{2+}/calmodulin-dependent protein kinase type II (CaMKII) has been observed in AF patients and experimental animal models of AF. CaMKII-dependent phosphorylation of RyR2 is increased in patients with chronic AF and is associated with increased RyR2 open probability and more spontaneous Ca^{2+} sparks during diastole [111]. Likewise, mice with RyR2 gain of function mutations that promote hyper-phosphorylation by CaMKII develop spontaneous Ca^{2+} release events independent of SR Ca^{2+} load and are more susceptible to burst pacing-induced AF [113, 120]. PKA-dependent hyper-phosphorylation of RyR2 has also been documented in dogs with atrial tachypacing and patients with chronic AF, causing dissociation of the RyR2 stabilizing

protein FKBP12.6 [121]. The role of RyR2 Ca^{2+} release in AF is described in more detail in the introduction to Chapter 6.

1.1.4 Oxidative Stress and Atrial Fibrillation

Reactive oxygen species (ROS) are highly reactive metabolites of oxygen with unpaired electrons [122]. Biologically relevant forms of ROS include the superoxide radical anion ($O_2{\cdot}^-$), hydrogen peroxide (H_2O_2), and the hydroxyl radical (OH^-). In myocardial tissues, these molecules are predominantly derived from the mitochondria, xanthine oxidoreductase (XOR), uncoupled nitric oxide (NO) synthase (NOS), and nicotinamide adenine dinucleotide/phosphate (NADPH) oxidases (Figure 1.1), which confine ROS production and ROS-mediated signalling to specific subcellular compartments [5, 122].

In the mitochondria, $O_2{\cdot}^-$ is produced as a normal by-product of oxidative phosphorylation and occurs mainly at Complex I and III due to electron leak during aerobic respiration [123, 124]. $O_2{\cdot}^-$ production also occurs at the SR and sarcolemmal membranes via XOR and NADPH oxidases, respectively [5]. XOR exists in two interconvertible forms, xanthine dehydrogenase and xanthine oxidase [125], the latter of which produces two molecules of H_2O_2 and two molecules of $O_2{\cdot}^-$ as by-products during the conversion of hypoxanthine to xanthine and xanthine to uric acid in the purine degradation pathway [126, 127], while NADPH oxidases (with NADPH oxidase 2 (NOX2) as the primary source of ROS in atrial myocytes [128]) produce $O_2{\cdot}^-$ through electron transfer from NADPH to molecular oxygen (details regarding the structure and function of NADPH oxidases are covered later in this chapter) [129]. Additionally, a neuronal NOS (nNOS or NOS1) is localized to both the sarcolemmal and SR membranes where it normally produces NO [130]; however, under certain conditions, it may become 'uncoupled' and produce $O_2{\cdot}^-$ [131].

ROS levels are also regulated by ROS-scavenging antioxidant systems (both enzymatic and non-enzymatic). Antioxidant enzymes include superoxide dismutase (SOD, with Cu/ZnSOD in the cytosol and MnSOD in the mitochondria [132]) which catalyzes the reduction of $O_2{\cdot}^-$ to H_2O_2 and water [133], and catalase or glutathione peroxidase which further reduce H_2O_2 to water and

oxygen [122]. ROS can also be neutralized by endogenous redox buffers including peroxiredoxins and glutathione (with GSH and GSSG as the reduced and oxidized forms, respectively), as well as nitric oxide (NO), which reacts with $O_2^{\cdot -}$ to form the less reactive peroxynitrite ($ONOO^-$) [5].

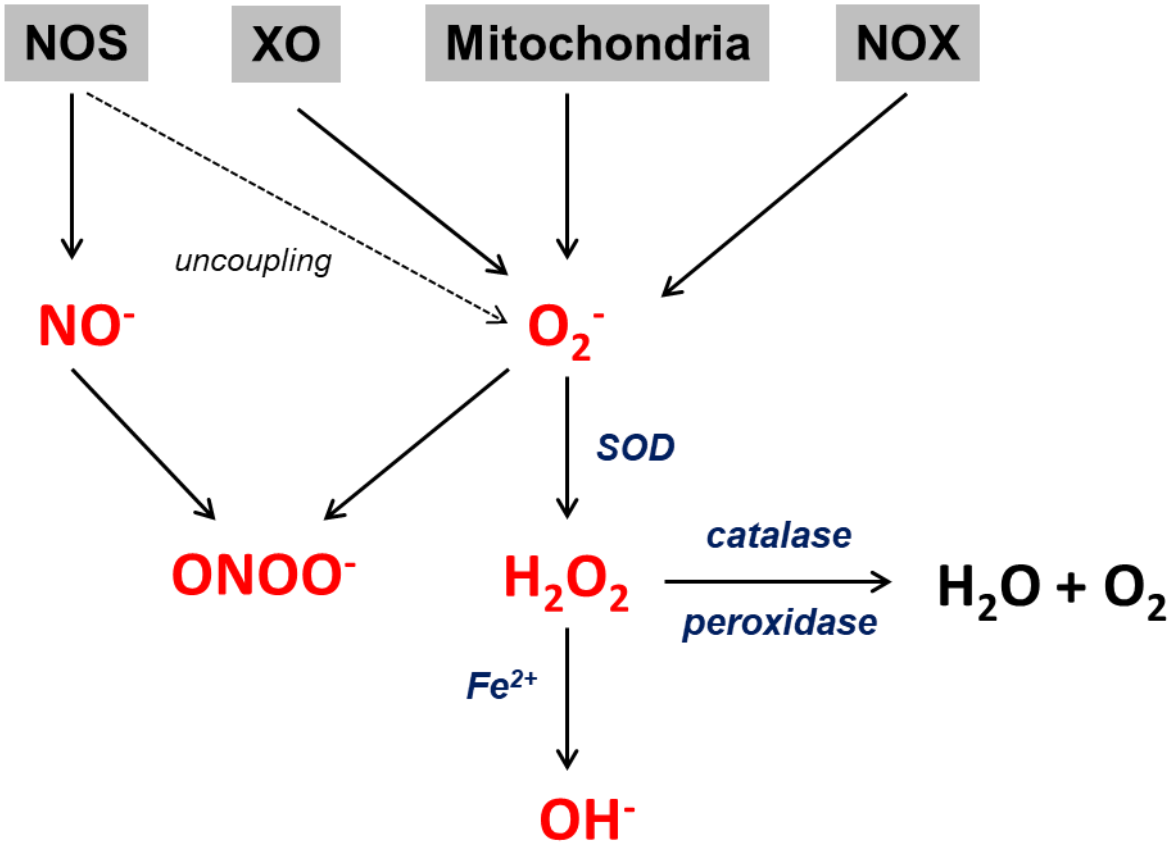

Figure 1.1: Main ROS sources in cardiac myocytes. ROS in cardiomyocytes are generated predominantly by the mitochondria, NADPH oxidases, xanthine oxidase, and uncoupled NOS. Both one electron oxidants (*e.g.*, $O_2^{\cdot -}$ and NO) and two-electron oxidants (*e.g.*, H_2O_2 and $ONOO^-$) are generated. $O_2^{\cdot -}$ is rapidly dismutated by SOD to form the non-radical H_2O_2, which can be converted by catalase or glutathione peroxidase to form water. It can also be converted to the highly reactive OH^- radical by transfer of a third electron from Fe^{2+} through the Fenton reaction [132]. NOS primarily produces NO; however, under certain conditions (*e.g.*, insufficient availability of the substrate L-arginine or the essential cofactor tetrahydrobiopterin) it may become uncoupled and produce $O_2^{\cdot -}$. Refer to text for abbreviations. Figure modified from [134].

The concept that *oxidative stress*, an imbalance in the reduction-oxidation (redox) state of the cell that occurs when the production of ROS exceeds antioxidant defense mechanisms [134, 135], may be a driver of AF progression has been suggested by a number of studies. Mihm *et al.* [136] were the first to report extensive protein oxidation in the atrial myocardium of patients with permanent AF. Later it was shown that the levels of ROS, including $O_2^{\cdot -}$ and H_2O_2, are augmented in experimental animal models as well as in patients with AF (at various stages of disease progression), along with decreases in NO bioavailability, due to an increase in the activity of several myocardial oxidase systems (summarized in Table 1.1). In AF, NADPH oxidase activity and expression of isoforms NOX2 and NOX4 are increased [137-139], XOR oxidase activity is enhanced [137, 140], and production of $O_2^{\cdot -}$ from the mitochondria rises [138] along with increased expression of Complex I and III [141].

Interestingly, some studies have demonstrated that the sources of ROS vary with both the duration and substrate of AF, with NADPH oxidases likely accounting for the increase in ROS production in the early stages of AF development, while the mitochondria/uncoupled NOS have been proposed as the major sources of ROS in persistent AF [138]. This hypothesis was first suggested by Reilly *et al.* [138] who showed that rapid atrial pacing in a goat model led to an increase in the production of $O_2^{\cdot -}$ by NADPH oxidase after two weeks of AF, but returned to baseline 6 months later. At the 6 month time-point, elevations in $O_2^{\cdot -}$ were predominantly from the mitochondria (Complex I) and uncoupled NOS [138]. Similar observations were made in patients with AF where NADPH oxidase-mediated $O_2^{\cdot -}$ production was shown to be predictive of AF development in the post-operative period [142, 143], while elevations in $O_2^{\cdot -}$ from the mitochondria and uncoupled NOS were observed in right atrial tissues from permanent AF patients [138].

Table 1.1: Summary of studies implicating oxidative stress in AF

Year	Species	Tissue	Experimental Model	Findings	Refs.
2002	Pig	LA	Atrial tachypacing (1 week)	Decreased bioavailability of NO and eNOS expression	[144]
2005	Pig	LA	Atrial tachypacing (1 week)	Increased XOR- and NADPH oxidase-mediated $O_2\cdot^-$ and Rac1 expression	[137]
2005	Human	RAA	Permanent AF (n = 6), permanent AF from paroxysmal (n = 4), paroxysmal AF (n = 5)	Increased NADPH-stimulated/apocynin-inhibitable $O_2\cdot^-$	[128]
2007	Mouse	LA	Cardiac Rac1-GTPase overexpression	Increased NADPH-stimulated $O_2\cdot^-$; spontaneous AF episodes	[145]
2007	Human	LAA	Mitral valve surgery patients (permanent AF, n = 8; sinus, n = 7)	Increased PMA-stimulated $O_2\cdot^-$ and Rac1 expression/membrane translocation	[145]
2008	Human	RAA	Post-operative AF patients (sinus rhythm, n = 99; AF, n = 71)	Increased NADPH-stimulated/apocynin-inhibitable $O_2\cdot^-$	[143]
2008	Human	RAA	Persistent AF (n = 8)	Decreased peroxiredoxin; increased NADH dehydrogenase flavoprotein and ubiquinol cytochrome C reductase core protein 1 (by mass-spectrometry/microarray)	[141]
2008	Human	RA	Persistent AF (n = 15)	Increased NOX, iNOS, eNOS expression;	[146]
2011	Human	RAA	Mitral valve regurgitation (persistent AF, n = 8; sinus rhythm, n = 8)	Increased NOX2-dependent $O_2\cdot^-$ and NOX2 expression in persistent AF patients	[147]
2011	Human	RAA	Persistent AF (n = 26)	Increased rotenone and L-NAME-inhibitable $O_2\cdot^-$	[138]
2011	Human	RAA	Post-operative AF (n = 32)	Increased NADPH-stimulated and apocynin-inhibitable $O_2\cdot^-$, $p22^{phox}$ and NOX2 protein	[138]
2011	Goat	LA/RA	Atrial tachypacing (2 weeks and 6 months)	Increased NADPH-stimulated and apocynin-inhibitable $O_2\cdot^-$, Rac1 expression at 2 weeks; Increased mitochondrial/uncoupled eNOS-derived $O_2\cdot^-$ at 6 months	[138]
2012	Human	LAA	AF patients (n = 18); sinus rhythm (n = 17)	Increased NOX4-dependent H_2O_2	[139]

A summary of studies investigating the sources of ROS in AF patients and animal models. Table modified/adapted from ref. [148]. RAA – right atrial appendage; RA – right atria; LAA – left atrial appendage; LA – left atria.

Further support for a role of oxidative stress in AF comes from clinical trials evaluating the efficacy of antioxidants in post-operative AF (commonly associated with increased ROS production [142, 143]). For instance, Carnes *et al.* [149] reported a significant (~50%) reduction in the incidence of post-operative AF in patients receiving ascorbic acid (vitamin C) before (and continued to 5 days after) cardiac surgery, compared with control patients. Similar findings were obtained by treatment with a combinatorial antioxidant regimen (ascorbic acid, α-tocopherol, and polyunsaturated fatty acids), which reduced the incidence of post-operative AF in the supplemented group [10 cases of AF (9.7%)] when compared with patients receiving placebo [32 AF cases (32%)] [150]. In this study, the activity of catalase, SOD, and glutathione peroxidase were increased in right atrial tissues of patients receiving the treatment regimen in association with decreased levels of malondialdehyde (a product of lipid peroxidation and a marker of oxidative stress).

Despite these accounts, very few studies have demonstrated a clear link between increased ROS and the development of an AF substrate and/or arrhythmogenic triggers. As mentioned previously, down-regulation I_{CaL} and APD shortening are key features of electrical remodelling in AF. Importantly, the L-type Ca^{2+} channel is subject to redox-mediated post-translational modifications, which may contribute to the observed reduction in I_{CaL} and associated APD shortening in AF. For instance, Carnes *et al.* [84] demonstrated that the α1c subunit of the L-type Ca^{2+} channel is S-nitrosylated in the left atrial appendage of patients with persistent AF, an effect which decreases I_{CaL} in these patients [151]. RyR2 is also redox-sensitive [152, 153] and RyR2 oxidation may promote the formation of arrhythmogenic triggers [154-156]. Xie *et al.* [155] recently reported that RyR2 channels are oxidized in the right atria of patients with AF, an effect which increases RyR2 open probability. Oxidative stress may also increase RyR2 activity indirectly via phosphorylation by the redox-sensitive kinase CaMKII. Indeed, CaMKII oxidation is increased in AF patients [156], and in mice, Ang-II-induced oxidation of CaMKII was shown to increase RyR2 phosphorylation, spontaneous Ca^{2+} release, and susceptibility to AF by rapid atrial pacing [156].

1.2 NADPH Oxidases

Among the different sources of ROS in the atrial myocardium, NADPH oxidases comprise an enzymatic family of seven isoforms that produce $O_2\cdot^-$, not as a by-product, but as their primary function during the catalytic metabolism of oxygen. The earliest description of the NADPH oxidase system came from studies on the metabolic activity of leukocytes. In 1964, Rossi and Zatti [157] correctly identified NADPH oxidase as the enzyme responsible for the burst of oxygen consumption displayed by leukocytes in response to invading pathogens, an effect which was subsequently demonstrated to result in the generation of $O_2\cdot^-$ and its downstream metabolite H_2O_2 [158]. Since its initial discovery, the NADPH oxidase system was shown to be widely expressed *in vivo*, to have diverse physiological functions, and to contribute to various pathological states.

1.2.1 General Biochemistry of NADPH Oxidases

The NADPH oxidase complex is composed of two basic features: a membrane-bound catalytic core that catalyzes the one-electron reduction of oxygen, and cytosolic regulatory subunits (including $p47^{phox}$, $p67^{phox}$, $p40^{phox}$, and a small guanine nucleotide-binding protein) that affect enzyme activity by translocating to and binding the catalytic core [159]. To date, seven distinct NADPH oxidase complexes have been identified in the mammalian genome and are collectively referred to as the NOX family; this nomenclature refers to the identity of the large subunit within the catalytic core, of which there are seven isoforms termed NOX1, NOX2 ($gp91^{phox}$), NOX3, NOX4, NOX5, DUOX1, and DUOX2 [159].

Superoxide production takes place at the large transmembrane NOX protein according to the following reaction: $NADPH + 2O_2 \rightarrow NADP^- + H^+ + 2\ O_2\cdot^-$ [129]. Consistent with their conserved function, NOX isoforms share a core structure that includes the flavin adenine dinucleotide (FAD) and NADPH-binding domains at the hydrophilic C-terminal which are required for catalytic activity and six conserved membrane-spanning α-helices at the N-terminal [160]. The third and fifth transmembrane domains each contain two conserved heme-binding

histidine residues that are predicted to position the two heme groups perpendicular to the plane of the membrane where they facilitate electron transport (reviewed in ref. [160]). Electrons are first transferred from NADPH to FAD (located on the cytosolic side) and sequentially to each heme group which reduces O_2 to $O_2^{\cdot -}$ [160]. Despite sharing a common function of $O_2^{\cdot -}$ production (the exception being NOX4 and the DUOX proteins which instead directly produce H_2O_2 [161-163]), NADPH oxidases differ in their interaction with cytosolic subunits and therefore activation of electron transport. A complete coverage of the biochemistry and physiology of all isoforms is beyond the scope of this work (see ref. [159] for a comprehensive review); instead, specific emphasis will be placed on NOX2. Figure 1.2 illustrates the structure and molecular organization of NOX2-containing NADPH oxidase.

1.2.2 Molecular Components of NADPH Oxidases

Most of what is known about the biochemistry of NADPH oxidases comes from studies on NOX2, the prototypic NADPH oxidase responsible for the phagocytic respiratory burst that confers host defense [157, 158]. The membrane-spanning catalytic component is a heterodimer of the large glycosylated NOX2 subunit (originally named $gp91^{phox}$) and the smaller non-glycosylated $p22^{phox}$ subunit that assemble in a 1:1 ratio and together are known as flavocytochrome b_{558} (or cytochrome b_{558}) [164-166]. In humans, the NOX2 gene (*CYBB*) is located on the X chromosome and produces a 65 kDa precursor protein which is then glycosylated to generate an N-linked glycoprotein with an apparent molecular weight of 91 kDa [159, 167].

The *CYBA* gene located on chromosome 16 produces $p22^{phox}$, a 194 amino acid (~22 kDa) protein that serves to stabilize the NOX2 subunit at the membrane and is essential for the functional assembly of the oxidase [159, 168]; using reconstituted cell systems, it has been shown that co-expression of both $p22^{phox}$ and NOX2, but not $p22^{phox}$ or NOX2 alone, recapitulates the functional properties of the flavocytochrome [169]. Additionally, phagocytes of patients with a naturally occurring mutation in the *CYBA* gene show no detectable levels of $p22^{phox}$ and NOX2

protein, suggesting that stable expression of either subunit is mutually dependent on the other [170]. $p22^{phox}$ also provides a scaffold for the recruitment of the cytosolic regulatory subunits; the C-terminal contains proline-rich regions that are capable of interacting with the SRC Homology 3 (SH3) domains of both $p47^{phox}$ and $p67^{phox}$ [169].

The regulatory subunits exist in the cytosol as a dormant complex with $p67^{phox}$ acting as a bridge between $p47^{phox}$ and $p40^{phox}$ [171, 172]. Activation of the enzymatic complex occurs through a series of protein-protein interactions that begins with the phosphorylation of $p47^{phox}$ at its auto-inhibitory region [173]. Consequently, a conformational change in its SH3 domain enables $p47^{phox}$ to translocate to the membrane and bind to the proline-rich region of $p22^{phox}$ [174]. This translocation of $p47^{phox}$ to the membrane is crucial for the recruitment of the entire cytosolic complex to the catalytic core. Evidence for this is found in $p47^{phox}$-deficient patients, where $p67^{phox}$, $p40^{phox}$, and Rac1-GTPase fail to translocate to the membrane of neutrophils upon stimulation [175, 176]. $p47^{phox}$ also appears to play a modulatory role; for instance, in the absence of $p47^{phox}$ much greater concentrations of $p67^{phox}$ are required to induce $O_2{\cdot}^-$ production (*e.g.*, micromolar rather than nanomolar concentrations) [177].

At the membrane, $p67^{phox}$ directly binds flavocytochrome b_{558} and regulates electron transfer from NADPH to FAD [177, 178]. Also crucial are the Rac GTPases which translocate to the membrane independently of the cytosolic subunits upon binding of guanosine triphosphate (GTP). Rac proteins interact with both flavocytochrome b558 (at the dehydrogenase domain of NOX2) and $p67^{phox}$ (at the N-terminal tetratricopeptide repeats of $p67^{phox}$) to promote the transfer of electrons from FAD to the heme groups and molecular oxygen [177, 179, 180].

The role of $p40^{phox}$ is less clear. It becomes phosphorylated and translocates to the membrane in a similar manner to $p47^{phox}$ but it does not appear to interact directly with flavocytochrome b_{558}, nor is it required for oxidase activity. Instead, $p40^{phox}$ has been suggested to increase the affinity of $p47^{phox}$, $p67^{phox}$, and/or Rac for flavocytochrome b_{558}. This is supported by the observation that $p40^{phox}$ significantly reduces the concentration of $p47^{phox}$ required to produce half-maximal NADPH oxidase activity [181]. Furthermore, in the same cell-free systems, $p40^{phox}$ could elicit a low rate of $O_2{\cdot}^-$ production even in the absence of $p47^{phox}$ [181].

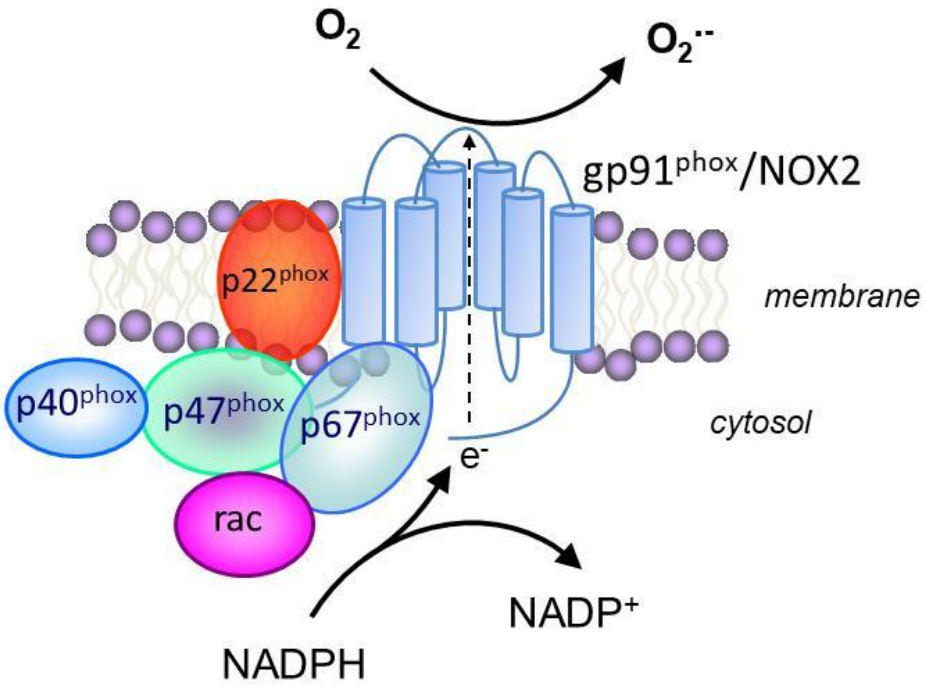

Figure 1.2: Schematic illustrating the structure and molecular organization of the gp91^{phox}-containing NADPH oxidase. The NADPH oxidase complex is composed of two basic features: a membrane-bound catalytic core and cytosolic regulatory subunits. The membrane-spanning catalytic component of NOX2 is a heterodimer of the large gp91^{phox} and the smaller p22^{phox} subunit. Activation of NOX2 requires the phosphorylation and membrane translocation of p47^{phox} which brings the other cytosolic components, p40^{phox}, p67^{phox}, and the small GTPase Rac to the NOX2/p22^{phox} complex to initiate the one-electron reduction of oxygen.

As in the case of NOX2, NOX1 requires p22^{phox}, cytosolic subunits, and Rac proteins for activation. In pull-down assays, NOX1 was shown to immunoprecipitate with p22^{phox} [182], while functional studies in co-transfected cells demonstrated a reduction in NOX1-mediated $O_2\cdot^-$ production with p22^{phox}-suppressing silencing RNAs [169]. The regulatory subunits that interact with NOX1 are p47^{phox} and p67^{phox}, as well as their homologues, NOXO1 (NOX-organizer 1) and NOXA1 (NOX-activator 1), respectively [183, 184]. NOXO1 and p47^{phox} share ~25% homology and have similar functional domains [184]; for instance, both have the phox homology domain that interacts with membrane phospholipids and two SH3 domains that facilitate interaction with p22^{phox}. A notable difference is that NOXO1 lacks the auto-inhibitory region that is present in p47^{phox} and prevents binding to p22^{phox} in its de-phosphorylated state [185]. Consequently, NOX1

displays both stimulus-dependent and stimulus-independent activation [183]. In HEK293 cells co-transfected with NOX1 and either NOXO1 and NOXA1, $p47^{phox}$ and $p67^{phox}$, $p47^{phox}$ and NOXA1, or NOXO1 and $p67^{phox}$, constitutive activity was observed exclusively for NOXO1 and NOXA1, suggesting that these proteins must interact with each other to produce stimulus-independent activation of NOX1 [185].

The overall structure and protein-protein interactions of NOXA1 and $p67^{phox}$ are similar; both contain N-terminal tetratricopeptide repeats which interact with Rac proteins, a highly conserved activation domain that facilitates interaction with NOX proteins, and a C-terminal SH3 domains that interact with NOXO1 and $p47^{phox}$ [159]. However, differences do exist; for instance, NOXA1 only has one SH3 domain at the C-terminal (as opposed to $p67^{phox}$ which has two) and does not interact with $p40^{phox}$ [159, 184]. There is also evidence for the involvement of Rac proteins in the regulation of NOX1. In transfected cells, NOX1-mediated $O_2\cdot^-$ production is reduced upon depletion of Rac1 [186], while mutations in either Rac1 or NOXA1 that disrupt Rac1 binding to the tetratricopeptide repeats of NOX1 have also been demonstrated to inhibit oxidase activity [187].

NOX3 shares ~56% amino acid sequence identity with NOX2 and its overall structure is predicted to be very similar to both NOX1 and NOX2 [159, 188]. NOX3 functionally interacts with $p22^{phox}$. This is supported by the observation that $p22^{phox}$ mutants lacking the proline rich region at the C terminal inhibit ROS production by NOX3 [169]. In heterologous expression studies, NOX3 displays high basal activity even in the absence of regulatory subunits, but can be augmented by both NOXO1 and $p47^{phox}$ [189]. Furthermore, both $p67^{phox}$ and NOXA1 have been shown to enhance the $p47^{phox}$-mediated increase in NOX3 activity, while blunting the NOXO1-mediated response [189]. The most physiologically relevant regulator of NOX3 is as yet unclear but *in vivo* data suggests a requirement for NOXO1. This is based on data showing that NOXO1-deficiency mimics the phenotype observed with mutations in the genes for both $p22^{phox}$ [190] and NOX3 [191, 192].

Similar to NOX1 and NOX2, NOX4 also requires $p22^{phox}$ for full activity. NOX4 directly associates with $p22^{phox}$ in heterologous systems [161, 182] and a functional NOX4/$p22^{phox}$ complex

is found endogenously in focal adhesions at the plasma membrane of vascular smooth muscle cells [193]. Unlike NOX1-3, this interaction does not occur at the C-terminal proline rich region of $p22^{phox}$ as point mutations in $p22^{phox}$ that produce a truncated C-terminal do not affect ROS production from NOX4 [169]. Instead, NOX4 appears to bind a dual tryptophan motif at the N-terminal [194].

There is also evidence that NOX4 is constitutively active as NOX4-dependent ROS production is not enhanced by co-expression of any of the known regulatory subunits, including $p47^{phox}$, $p67^{phox}$, NOXO1, NOXA1, or Rac proteins [161, 195, 196]. Mechanisms of subunit-independent NOX4 activation might include modulation of transcriptional activity. Using a tetracycline-inducible NOX4-expressing cell line, Serrander *et al.* [162] observed a rapid increase in NOX4 mRNA content upon tetracycline stimulation that was closely followed by an increase in ROS production. However, in certain cell types that endogenously express NOX4, a Rac1-dependent activation of NOX4 was also documented [197, 198]. NOX4 has also been suggested to produce predominantly H_2O_2 [161, 162], although some studies have reported $O_2{\cdot}^-$ generation [199].

NOX5 distinguishes itself considerably from the other isoforms as it does not require $p22^{phox}$ or cytosolic subunits for its activity but is instead activated directly by Ca^{2+} [159, 200]. This unique feature is mediated by the presence of four Ca^{2+}-binding EF hands at the intracellular NH_2 terminus of the enzyme; upon Ca^{2+} binding, the EF hands undergo a conformational change that brings them into contact with the catalytic C-terminal of the NOX5 subunit, which in turn initiate the electron transfer reaction [201].

1.2.3 NOX2-generated $O_2{\cdot}^-$ in myocardial physiology

Perhaps the best characterized physiological function of NOX2 in cardiomyocytes is that of mechanochemotransduction. In a process termed '*X-ROS'* (NOX2-dependant ROS) signalling, microtubule-mediated activation of NOX2 produces a local increase in ROS production that

increases RyR2 Ca^{2+} sensitivity and successfully triggers excitation-contraction dynamics in ventricular cardiomyocytes. In their study, Prosser *et al.* [202] applied a moderate level of stretch (~8% of cell length) to individual myocytes and observed a burst of localized Ca^{2+} sparks that was rapid in onset and occurred almost simultaneously with an increase in the fluorescence signal of the ROS sensor 2',7'-dichlorofluorescein (DCF). Upon normalization of cell length, both $[Ca^{2+}]_i$ and superoxide levels returned to baseline with similar kinetics.

Importantly, the stretch-dependent production of ROS and burst of $[Ca^{2+}]_i$ could be inhibited by diphenyleneiodonium (DPI), an inhibitor of flavin-containing oxidases, or gp91ds-tat, a peptide inhibitor that blocks the interaction of $gp91^{phox}$ with $p47^{phox}$, thus implicating NOX2 in this process. Myocytes lacking NOX2 expression also failed to show a stretch-dependent production of ROS. The stretch-induced production of ROS and $[Ca^{2+}]_i$ also requires an intact microtubule network and may involve Rac-dependent activation of NOX2 [203]. For instance, treatment of cells with colchicine to disrupt the assembly of microtubules, or inhibition of Rac1 (which binds NOX2 and microtubules [204]) abolished the stretch-dependent production of ROS production and related Ca^{2+} burst.

The rapid enhancement of SR Ca^{2+} release in response to NOX2-derived $O_2{\cdot}^-$ was attributed to an increase in the Ca^{2+}-sensitivity of RyR2. This is supported by data showing co-localisation of NOX2 with t-tubule structures at the Z-line, in close proximity (~15 nm) to junctional RyR2 channels, as well as an increase in the percentage of active RyR2 clusters in response to stretch in mouse ventricular myocytes, an effect which was abolished by gp91ds-tat [202]. In SR vesicles isolated from rat ventricles, stimulation of NOX2 activity was also demonstrated to increase RyR2 channel sensitivity to activation by cytoplasmic Ca^{2+} and therefore the rate of SR Ca^{2+} release [205]. However, whether this effect is a direct consequence of channel oxidation is unclear.

In a follow-up study, the authors used a cyclic stretch protocol to better mimic physiologic cardiomyocyte behaviour, *e.g.*, cyclic contraction and relaxation, and further demonstrated that NOX2-dependent ROS dynamically couples cell shortening to $[Ca^{2+}]_i$ dynamics in ventricular myocytes [206]. Cyclic stretch (~8% of cell length) caused an initial similar increase in ROS

production and Ca^{2+} spark rate as observed with static stretch [202]; however, upon sustained cyclic stretch (up to 3 minutes), the increase in ROS production and related Ca^{2+} spark rate remained elevated for the duration of the protocol. Importantly, these effects were abolished by inhibition of NOX2 activity with either DPI or gp91ds-tat. Furthermore, varying both the frequency (to mimic changes in heart rate) and the amplitude (to mimic changes in diastolic length or pre-load) of cyclic stretch produced a graded increase in NOX2-dependent ROS production. The authors suggest that a basal amount of ROS is produced by NOX2 during cell shortening and relaxation alone which can be further modulated by changes in heart rate or pre-load to maintain cardiac function during acute physiological stress.

A recent study implicated NOX2-derived ROS in mediating the positive inotropic effects of angiotensin II (Ang-II) [207]. Using mice with cardiomyocyte-specific overexpression of NOX2 (NOX2-Tg), Zhang *et al.* [207] observed an increase in left ventricular dP/dt_{max} (index of contractility) in NOX2-Tg mice upon acute Ang-II stimulation which was without effect in wild-type littermate controls. Both the speed of relaxation and the rate of decay of the $[Ca^{2+}]_i$ transient were faster in Ang-II myocytes from NOX2-Tg mice. These findings were associated with an increase in the Serine-16 phosphorylated fraction of PLN and in SERCA activity which produces an increase in the SR Ca^{2+} content. The increase in SR Ca^{2+} content augments the magnitude of Ca^{2+} release resulting in an increased amplitude of the $[Ca^{2+}]_i$ transient and thus myocyte shortening. In agreement with this, $[Ca^{2+}]_i$ transient amplitude and the speed of contraction and relaxation were increased in NOX2-Tg myocytes in response to AngII. Likewise, Ca^{2+} influx through L-type Ca^{2+} channels is also increased by Ang-II in a NOX2-dependent manner [208] and may therefore contribute to the modulation of myocardial contractility observed in NOX2-Tg mice.

1.2.4 NOX2-generated $O_2^{\cdot -}$ in myocardial disease

Whereas NOX2-dependent ROS production preserves contractile function by fine-tuning Ca^{2+} signalling in excitation-contraction coupling, chronically elevated NOX2 signalling may be

detrimental. The fact that NOX2-derived $O_2^{\cdot -}$ regulates RyR2 channels is especially pertinent to cardiac arrhythmogenesis, as spontaneous RyR2 Ca^{2+} release provides an arrhythmogenic trigger due to delayed afterdepolarizations. Indeed, Wagner *et al.* [208] previously demonstrated that increased NOX2-dependent ROS production downstream of Ang-II causes afterdepolarizations by differentially activating CaMKII and PKA. By using $gp91^{phox}$-deficient and CaMKII-deficient mice, as well as pharmacological inhibition of PKA, the authors demonstrated that Ang-II enhances peak I_{CaL} and I_{Na} via NOX2 and PKA, while a NOX2/CaMKII pathway was shown to promote diastolic SR Ca^{2+} leak (*e.g.*, via increased Ca^{2+} sparks), ultimately leading to an increase in the frequency of both early and delayed afterdepolarizations in isolated murine ventricular cardiomyocytes [208].

Augmented NOX2-derived ROS signalling may also underlie ventricular arrhythmogenesis in the *mdx* mouse model of Duchenne muscular dystrophy [202, 209]. Ventricular myocytes from *mdx* mice display greater expression of the NOX2 subunits, $p47^{phox}$ and $gp91^{phox}$, along with higher levels of cellular ROS production compared to wild-type controls [210]. Importantly, moderately stretching *mdx* myocytes was shown to enhance NOX2-derived $O_2^{\cdot -}$ production (*e.g.*, increased X-ROS signalling) and promote arrhythmogenic Ca^{2+} waves instead of the Ca^{2+} sparks that are observed in healthy cardiomyocytes in response to physiological stretch [202].

Of particular relevance to the work being undertaken in this thesis, NOX2 has also been implicated in AF. This is described in more detail in the introduction to Chapter 3, but a NOX2-mediated increase in atrial $O_2^{\cdot -}$ is observed in right atrial tissues of patients with paroxysmal [128] and post-operative AF [138], and is predictive of AF development in the post-operative period [142, 143]. Likewise, in a goat model of pacing-induced AF, NOX2-derived $O_2^{\cdot -}$ production was shown to be increased in the left atrium after 2 weeks of AF, along with increased expression of both NOX2 and $p22^{phox}$ [138]. However, the mechanisms linking increased NOX2 activity to AF are unclear. We know that NOX2-derived $O_2^{\cdot -}$ promotes RyR2 Ca^{2+} release in ventricular myocytes [202, 208], but whether this occurs in the atria is yet to be established. A previous article by Purohit *et al.* [156] showed that 3 weeks of Ang-II infusion increased atrial ROS production,

oxidation (and thus activation) of CaMKII, SR Ca^{2+} leak, and AF susceptibility in wild-type but not $p47^{phox}$-knockout mice, suggesting a link between NOX2 and spontaneous RyR2 Ca^{2+} release in AF.

NOX2-derived $O_2\cdot^-$ is also implicated in atrial structural and electrical remodelling, both of which increase susceptibility to AF. For instance, mice with cardiac-specific overexpression of constitutively active Rac1, a necessary activator of NOX2, exhibit increased NADPH-stimulated ROS production and collagen content (marker of fibrosis) in the atria, and develop spontaneous episodes of AF [145], while short-term administration of statins, which are known to inhibit atrial NOX2 activity, was reported to attenuate the AF-related shortening of the atrial effective refractory period in a canine model of tachypacing-induced AF [211]. Beyond this, very little is known regarding the role of NOX2-derived $O_2\cdot^-$ production in AF. Therefore, the focus of the current investigation is to determine whether NOX2-derived $O_2\cdot^-$ production promotes the development of AF and to dissect the underlying molecular mechanisms.

1.3 Hypothesis and Objectives

Taking together the background literature in this chapter, this thesis aims to investigate the role of NOX2-derived $O_2^{\cdot -}$ in AF. It is predicted that altered NOX2 activity in the atrial myocardium contributes to the development of AF owing to distinct changes in the electrophysiological properties and Ca^{2+} dynamics of atrial cells. More specifically, this thesis aims to investigate the following questions:

1. **Does myocardial-specific overexpression of NOX2 promote the development of AF *in vivo*?** An increase in atrial NOX2 activity accompanies AF induction and electrical remodelling in large animal models and predicts incident AF in humans; however, whether it is directly involved in the development of AF remains to be demonstrated. In **Chapter 3**, I characterize the AF phenotype of a transgenic mouse with myocardium-targeted overexpression of NOX2 using transesophageal burst pacing.

2. **Is pharmacological inhibition of NOX2 activity sufficient to prevent AF?** Statins are known to exhibit a wide range of pleiotropic effects among which is the reduction of NOX2 activity and related $O_2^{\cdot -}$ production in the atrial myocardium. **Chapter 4** investigates whether dietary supplementation with atorvastatin is protective against the development of pacing-induced AF.

3. **Does NOX2-derived $O_2^{\cdot -}$ promote electrical and/or structural remodelling of the atria?** Electrical and structural remodelling of the atria, consistent with APD shortening and impaired conduction, has been demonstrated to support sustained episodes of AF. **Chapter 5** describes the development and application of an optical imaging system to record depolarization/ repolarization kinetics and electrical impulse conduction in isolated intact atrial preparations with high spatiotemporal resolution. This approach was then used to measure APD and conduction velocity in the left and right atria from wild-type and NOX2 transgenic mice.

4. **Does NOX2-derived $O_2\cdot^-$ modulate the diastolic Ca^{2+} leak from RyR2?** RyR2 channel function has been shown to be modulated by NOX2-derived $O_2\cdot^-$ and channel hyperactivity has been implicated in the initiation of AF in animal models and humans. In **Chapter 6**, I measure the diastolic leak of Ca^{2+} through RyR2 channels in atrial cardiomyocytes isolated from wild-type and NOX2 transgenic mice. Post-translational modifications of RyR2, which are known to modulate RyR2 leak, are also investigated.

2 Methods

2.1 Animal Model

Transgenic mice with cardiomyocyte-targeted expression of NOX2 (NOX2-Tg) were generously provided by the group of Professor Ajay Shah at King's College London (London, UK) and housed in a Specific Pathogen Free environment in the Functional Genetics Facility at the Wellcome Trust Centre for Human Genetics (Oxford, UK). The transgenic mouse model was developed by Zhang *et al.* [207] by cloning a 1.8 kb fragment of the human *NOX2* gene downstream of the murine ventricular myosin light chain-2 (MLC-2v) promoter. The mini-transgene (~8.6 kb) was excised by *NotI* digestion and used for microinjection into fertilized 1-cell CBA/C57Bl/6 F1 oocytes. The offspring were screened with polymerase chain reaction (PCR) to confirm successful transgene integration and backcrossed for 10 generations onto a C57/Bl/6 background. All experiments were performed on male and female adult heterozygous NOX2-Tg mice and their wild-type (WT) littermate controls aged 16 to 20 weeks unless otherwise specified. All animal studies were conducted in accordance with the Home Office Guidance on the Operation of Animals (Scientific Procedures) Act 1986 (HMSO, UK) under Project Licences 30/2804 and 30-3374.

2.1.1 Genotyping

Ear notch biopsies were used to obtain samples of genomic DNA for genotyping. Tissue was digested in 75 µL of DNA lysis buffer (25 mmol/L NaOH, 0.2 mmol/L EDTA, pH 12) for 30 minutes at 95 °C, after which an equal volume of neutralization buffer (40 mmol/L Tris-HCl, pH 5) was added. Samples were vortexed and centrifuged at 13 000 rpm for 5 minutes at room temperature and supernatants were transferred into a new tube. DNA samples were stored at -20 °C until PCR reactions were performed. To perform the PCR reaction, DNA samples were added to individual PCR tubes along with primer sets (Table 2.1), water, dNTPs, $MgCl_2$, and Taq

polymerase in the following quantities: 5 µL DNA, 5 µL DNase-free, RNase-free water, 0.5 µL $MgCl_2$, 0.5 µL NOX2 primers (20 µmol/L), 0.5 µL GAPDH primers (10 µmol/L), 12.5 µL Taq polymerase-dNTP mixture.

Table 2.1: Oligonucleotide primers used in the genotyping protocol

Primer	Sequence
NOX2-F	5'- GCACCAAAGAAAGCCAAGAA-3'
NOX2-R	5'- CCAGTGCTGACCCAAGAAGT-3'
GAPDH-F	5'- CCTAGACAAAATGGTGAAGG-3'
GAPDH-R	5'- GACTCCACGACATACTCAGC-3'

PCR amplification was performed using a Bio-Rad Tetrad 2 Peltier Thermal Cycler (Bio-Rad Laboratories Ltd.) according to the programme in Table 2-2 and PCR products were resolved on a 2% agarose gel (4 g agarose in 200 mL TAE buffer containing 8 µL Gel-Red (*Biotium*) nucleic acid gel stain).

Table 2.2: Thermal cycler PCR program

Temperature	Time	PCR step
94 °C	5 minutes	*enzyme activation*
94 °C	30 seconds	*denaturation*
56 °C	30 seconds	*annealing*
72 °C	30 seconds	*extension*
72 °C	10 minutes	

Denaturation, annealing, and extension steps are set for 32 cycles.

2.2 Tissue Collection and Processing

Mice were killed by Schedule 1 cervical dislocation and the thorax was rapidly opened to expose the ventricles and surrounding tissues. For organ harvest, the descending aorta was cut and hearts were perfused through the right and left ventricles with ice-cold phosphate-buffered saline (PBS), 5 mL through each ventricle. Hearts were then excised and the right atria, left atria, and left ventricle were carefully dissected, placed into individual cryo-tubes, and frozen on dry ice. Samples were stored at -80 °C until required. Frozen tissue samples were homogenized in a set volume of the appropriate lysis buffer (see specific protocols) using pre-cooled stainless steel beads and a small bead mill (TissueLyser LT, Qiagen). Typically, one cycle of the bead mill (50 Hz for 2 minutes) was sufficient to disrupt the tissue. If multiple cycles were required for complete disruption, tissue homogenates were placed on ice for at least 1 minute between runs.

2.3 RNA Isolation and Quantitative Reverse Transcription PCR

Total RNA was isolated from frozen atrial and ventricular tissues (stored at -80 °C) using the mirVana RNA isolation kit (*ThermoFisher Scientific*). RNA concentration was determined by measuring the absorbance at 260 nm using the NanoDrop ND-1000 Spectrophotometer (*ThermoFisher Scientific*), normalised to a standard concentration (25 ng/µL) and stored at -80 °C to prevent degradation until further processing. cDNA was synthesized from 300 ng total RNA with the QuantiTect Reverse Transcription Kit (*Qiagen*), according to the manufacturer's instructions. Gene expression was measured with TaqMan gene expression assays (*ThermoFisher Scientific*). For the PCR reaction, 4.5 µL of cDNA (10 ng) was mixed with 5 µL of the TaqMan Fast Advanced Master Mix (*ThermoFisher Scientific*) and 0.5 µL of the appropriate TaqMan probe in a 96- or 384-well plate. Plates were sealed with Optical Adhesive Covers (*ThermoFisher Scientific*) and centrifuged briefly to ensure that the entire volume was at the bottom of the wells. Each sample was assayed in duplicates, including negative controls containing water instead of

cDNA. Housekeeping genes were included in each plate to control for variability between samples. All reactions were performed using the ABI Prism system (*Applied Biosystems*).

2.3.1 Quantitation of Gene Expression

Gene expression levels were measured by relative quantification using the comparative Ct method (ΔΔCt method) with reference to a housekeeping gene, as described in User Bulletin No. 2: Relative Quantitation of Gene Expression (*Applied Biosystems*). This method involves obtaining the cycle threshold (Ct) value for each sample, which corresponds to the number of cycles needed for the amplification of the PCR product to reach a fixed threshold in the exponential phase of the reaction. The Ct value is inversely proportional to the amount of target mRNA in the sample, so that a highly abundant gene will have a low Ct value and a high Ct value indicates a lower level of expression. Ct values are necessary to convert the data into relative quantities.

First, Ct values are obtained by setting the threshold to the linear phase of the PCR amplification plot. The ΔCt value is then calculated by subtracting the mean Ct for the housekeeping gene from the mean Ct of the gene of interest, according to the following equation:

$$\Delta Ct = Ct(\text{target gene}) - Ct(\text{housekeeping gene})$$

Since the Ct values are on a logarithmic scale, relative expression of the gene of interest to a housekeeping gene can be calculated by applying the negative ΔCt exponential function of 2 (*i.e.*, $2^{-\Delta Ct}$). The ΔΔCt is obtained by subtracting the mean of ΔCt WT values in each tissue type from the ΔCt of each sample. Gene expression relative to WT control samples is then determined by calculating $2^{-\Delta\Delta Ct}$. Statistical analysis was performed on ΔCt values or ΔΔCt values, as appropriate. Specific details are provided in the relevant chapters.

2.4 Western Blot Analysis

Frozen RA and LA tissue samples were homogenized in 150 µL RIPA buffer (prepared from 10X stock, *Sigma Aldrich*) containing tablet protease and phosphatase inhibitors (*ThermoFisher Scientific*). Samples were centrifuged for five minutes at maximum speed to remove any remaining tissue debris and the sample supernatant was then transferred to new tubes. Protein concentration was estimated using the BCA protein assay kit (*ThermoFisher Scientific*) with bovine serum albumin (BSA) as standard and samples were incubated with NADPH (100 µmol/L) for 15 minutes at 37 °C to enhance NOX2 activity. Samples were loaded onto NuPage 4-12% Tris-Acetate gradient gels (*ThermoFisher Scientific*) or Criterion Tris-Glycine precast gels (*Bio-Rad*) for electrophoretic separation and transferred onto nitrocellulose membranes. Antibodies used were: anti-gp91^{phox}, RyR2, and phosphorylated RyR2 (Phospho-RyR2-Ser2808, Phospho-RyR2-Ser2814), and HRP-conjugated GAPDH. The band intensities were detected and quantified using the ChemiDoc Imaging system (*Bio-Rad*). GAPDH was used as a loading control except for phosphorylated protein levels which were normalized by the respective total protein levels. Specific details are provided in the relevant chapters.

2.5 Measurement of $O_2{\cdot}^-$ Production

$O_2{\cdot}^-$ is a short-lived radical anion that can be reliably detected and quantified by way of its reaction with certain probes that produce stable compounds [212]. In cellular systems, the probe of choice is the fluorescent compound dihydroethidium (DHE). Upon oxidation, DHE produces 2-hydroxyethidium (2-OHE), known to be specific for $O_2{\cdot}^-$, and ethidium, which is thought to reflect the general redox status of the cell [213]. 2-OHE can be readily separated from its parent DHE and ethidium by high performance liquid chromatography (HPLC) and the 2-OHE peak is used as a measure of intracellular $O_2{\cdot}^-$ production. A description of the methodology is provided in refs. [212] and [214] and reviewed in ref. [213].

2.5.1 Detection of Dihydroethidium Oxidation Products by HPLC

For the detection and quantification of 2-OHE, frozen RA and LA tissue samples were homogenized in Krebs-HEPES buffer (in mmol/L: 118 NaCl, 10 HEPES, 25 $NaHCO_3$, 5.6 glucose, 4.7 KCl, 1.2 KH_2PO_4, 1.1 $MgSO_4$, 1.4 $CaCl_2$, pH 7.4) supplemented with tablet protease inhibitors (*ThermoFisher Scientific*). Homogenates were centrifuged at 13 000 rpm for 5 minutes (4°C) and the protein content in the supernatants was measured using the BCA protein assay kit (*ThermoFisher Scientific*). The samples were then diluted to obtain a final concentration of 100 µg/mL. An aliquot (100 µL) of each sample was then transferred to a separate amber tube and incubated with NAPDH (100 µmol/L) for 15 minutes at 37°C. A separate aliquot of equal volume was incubated with NADPH for 15 minutes at 37°C followed by tiron (100 mmol/L) for an additional 15 minutes at 37°C. Both aliquots were then incubated with DHE (50 µmol/l) for 15 minutes at 37°C. After incubation, samples were further processed for high-performance liquid chromatography analysis by adding methanol and HCl (0.1 mol/L).

A portion of each sample (150 µL) was then injected into an isocratic HPLC system equipped with a Jasco PU-2080 pump, Jasco X-LC 3075 UV absorbance detector and a Jasco FP-2020 Plus fluorescence detector. DHE was monitored with UV absorption at 355 nm; 2-OHE and ethidium production was monitored by the fluorescence detector with excitation at 480 nm and emission at 590/595 nm. The mobile phase was composed of 0.1% trifluoroacetic acid and an acetonitrile gradient (from 30% to 50% over 23 minutes) at a flow rate of 1.0 mL/min. Quantification of $O_2{\cdot}^-$ was done by comparing the area under the 2-OHE peak between NADPH- and tiron-treated sample and normalizing the signal to the protein content. All results are expressed as the tiron-inhibitable fraction of 2-OHE as this measurement is taken to be representative of the true level of $O_2{\cdot}^-$ production.

2.6 Cholesterol Assay

Myocardial and plasma cholesterol content was measured by isolation of the lipid fraction. Briefly, tissue and plasma samples were homogenized with a 200 mL solution of 38.5% chloroform, 60% isopropanol, and 0.55% NP-40 by volume. Samples were centrifuged for 10 minutes at 15 000 rpm and supernatants were then transferred to new tubes and dried at 50 °C to remove the chloroform. Dried pellets were placed under a vacuum for 30 minutes to remove trace organic solvents. Dissolved dried lipids were then re-suspended in 200 µL of Cholesterol Assay Buffer and cholesterol levels were measured using the Amplex Red Cholesterol Assay Kit according to manufacturer's instructions (*ThermoFisher Scientific*).

2.7 *In-Vivo* Interventions

All *in vivo* procedures were performed at the Functional Genetics Facility at the Wellcome Trust Centre for Human Genetics (Oxford, UK) in accordance with the Home Office Guidance on the Operation of Animals (Scientific Procedures) Act 1986 (HMSO, UK) under Project Licences 30/2804 and 30-3374.

2.7.1 Echocardiography

To determine whether myocardial NOX2 overexpression alters left ventricular structure and function, WT and NOX2-Tg mice underwent 2D-echocardiography. Mice were placed under general anaesthesia with a 2% isoflurane/oxygen mixture using a Benson isoflurane chamber. Suitable depth of anaesthesia was checked by reduced toe pinch reflex and reduced respiratory rate. Once suitably anesthetised, mice were placed on a heated pad which also contained built-in leads for continuous ECG acquisition which was used to monitor the heart rate throughout the imaging protocol. Liquid eye gel (Viscotears Liquid Gel, Novartis) was applied to the eyes to prevent

drying. Chest fur was then removed with an electric shaver and a layer of acoustic coupling gel was applied to the chest wall.

Echocardiography was performed using the VisualSonics Vevo 2100 system equipped with an ultra-high frequency MS400 cardiovascular transducer (18-38 MHz). LV systolic function was assessed at near-physiological heart rates (~500 bpm) using the short-axis view. LV interventricular septal thicknesses, internal diameters, and posterior wall thicknesses at diastole and systole were measured from M-mode images at the level of the papillary muscles. LV mass was calculated from the diastolic LV internal diameter (LVID) and LV wall thickness measurements. LV ejection fraction (EF) and fractional shortening (FS) were calculated according to the following equations:

$$\text{EF}\ (\%) = 100\ \text{x}\ [(\text{EDV} - \text{ESV})/\text{EDV}]$$

$$\text{FS}\ (\%) = 100\ \text{x}\ [(\text{LVIDd} - \text{LVIDs})/\text{LVIDd}]$$

Pulsed-wave tissue Doppler imaging of mitral valve flow obtained in apical 4-chamber view was used to evaluate LV diastolic function. The Doppler measurements include the ratio of peak velocity of early to late filling of mitral inflow (E/A), isovolumetric contraction time (IVCT), and isovolumetric relaxation time (IVRT). Images were acquired at low heart rates (~350 bpm) in order to observe the distinct phases of early and late LV diastolic filling.

2.7.2 Electrophysiology

To determine whether NOX2 overexpression increases AF vulnerability, WT and NOX2-Tg mice underwent *in vivo* electrocardiography and atrial pacing studies. Mice were placed in a Benson isoflurane induction chamber and anaesthetized with a 5% isoflurane/oxygen mixture. The animals were then transferred onto a regulated heating pad in the supine position and maintained under general anaesthesia with a 2% isoflurane/oxygen mixture. Sufficient anaesthesia was confirmed by reflex analysis. Surface electrocardiogram recordings and transesophageal atrial pacing were performed as described below.

2.7.2.1 Surface ECG Recordings

For the continuous recording of the surface ECG, platinum subdermal needle electrodes (F-E7, *Grass Technologies*) were attached to each limb in lead II arrangement. Electrodes were connected to an Iso-DAM8A amplifier (*World Precision Instruments*) and the CED Power 1401-3A interface (*Cambridge Electronic Design Ltd*.), and data was acquired using the Spike 2 electrophysiology software. ECG signals were sampled at 2000 Hz and displayed in real time for the duration of the protocol. Figure 2.1 illustrates the various components of the electrophysiology equipment. After placement of the needle electrodes, mice were given a minimum of 5 minutes for the heart rate to stabilize. A five minute recording was taken for offline analysis of ECG parameters, after which transesophageal atrial burst pacing was performed.

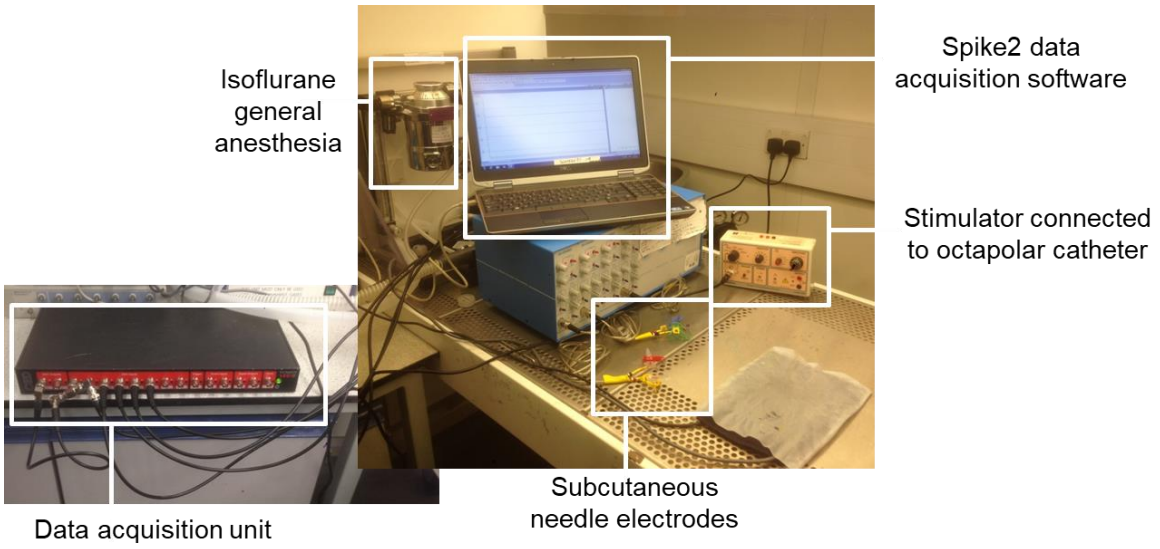

Figure 2.1: Photograph illustrating the Cambridge Electronic Design system for murine electrophysiology. Data was acquired using an Iso-DAM8A amplifier connected to the CED Power 1401-3A interface. ECG signals were sampled at 2000 Hz and displayed in real-time using Spike software (version 2). The transesophageal octapolar catheter is connected to a bipolar stimulus isolation unit and used to deliver programmed electrical stimulations to the left atrium.

2.7.2.2 Transesophageal Atrial Burst Pacing

In order to assess AF susceptibility, the left atrium was paced using an octapolar electrode electrophysiology catheter (CIBer mouse EP catheter, *NuMED Inc.*). First, the catheter was inserted into the oesophagus and placed at the location where the amplitude of the atrial signal from the transesophageal electrodes was maximal. The diastolic pacing threshold was then determined by pacing the atria at a basic cycle length 10-20 ms under the sinus cycle length (typically 100 ms) while slowly changing the position of the catheter and the amperage to find the position with the lowest atrial capture threshold (*i.e.*, the lowest voltage required to achieve 1:1 conduction to the ventricles), which also indicates correct catheter placement at the atria. All subsequent stimulations were delivered at twice the threshold amperage with a stimulus duration of 1 ms. Figure 2.2 shows an ECG lead II recording of the stimulus output during atrial capture. Arrhythmia induction was then tested using a decremental burst pacing protocol that consisted of a 40 stimulus drive train at a cycle length of 60 ms with 2 ms decrements until 10 ms. After each burst, the surface ECG was monitored for evidence of atrial arrhythmias and the protocol was continued only after return to sinus rhythm.

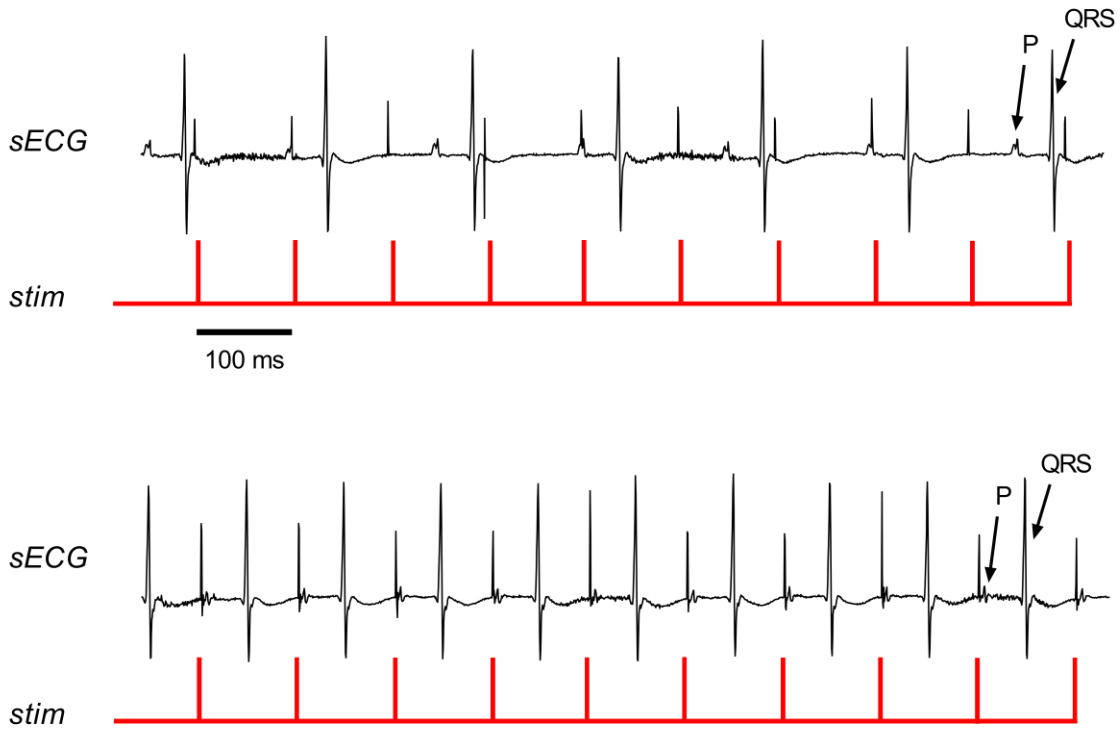

Figure 2.2: Determination of correct catheter placement and atrial capture. A 2-F octapolar catheter is introduced into the esophagus and guided towards the heart. Programmed stimulations are delivered at a coupling interval 10-20 ms below the R-R interval (~90-100 ms) and the catheter is re-positioned until an atrial signal is evoked and successful propagation to the ventricles is observed such that each atrial stimulation (in red) is immediately followed by a P-wave and QRS complex (bottom electrogram). In contrast, if the catheter is not placed near the atria and/or the stimulus amperage is insufficient, a P-wave is not observed immediately following the stimulus, as shown in the top electrogram. sECG – surface electrocardiogram; stim – stimulus output

2.7.2.3 Data Collection and Offline Analysis

ECG data were analysed using Spike 2 software. Standard ECG parameters were measured and averaged from five consecutive beats: R-R interval (RR, cardiac cycle duration), P-Q interval (beginning of the P wave to the beginning of the QRS complex), P wave duration, QRS duration, and corrected QT interval (beginning of the QRS complex to the end of the T wave where the electrogram crosses the isoelectric line). The corrected QT interval (QTc) was calculated as per Bazett's formula (modified for the mouse):

$$\mathrm{QTc} = \mathrm{QT}/\sqrt{(\mathrm{RR}/100)}$$

The mean beat-to-beat RR interval was used to normalize the QT interval as this has been shown to report QTc values within normal physiological range compared to either unadjusted or conventional (RR-adjusted) corrections [215, 216].

The occurrence of AF was identified from the surface ECG by the development of rapid and irregular atrial rhythms, often characterised by the absence of regular P waves, and irregular ventricular activation (see Figure 3.5 of Chapter 3). AF data was then analysed based on arrhythmia duration, initially applying a cut-off of 2 seconds and subsequently 5 seconds and 10 seconds. If burst electrical stimulation provoked arrhythmias that were less than the specified cut-offs or did not evoke an arrhythmic episode at all, the mouse is said to be in sinus rhythm. AF vulnerability was assessed by quantifying the incidence (proportion of mice that developed an episode of AF) and probability (number of arrhythmic episodes divided by the total number of testing manoeuvres applied) of pacing-induced AF. AF duration was measured from the end of the pacing train until the first sinus P wave (Figure 2.3) and maximum (*i.e.*, the longest AF episode in each animal), cumulative (*i.e.*, cumulative sum of all discrete AF episodes in each animal), and mean (*i.e.*, average of all discrete AF episodes in each animal) AF durations were quantified and compared between groups.

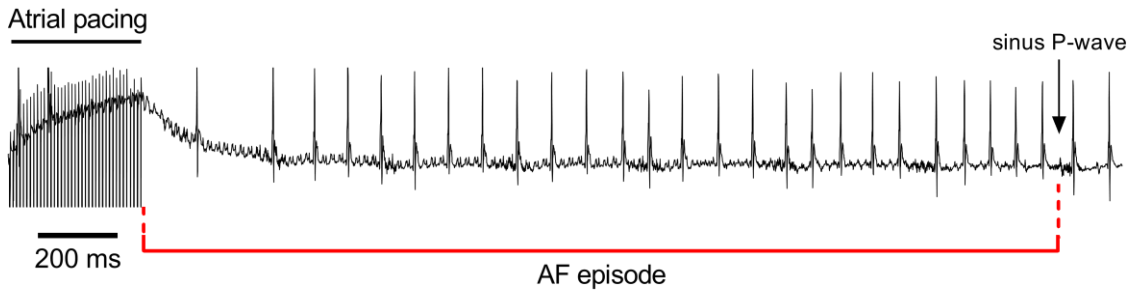

Figure 2.3: Analysis of AF duration. AF was identified by the development of rapid and irregular atrial rhythms on the surface ECG and the duration of each episode was measured from the end of the pacing train until the first sinus P-wave.

2.8 Optical Imaging of Atrial Tissues

A detailed description of the optical imaging system, the experimental protocol and image acquisition, and the tools developed to analyse imaging data is provided in the Methods section of Chapter 5. Briefly, isolated atrial tissues from WT and NOX2-Tg mice were stained with the fluorescent voltage-sensitive dye, di-4-ANEPPS, and the excitation-contraction uncoupler, blebbistatin, over a period of 30 minutes. The tissue was then transferred to a separate chamber and perfusion with warm Krebs-Henseleit solution was started at a constant flow rate to maintain a bath temperature of 35-37°C. The atria were illuminated by an LED source at 545 nm and images (up to 4000 frames) of emitted fluorescence were captured at 1000 frames/sec using a high-resolution camera (128 x 128 pixels, NeuroCMOS-DW128-II, *Cairn Research*) and the GView optical mapping software.

2.9 Studies on Isolated Atrial Myocytes

The following sub-sections describe the procedure for obtaining primary atrial myocytes from mouse hearts and the functional experiments designed to measure intracellular $[Ca^{2+}]_i$ transients and to assess the diastolic leak of Ca^{2+} through RyR2 channels.

2.9.1 Atrial Myocyte Isolation

Mice were injected with heparin (1000 U/mL, *ip*) and sacrificed by Schedule 1 cervical dislocation. The heart was dissected out and rapidly immersed in a Ca^{2+}-free Tyrode solution (in mmol/L: 130 NaCl, 5.6 KCl, 3.5 $MgCl_2$, 5.0 HEPES, 0.4 Na_2PO_4, 20 taurine, 10 glucose, pH 7.4). The lungs, thymus, and fat were carefully removed to expose the aorta which was subsequently inserted onto a cannula (made from a blunted 23 gauge needle) filled with the Ca^{2+}-free solution. A surgical suture thread (Ethicon 5/0 silk) was looped around the aorta and tightened in order to secure the cannula. A second suture was added to ensure adequate filling and perfusion of the atria. The aorta was then cannulated onto a Langendorff perfusion apparatus, taking care not to introduce any bubbles into the coronary circulation, as this is known to affect the isolation procedure. A photograph of the Langendorff apparatus and the Langendorff-perfused heart preparation is shown in Figure 2.4.

The heart was perfused with a Ca^{2+}-free Tyrode solution (maintained at 37 °C) for 3 minutes to clear the blood, and then with a primary enzyme solution (containing 1 mg/mL collagenase type II, 0.233 mg/mL protease, 0.166% BSA, and 50 µmol/L Ca^{2+} in Tyrode solution) for a further 8-10 minutes until the heart was digested. At the end of this period, the heart was detached from the cannula and the left and right atria were separated from the ventricles. Each atria was cut into several pieces and transferred into individual 15 mL cell culture tubes with 500 µL Kraft-Brühe buffer (in mmol/L: 70 glutamic acid potassium salt, 25 KCl, 20 taurine, 20 KH_2PO_4, 3 $MgCl_2$, 0.5 EGTA, 10 glucose, and 10 HEPES). Atrial tissue pieces were gently triturated for 3 minutes in a water bath (37 °C) to disperse the atrial myocytes. The presence of atrial cardiomyocytes was confirmed by microscopic visualization. Freshly isolated cells were stored at room temperature until experiments were performed later that same day.

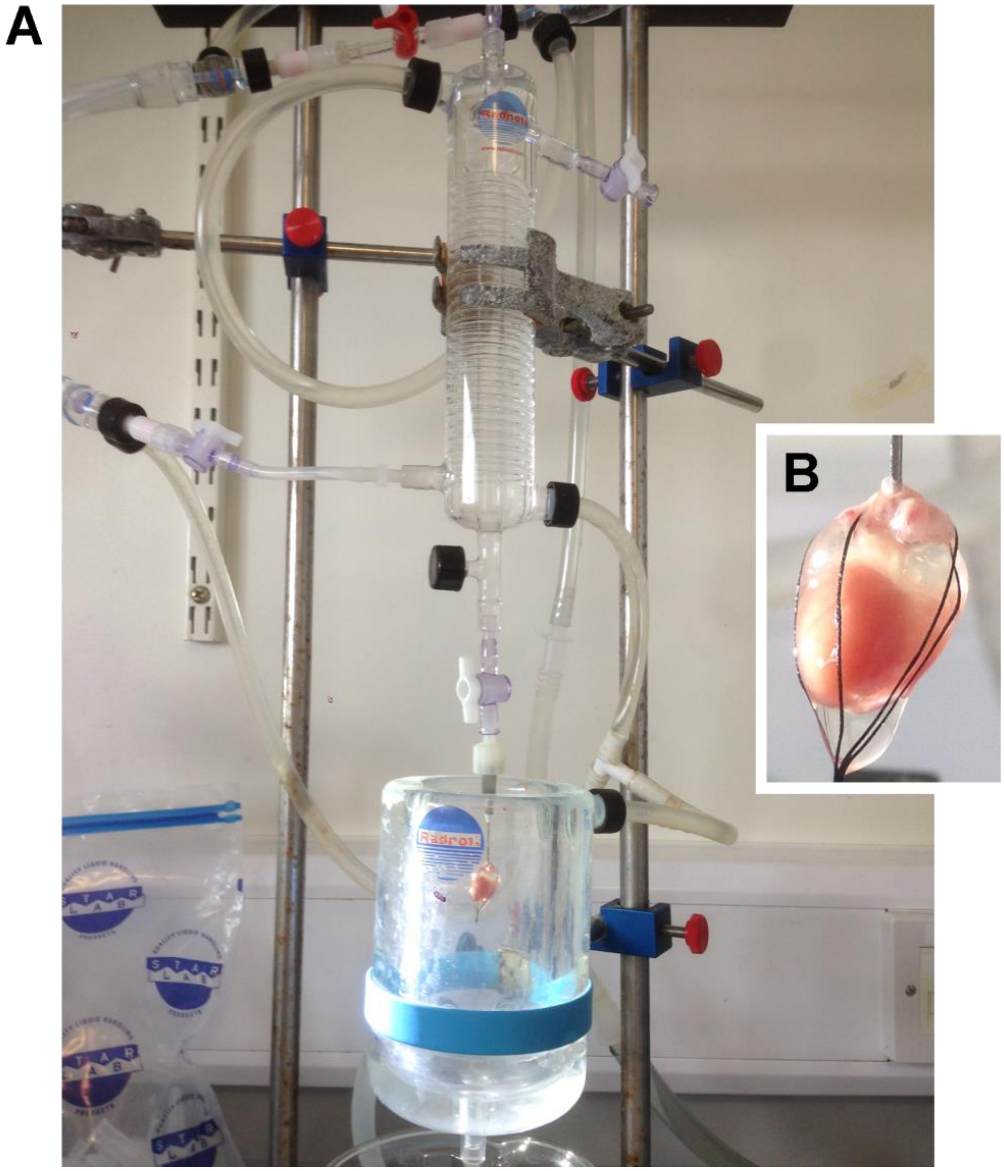

Figure 2.4: Langendorff perfusion system for mouse heart cannulation. A, The heart was attached to a Langendorff perfusion system and perfused with a primary enzyme solution containing collagenase and protease to begin digestion. **B,** Enlarged view of mouse heart cannulation showing adequate filling and perfusion of the atria. LA – left atria; RA – right atria

2.9.2 Measurement of Diastolic Ca^{2+} leak

To monitor $[Ca^{2+}]_i$, freshly isolated atrial myocytes were introduced to Ca^{2+} (0.5 mmol/L Ca^{2+} in Tyrode solution) and loaded with the Ca^{2+}-sensitive, ratiometric, fluorescent dye Fura-2AM (5 µmol/L, ThermoFisher Scientific). An aliquot (500 µL) of atrial myocytes was transferred to an opaque micro-centrifuge tube and incubated with normal Tyrode solution (500 µL) containing 3 µL Fura-2, 500 µmol/L Ca^{2+}, and 2 µL pluronic to aid cell membrane permeability for 8 minutes at room temperature. Myocytes were then centrifuged at 0.4 RCF (relative centrifugal force) for 1 minute and the supernatant containing excess Fura-2 was removed and replaced with 500 µL normal Tyrode solution containing 1 mmol/L Ca^{2+}. Aliquots of 100 µL were incubated with Ang-II (1 µmol/L) for a further 20 minutes before use.

Fura-2-loaded and Ang-II-stimulated atrial myocytes were transferred to a recording chamber with a microscope coverslip floor, mounted on the stage of a high-resolution inverted microscope (Leica Microsystems) which was supported on a pneumatic anti-vibration table (Newport). Once the myocytes had settled, perfusion of a modified Tyrode solution (in mmol/L: 140 NaCl, 5.6 KCl, 3.5 $MgCl_2$, 5 HEPES, 10 glucose, and 1.8 $CaCl_2$) was started and maintained by a speed-adjustable pump at a constant flow rate to ensure a bath temperature of 35 ± 1.5°C (maintained by a passage through a thermal unit situated upstream of the perfusion inflow).

Myocytes were field-stimulated by two electrodes placed at opposite ends of the recording chamber and connected to a digital stimulator (IonOptix Corporation). Electrical stimulation was delivered with 30 V depolarizing pulses at a frequency of 2 Hz. Fura-2 fluorescence was excited by light from a Xenon arc lamp, which was passed through an interference filter (alternately at 365 nm and 380 nm) and reflected up through an 40 X oil-immersion objective (Leica) to the cell. Light collected was restricted to the myocyte of interest through an adjustable aperture. Emitted light was conditioned by photomultiplier tubes filtered at 100 Hz and recorded at 510 nm using a video edge-detection system (IonOptix Corporation). Continuous recordings were displayed by the data acquisition program IonWizard. Background fluorescence measurements (*e.g.,* in the absence of cells) were obtained for each experiment and subtracted for each excitation wavelength. The

Fura-2 fluorescence ratio (*e.g.*, the ratio of the photon live count detected by the excitation at 365 nm compared with that at 380 nm) is proportional to $[Ca^{2+}]_i$.

Diastolic Ca^{2+} leak from RyR2 was measured according to the protocol developed by Shannon *et al*. [217] and modified for atrial myocytes [218]. Myocytes were field-stimulated at 2 Hz and 1.8 mmol/L extracellular $[Ca^{2+}]$ ($[Ca^{2+}]_o$) until $[Ca^{2+}]_i$ transients reached a steady state and were recorded for a further 30 seconds. Pacing was then stopped and the bath solution was rapidly changed to a Na^+-free, Ca^{2+}-free Tyrode solution (with Na^+ replaced by Li^+) containing tetracaine (1 mmol/L, Sigma-Aldrich) for 60 seconds. After this period, the solution was changed again, this time to a Na^+-free, Ca^{2+}-free solution without tetracaine for 90 seconds. The absence of extracellular Na^+ and Ca^{2+} prevents any trans-sarcolemmal Ca^{2+} fluxes and creates a closed system with steady-state $[Ca^{2+}]_i$. At a concentration of 1 mmol/L, tetracaine blocks RyR2 channel opening [219, 220] and thus any Ca^{2+} release through these channels.

The RyR2 Ca^{2+} leak is then quantified as the tetracaine-dependent change in diastolic $[Ca^{2+}]_i$ during the periods of Na^+-free, Ca^{2+}-free Tyrode perfusion. Finally, a pulse of caffeine (10 mmol/L) was applied to the myocyte to release Ca^{2+} from the SR, causing maximal opening of RyR2. The amplitude of the caffeine-induced Ca^{2+} transient was taken as the SR Ca^{2+} content (or load), which was used to assess the leak-load relationship by plotting the RyR2 Ca^{2+} leak against the SR Ca^{2+} content. A sample raw data trace showing the diastolic SR Ca^{2+} leak protocol is reproduced in Figure 6.1 (Methods section of Chapter 6).

$[Ca^{2+}]_i$ transient morphology was assessed as part of the RyR2 leak measurement protocol when myocytes were field-stimulated at 2 Hz in normal Tyrode solution. The amplitude of the $[Ca^{2+}]_i$ transient was calculated by subtracting the baseline (diastolic) $[Ca^{2+}]_i$ from the peak (systolic) $[Ca^{2+}]_i$, and the time constant (tau, τ) was calculated by fitting a second order exponential curve to the transient using specialist software (Axon Clampfit version 8.2.0.233). Measurements from at least 15 seconds of $[Ca^{2+}]_i$ transient recordings were averaged for each cell. The number of myocytes and animals used in each experiment is detailed in the relevant results section.

2.10 Statistics and Data Analysis

All functional studies were performed in a blinded manner (by another scientist) and genotypes were only decoded after completion of the measurements. Group sizes were determined using GPower 3.1 (*Universitat Dusseldorf, Germany*) by power calculations of sample size, applying a power of 80% and α=0.05 (or a 5% significance level). Normality of data sets and statistical significance were assessed using GraphPad Prism 7 (*GraphPad Software Inc.*). Statistical analysis was performed by two-tailed unpaired student's t-test, one-way ANOVA, or two-way ANOVA with Tukey or Bonferonni's *post-hoc* multiple comparisons test, and statistical data expressed as mean ± standard deviation (SD). In the case of non-parametric data, significance was tested by Mann-Whitney *U* test or Kruskal-Wallis test with Dunn's *post-hoc* multiple comparisons test and data expressed as median with 25^{th} and 75^{th} percentiles. Details of the statistical tests used are provided in the Methods section of each chapter and included in each figure legend. The null hypothesis was rejected at a value of $P < 0.05$.

2.11 Materials

A list of materials used in the experiments described above is provided in Table 2.3.

Table 2.3: List of materials and resources

	Source	Identifier
Antibodies		
anti-rabbit RyR2 (Phospho-Ser2814)	Badrilla Ltd.	A010-31
anti-rabbit RyR2 (Phospho-Ser2808)	Badrilla Ltd.	A010-30AP
anti-mouse RyR2	ThermoFisher Scientific	MA3-925
anti-mouse $gp91^{phox}$	BD Transduction Lab.	611414
Monoclonal anti-GAPDH peroxidase	Sigma Aldrich	G9295
Chemicals		
Angiotensin II	Sigma Aldrich	A9525
Blebbistatin	RD Systems	1760
Caffeine	Sigma Aldrich	C0750
di-4-ANEPPS	Sigma Aldrich	D8064
Fura-2 AM	ThermoFisher Scientific	F1221
NADPH	Sigma Aldrich	N5130
Pluronic F-127, 20% solution in DMSO	Sigma Aldrich	59004
Pierce protease inhibitor mini tablets	ThermoFisher Scientific	88665
cOmplete mini protease inhibitor tablets	Sigma Aldrich	11836153001
RIPA (10X)	Sigma Aldrich	20-188
TaqMan		
Tetracaine	Sigma Aldrich	T7383
Tiron	Sigma Aldrich	172553
Commercial Assays		
Amplex Red Cholesterol Assay Kit	ThermoFisher Scientific	A12216
BCA Protein Assay Kit	ThermoFisher Scientific	23225
mirVana miRNA Isolation Kit	ThermoFisher Scientific	AM1561
QuantiTect Reverse Transcription Kit	Qiagen	205313
RNeasy Mini Kit	Qiagen	74104
TaqMan Gene Expression Master Mix	ThermoFisher Scientific	4369016

	Source	**Identifier**
Oligonucleotides		
NOX2, murine	ThermoFisher Scientific	Mm001287743_m1
NOX2, human	ThermoFisher Scientific	Hs00166163_m1
ACTN2, murine	ThermoFisher Scientific	Mm00473657_m1
GAPDH, murine	ThermoFisher Scientific	Mm99999915_g1
Software and Algorithms		
Ccoffinn toolkit	Tomek *et al.* [221]	
Clampfit version 8.2.0.233	Molecular Devices	
GPower version 3.1	Universitat Dusseldorf	
GraphPad Prism version 7.0a	GraphPad Software Inc.	
GView	Dr Gil Bub, McGill University	
lmerTest R package	Sikkel *et al.* [222]	
MATLAB version 2015a	MathWorks	
Spike 2 version 7.09a	Cambridge Electronic Design	

2.12 Technical Contributions

I was responsible for the planning and primary data collection of the following: cardiac mRNA expression of NOX2, surface ECG measurements and *in vivo* transesophageal atrial burst pacing, optical mapping of isolated atrial tissues (including development and validation of the technique), analysis of optical imaging data, measurement of Ca^{2+} transients and assessment of diastolic Ca^{2+} leak in atrial myocytes, RyR2 phosphorylation in atrial tissues. I was also responsible for analyzing all of the data (excluding molecular experiments performed by others), performing statistical analysis, and generating all figures.

The following parts of my thesis are not exclusively my own work: In Chapter 3, Dr Alice Recalde performed the western blots for assessment of NOX2 protein expression (with technical contributions from Dr Jillian Simon), measurements of NADPH-stimulated $O_2 \cdot^-$ production in atrial tissues by HPLC, and a portion of the *in vivo* transesophageal burst pacing experiments. Dr Ricardo Carnicer performed the mouse echocardiography experiments. In Chapter 4, Dr Alice Recalde performed the *in vivo* transesophageal burst pacing experiments and cholesterol assays in placebo and atorvastatin-treated animals. All electrocardiograms were analyzed by myself (including measurements of ECG parameters and AF susceptibility). In Chapter 5, Dr Klemen Ziberna wrote the majority of the MATLAB scripts used to measure atrial APD.

3 Myocardial NOX2 Overexpression Promotes AF

3.1 Introduction

As highlighted in Chapter 1, AF is associated with elevations in atrial ROS production, in particular elevated $O_2^{\cdot -}$ due to the increased activity of NADPH oxidases. In large animal models, induction of AF by rapid atrial pacing is accompanied by increased NADPH oxidase activity and $O_2^{\cdot -}$ production in the left atrium [137, 138]. Circumstantial evidence implicates the $gp91^{phox}$-containing NADPH oxidases (NOX2) in mediating these effects. For instance, in the study by Dudley *et al.* [137], NADPH oxidase-dependent $O_2^{\cdot -}$ release was associated with an increase in the activated form of GTP-bound Rac1 (critical for NOX2 activation), although expression of $p22^{phox}$ and NOX2 remained unchanged. Reilly *et al.* [138], meanwhile, showed increased NOX2 and $p22^{phox}$ expression after two weeks of pacing-induced AF in a goat model, which returned to baseline within six months.

These findings are further supported by clinical studies. Kim *et al.* [128] were the first to report an association between NADPH oxidase-derived $O_2^{\cdot -}$ production and AF in patients. Using a range of substrates and inhibitors for selective ROS-generating enzymes, the authors first investigated the sources of $O_2^{\cdot -}$ production in the human atrial myocardium. Basal $O_2^{\cdot -}$ release was detected in right atrial tissue homogenates and isolated myocytes of sinus rhythm patients, and was markedly increased by NADPH (a substrate for NADPH oxidases). Both basal and NADPH-stimulated $O_2^{\cdot -}$ release were reduced by inhibition of NADPH oxidases with apocynin (a pan-isoform inhibitor) or DPI (inhibitor of flavin-containing oxidases), while inhibition of other ROS sources including mitochondrial complex I, NOS, and xanthine oxidase had no effect. Furthermore, analysis of right atrial samples (tissue homogenates and isolated myocytes) in patients with a history of AF (paroxysmal/persistent) showed significantly elevated $O_2^{\cdot -}$ production and NADPH

oxidase activity when compared to patients in normal sinus rhythm. The authors concluded that NADPH oxidases are the main source of superoxide in human atrial cardiomyocytes and further pointed to NOX2 as the candidate isoform based on expression studies which confirmed the presence of the NOX2 enzymatic complex ($gp91^{phox}$, $p22^{phox}$, $p47^{phox}$, $p67^{phox}$), but not its homologues NOX1 or NOX4, in isolated atrial myocytes.

A number of studies have also reported an increase in NADPH oxidase-dependent $O_2^{\cdot -}$ production in post-operative AF patients where it was shown to be predictive of new onset AF after cardiac surgery, as well as other in-hospital complications [142, 143]. Subsequent work found a Rac1-dependent activation of NADPH oxidases in post-operative AF that was increased along with expression of NOX2 and $p22^{phox}$ [138, 142]. Using atorvastatin to inhibit Rac1 activity in right atrial homogenates from AF patients, Reilly *et al*. [138] observed a decrease in NADPH-stimulated $O_2^{\cdot -}$ production and membrane translocation of $p47^{phox}$ and $p67^{phox}$ (critical for NOX2 activation) to normal levels (*i.e.* similar to sinus rhythm). Similar findings were obtained by pre-operative treatment with atorvastatin (40 mg/day for 3 days) which reduced the amount of active GTP-bound Rac1 and significantly lowered NADPH-stimulated and apocynin-inhibitable $O_2^{\cdot -}$ [142].

Despite these positive accounts implicating NOX2-derived $O_2^{\cdot -}$ in AF, direct experimental evidence linking NOX2 activity to the initiation and/or maintenance of AF has not been demonstrated. The work in this chapter follows on from these findings to test the hypothesis that $O_2^{\cdot -}$ released specifically from NOX2 oxidases directly contributes to the development of AF *in vivo.* An established transgenic mouse model which specifically expresses a human *NOX2* transgene (NOX2-Tg) in the heart was chosen as a model of increased myocardial NOX2 activity and used to test this hypothesis. In this chapter, *in vivo* work assesses cardiac rhythm and atrial arrhythmia susceptibility as a result of increased atrial NOX2 activity.

3.2 Methods

The following procedures were performed in this chapter as described in detail in Chapter 2:

- 2.2 Tissue Collection and Processing
- 2.3 RNA Isolation and Quantitative Reverse Transcription PCR
- 2.4 Western Blot Analysis
- 2.5 Measurement of $O_2^{\cdot -}$ Production
    - 2.5.1 Detection of Dihydroethidium Oxidation Products by HPLC
- 2.7 In-Vivo Interventions
    - 2.7.1 Echocardiography
    - 2.7.2 Electrophysiology
        - 2.7.2.1 Surface ECG Recordings
        - 2.7.2.2 Transesophageal Atrial Burst Pacing
        - 2.7.2.3 Data Collection and Offline Analysis
- 2.10 Statistical Analysis

Additional details relevant to this chapter are provided below.

3.2.1 RNA Isolation and Quantitative Reverse Transcription PCR

Gene expression in atrial and ventricular tissues was determined as described in Section 2.3 of Chapter 2 using TaqMan gene expression assays (ThermoFisher Scientific) for murine *NOX2*, human *NOX2*, α-actinin2 (*ACTN2*) and *GAPDH*. To determine the best gene for transcript normalization, the Ct values and standard deviations of *ACTN2* and *GAPDH* were compared between genotypes (Table 3.1) and between tissues (Table 3.2). There were no significant differences in mean Ct values between genotypes, however, *GAPDH* had the lowest standard deviation of Ct values across all tissue samples and the smallest statistical differences between cardiac tissue samples (from WT and NOX2-Tg mice combined) and was therefore chosen as the reference gene for further analysis.

Table 3.1: Comparison of mean Ct values between genotypes

	ACTN2		*GAPDH*	
	WT	**NOX2-Tg**	**WT**	**NOX2-Tg**
RA	20.3 ± 0.13	20.2 ± 0.18	18.5 ± 0.26	18.6 ± 0.3
LA	19.9 ± 0.12	19.9 ± 0.14	18.4 ± 0.06	18.0 ± 0.19
LV	19.3 ± 0.18	19.3 ± 0.17	17.9 ± 0.19	17.9 ± 0.13

Data shown are mean ± SD of Ct values.

Table 3.2: Mean Ct values of housekeeping genes

	RA (n = 16)	**LA (n = 16)**	**LV (n = 16)**	**All (n = 48)**
ACTN2	20.2 ± 0.15	19.9 ± 0.13 #	19.3 ± 0.17 *	19.8 ± 0.42
GAPDH	18.5 ± 0.20	18.5 ± 0.23	17.9 ± 0.16 *	18.3 ± 0.35

Data shown are mean ± SD of Ct values from WT and NOX2-Tg samples combined. * $P < 0.0001$ vs RA and LA; # $P < 0.0001$ vs RA

Human *NOX2* gene expression was then quantified by calculating the ΔCt values for each sample according to the equation below and relative expression is presented as $2^{-\Delta Ct}$.

$$\Delta Ct = Ct(\text{human } NOX2) - Ct(GAPDH)$$

Expression of the endogenous mouse *NOX2* isoform was quantified by first calculating the ΔCt values for each sample and then the ΔΔCt values according to the following equations:

$$\Delta Ct = Ct(\text{mouse } NOX2) - Ct(GAPDH)$$

$$\Delta\Delta Ct = \Delta Ct(\text{sample}) - \Delta Ct(\text{mean of WT})$$

Results for mouse *NOX2* are presented as relative expression to WT controls, calculated by $2^{-\Delta\Delta Ct}$.

3.2.2 Western Blot Analysis

Sample preparation for western blotting was carried out as described in Section 2.4 of Chapter 2. Atrial tissue homogenates were loaded onto NuPage 4-12% Tris-Acetate gradient gels and transferred onto nitrocellulose membranes. Antibodies used were: anti-mouse $gp91^{phox}$ (*BD Transduction*) and HRP-conjugated GAPDH (*Sigma Aldrich*).

3.2.3 Statistical Analysis

All functional studies performed by the author were done in a blinded manner and genotypes were only decoded after completion of the measurements. Group sizes were determined using GPower 3.1 (*Universitat Dusseldorf, Germany*) by power calculations of sample size, applying a power of 80% and a 5% significance level ($\alpha = 0.05$). Normality of data sets and statistical significance were assessed using GraphPad Prism 7 (*GraphPad Software Inc.*). Statistical analysis was performed by two-tailed unpaired student's t-test or one-way ANOVA with Bonferonni's *post-hoc* multiple comparison, as deemed appropriate and statistical data expressed as mean ± SD. In the case of non-parametric data, significance was tested by Mann-Whitney *U* test or Kruskal-Wallis test with Dunn's *post-hoc* multiple comparison and data expressed as median with 25^{th} and 75^{th} percentiles or box and whisker plot: minimum to maximum. Details of the statistical tests used are included in the Methods section of each chapter and in each figure legend. The null hypothesis was rejected at a value of $P < 0.05$.

3.3 Results

3.3.1 Myocardial NOX2 expression and $O_2^{\cdot -}$ production

Transgenic mice with cardiomyocyte-targeted overexpression of NOX2 (NOX2-Tg) were generated previously and found to have approximately 5-fold higher NOX2 protein levels in the ventricular myocardium compared with WT controls [207]. To study the effect of elevated NOX2 in the atria, we first sought to determine whether transgenic expression could be detected in the atrial myocardium of these mice. Expression of the human *NOX2* transcript was assessed by quantitative RT-PCR and detected in the LV, LA, and RA of NOX2-Tg mice (Figure 3.1-A). Analysis of cardiac tissue distribution revealed greater (~3-fold) expression of the transgene in the LV compared with the LA and RA ($P<0.05$) of NOX2-Tg mice, with no differences between the atrial chambers. As expected, human *NOX2* mRNA was not detected in WT animals. The expression of murine *NOX2* mRNA was not affected by the transgene, as can be seen from the similarity in the expression of mouse *NOX2* mRNA between NOX2-Tg mice and their WT littermates in the LV, LA, and RA. Irrespective of genotype, the relative expression of murine *NOX2* mRNA was higher in the RA compared with the LA ($P<0.05$) and LV ($P<0.001$), as shown in Figure 3.1-B.

To determine whether the human *NOX2* mRNA is translated into protein, immunoblotting for NOX2 was performed. A monoclonal anti-$gp91^{phox}$ antibody was used and a 58 kDa band was detected in atrial tissue homogenates from both WT and NOX2-Tg mice (Figure 3.2-A), suggesting cross-reaction with the endogenous murine NOX2 isoform. Protein sequence alignment in NCBI Protein Basic Local Alignment Search Tool (BLAST) identified 93% homology between the murine (UniProt: Q3U6G0) and human (UniProt: P04839) sequences, and 96% homology between the human sequence and the antibody epitope which is directed against amino acids 450-556 of the murine $gp91^{phox}$ subunit. Nevertheless, the total amount of NOX2 (both endogenous and transgenic NOX2) produced by NOX2-Tg mice in the atria was higher than that produced by WT mice; compared with WT, transgenic mice displayed approximately 3-fold and 3.5-fold higher

expression of NOX2 in RA (P=0.015, Mann-Whitney U test; Figure 3.2-B) and LA (P=0.0025, Mann-Whitney U test; Figure 3.2-C) tissue homogenates, respectively.

To investigate whether NOX2 is overexpressed as a functional enzyme, $O_2{\cdot}^-$ production in atrial tissue homogenates was determined by HPLC-based quantification of 2-OHE, according to the methods described in Section 2.5.1 of Chapter 2. Atrial tissue lysates were incubated for 15 minutes in Krebs-HEPES buffer containing DHE (50 µmol/L), a fluorescent compound that specifically produces 2-OHE when it reacts with $O_2{\cdot}^-$ [213]. To stimulate NOX2 activity, atrial tissue homogenates were incubated for 15 minutes with NADPH (100 µmol/L), a substrate for NOX2. Specificity for $O_2{\cdot}^-$ was determined by co-incubation with tiron (100 mmol/L), a cell-permeable $O_2{\cdot}^-$ scavenger, before the addition of DHE, and the tiron-inhibitable fraction of the 2-OHE signal was quantified and compared between genotypes. As illustrated in the HPLC chromatograms in Figure 3.3-A, formation of 2-OHE, which reflects the amount of $O_2{\cdot}^-$ produced in the tissue during the incubation with NADPH, was higher in NOX2-Tg atrial tissues when compared with WT. Quantification of the tiron-inhibitable fraction of the 2-OHE signal demonstrates that NADPH-stimulated $O_2{\cdot}^-$ production was significantly higher in both atria of NOX2-Tg mice (in RA homogenates: P=0.0019 *vs* WT, Mann-Whitney U test, Figure 3.3-B; in LA homogenates: P=0.004 *vs* WT, Mann-Whitney U test, Figure 3.3-C).

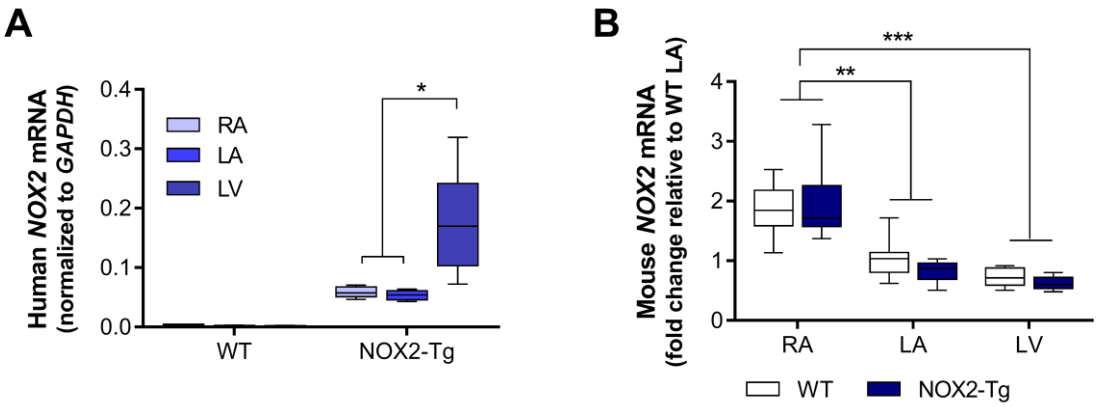

Figure 3.1: mRNA expression of human and mouse *NOX2* genes in WT and NOX2-Tg hearts. A, Quantitative RT-PCR detection of the human *NOX2* mRNA transcript confirms the presence of the transgene in the LV, RA, and LA of NOX2-Tg hearts. Human *NOX2* mRNA expression is significantly higher in the LV (*P<0.01 vs RA and LA, Kruskal-Wallis with Dunn's multiple comparisons test, n = 8/group), with no differences in expression between the atrial chambers (P>0.05). **B,** Expression of mouse *NOX2* mRNA is significantly higher in the RA (**P<0.05 *vs* LA, one-way ANOVA and ***P<0.001 *vs* LV, Kruskal-Wallis with Dunn's multiple comparison's test), with no differences between genotypes. Data shown as box and whisker plot: minimum to maximum.

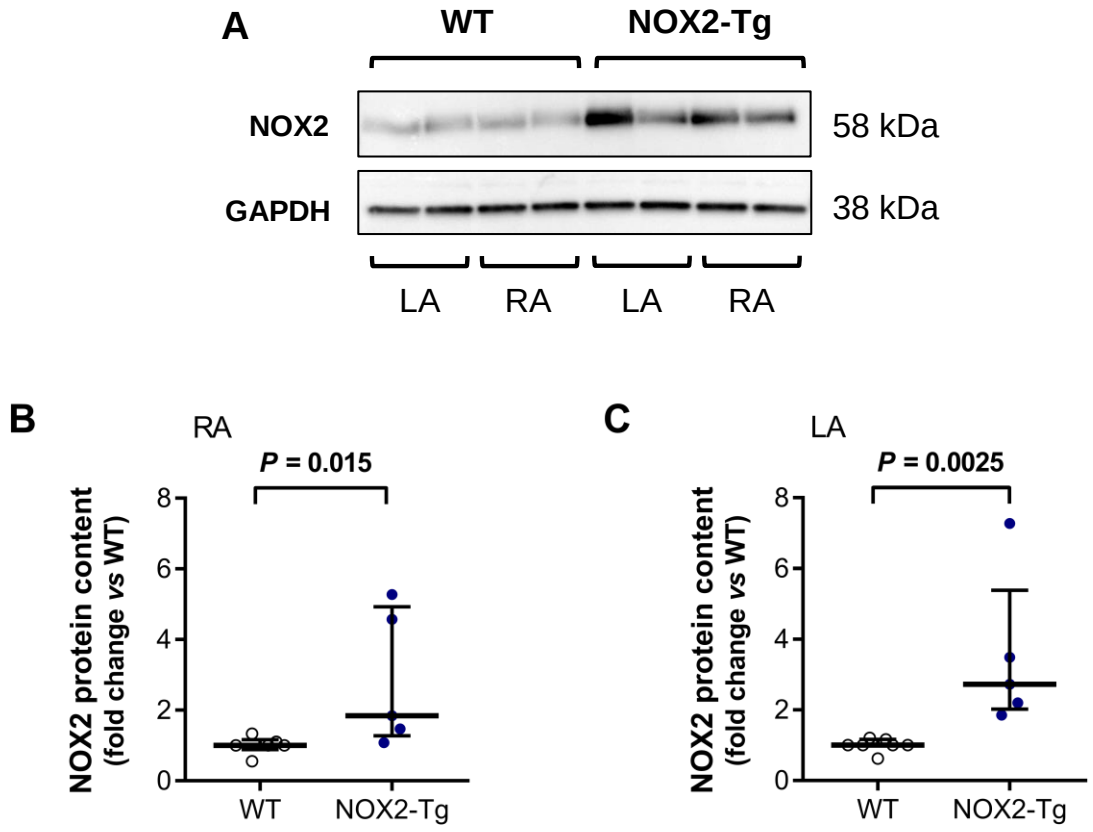

Figure 3.2: Atrial NOX2 protein expression. A, NOX2 protein expression was assessed by western blot with a monoclonal anti-gp91^{phox} antibody. Western blot detection of a 58 kDa NOX2 protein in atrial tissue homogenates from WT and NOX2-Tg mice is shown. NOX2 protein content is significantly higher in NOX2-Tg hearts in both RA (**B,** *P*=0.015 *vs* WT, Mann-Whitney *U* test, n=6 for WT and n=5 for NOX2-Tg) and LA (**C,** *P*=0.0025 *vs* WT, Mann-Whitney *U* test, n=7 for WT and n=5 for NOX2-Tg; **C**) tissue homogenates. Data are normalized initially to the reference protein, GAPDH, and then to the average of WT within each tissue and reported as a fold change relative to WT. Data shown are individual values with median ± interquartile range.

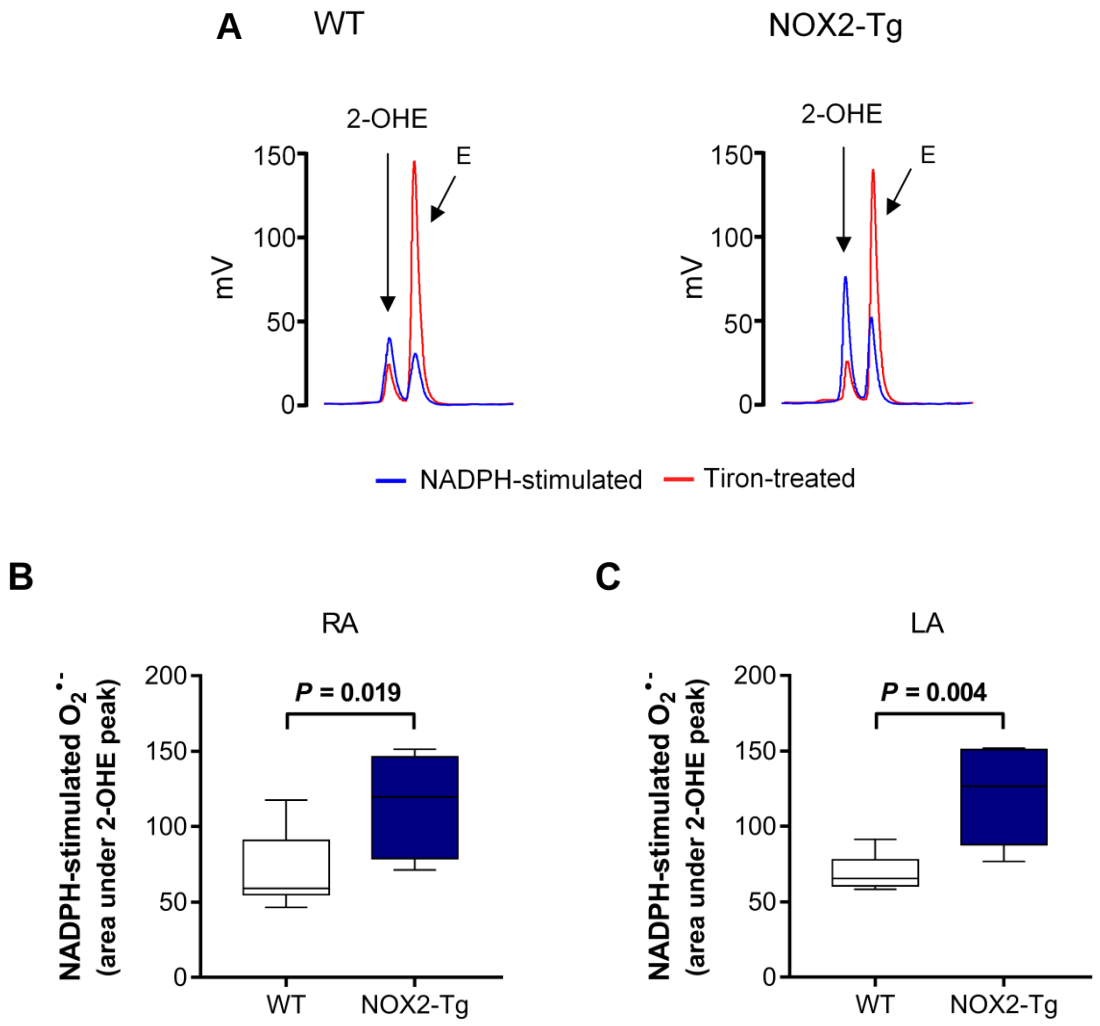

Figure 3.3: NADPH-stimulated $O_2^{\bullet-}$ production is higher in NOX2-Tg atrial tissue homogenates. **A,** HPLC chromatograms showing the formation of 2-hydroxyethidium (2-OHE), the $O_2^{\bullet-}$-derived oxidation product of DHE, and ethidium (E), the non-specific two-electron oxidation product, in LA homogenates. Samples were incubated with NADPH (100 µM, —) for 15 min to stimulate oxidase activity and tiron (100 mM, —) for an additional 15 min to confirm specificity for $O_2^{\bullet-}$. The tiron-inhibitable fraction of 2-OHE (*i.e.*, the difference in the area under the 2-OHE peak between NADPH and tiron) was taken as a measure of the NADPH-stimulated $O_2^{\bullet-}$ production and found to be significantly higher in NOX2-Tg RA (**B,** P=0.019 *vs* WT, Mann-Whitney *U* test, n=8 for WT and n=5 for NOX2-Tg) and LA (**C,** P=0.004 *vs* WT, Mann-Whitney *U* test, n=7/genotype). Data shown as box and whisker plot: maximum and minimum.

3.3.2 *In vivo* assessment of cardiac function and morphology

Growing evidence links NOX2-derived ROS to the development of LV hypertrophy [207, 223], a major risk factor for AF [27]. In this regard, the overexpression of NOX2 in the LV (Figure 3.1-A and ref. [207]) could potentially confound the association between atrial NOX2 activity and AF. To address this concern, we assessed cardiac function and morphology using 2-D M-mode echocardiography. As shown in Table 3.3, we observed significantly higher LV posterior wall thickness at end-diastole in NOX2-Tg mice (P=0.009 *vs* WT, un-paired Student's t-test), without any differences in diastolic (P=0.43) or systolic (P=0.86) internal diameters, and ejection fraction (P=0.95) between genotypes. In addition, LV mass and indexed LV mass showed an upward trend but the differences were not statistically different between groups (P>0.05).

Diastolic function as measured by tissue doppler imaging also appeared to be preserved; there were no significant differences in the E/A ratio (a ratio of early peak aortic velocity of mitral diastolic flow (E-wave) to late peak velocity of mitral diastolic flow from atrial contraction (A-wave)), the E'/A' ratio (a ratio of early tissue Doppler mitral annulus velocity (E') to late tissue Doppler mitral annulus velocity (A')), or the isovolumetric relaxation and contraction times (IVRT and IVCT, respectively) between genotypes. The E/E' ratio (ratio of mitral inflow E wave to tissue Doppler mitral annulus velocity), which correlates with left atrial pressure, was also similar between WT and NOX2-Tg mice.

Table 3.3: Left ventricular structure and function assessed by echocardiography

	WT	NOX2-Tg	*P*-value
n	*20*	*15*	
Male/Female	8/12	5/10	
Body weight (g)	23.2 ± 3.83	23.8 ± 5.48	0.71
Heart rate			
Baseline HR (bpm)	483 ± 29	488 ± 26	0.61
HR for diastolic measurements	349 ± 39	369 ± 20	0.16
LV dimensions			
LV diastolic posterior wall (mm)	**0.85 ± 0.11**	**1.02 ± 0.24**	**0.009****
LV systolic posterior wall (mm)	1.29 (1.19 – 1.45)	1.37 (1.26 – 1.59)	0.18
LV diastolic internal diameter (mm)	3.57 (3.28 – 3.78)	3.51 (3.25-3.65)	0.43
LV systolic internal diameter (mm)	2.11 (1.92 – 2.32)	2.08 (1.82 - 2.34)	0.86
LV diastolic volume (µL)	53.3 (43.3 – 61.3)	51.2 (42.7 – 56.3)	0.43
LV systolic volume (µL)	14.5 (11.5 – 18.4)	14.1 (1.0 – 19)	0.86
Indexed LV diastolic volume (µL/g)	2.31 (2.06 – 2.49)	2.18 (1.72 – 2.61)	0.26
Indexed LV systolic volume (µL/g)	0.64 (0.5 – 0.8)	0.68 (0.34 – 0.83)	0.99
LV mass			
LV mass (mg)	85.4 (73.4 – 109)	100 (89.2 – 110)	0.15
Indexed LV mass (mg/g)	3.89 (3.30 – 4.73)	4.41 (3.47 – 4.76)	0.39
LV systolic function			
LV ejection fraction (EF, %)	71.5 ± 9.68	71.3 ± 8.98	0.95
Fractional shortening (FS, %)	40.7 ± 8.33	40.3 ± 7.42	0.89
LV diastolic function			
Mitral valve E/A ratio	1.80 (1.5 – 2.0)	1.77 (1.6 – 2.0)	0.95
Tissue Doppler E'/A' ratio	1.39 (1.25 – 1.67)	1.33 (1.24 – 1.67)	0.74
Combined E/E' ratio	30.6 ± 6.74	28.8 ± 4.15	0.49
Cardiac times			
IVCT (ms)	20.7 ± 6.4	23.1 ± 6.7	0.44
IVRT (ms)	21.5 (20.4 - 23.6)	22.3 (20.5 – 25.3)	0.81

Echocardiographic measurements evaluating left ventricular mass, and systolic and diastolic function of anesthetized WT and NOX2-Tg mice. Data shown are mean ± SD or median (25^{th} to 75^{th} percentiles). Parametric data were analysed by a two-tailed un-paired Student's t-test and non-parametric data were analysed using a Mann-Whitney *U* test. *N* – number of mice; HR – heart rate; bpm – beats per minute; E – early mitral valve inflow velocity (passive filling); A – late mitral valve inflow velocity (active filling); E' – early tissue Doppler mitral valve annulus velocity; A' – late tissue Doppler mitral valve annulus velocity; IVCT – isovolumetric contraction time; IVRT – isovolumetric relaxation time.

3.3.3 *In vivo* analysis of cardiac rhythm

WT and NOX2-Tg mice further underwent surface ECG monitoring under general anesthesia to assess the role of NOX2-derived $O_2^{\cdot -}$ in cardiac rhythm stability. As shown in Table 3.4 and Figure 3.4, there was a small but significant increase (P=0.038, un-paired Student's t-test, Figure 3.4-A) in the RR interval of NOX2-Tg mice (142 ± 20 ms) compared with WT controls (135 ± 18 ms), which indicates a reduction in heart rate. NOX2-Tg mice also had significantly longer QT intervals (58 ± 8.93 ms, P=0.04, un-paired Student's t-test) compared with WT (54.9 ± 8.24 ms; Figure 3.4-B); however, this difference did not persist when QT was corrected for heart rate (QTc, 47.5 ± 6.82 ms for WT *vs* 49 ± 7.63 ms for NOX2-Tg, P=0.23; Figure 3.4-D). The rate correction was necessary as QT interval duration showed a positive, albeit small, correlation with the RR interval (Pearson coefficient, r=0.196, P=0.029; Figure 3.4-C). No other differences in ECG parameters were statistically significant between groups, as summarized in Table 3.4.

Table 3.4: Standard electrophysiology parameters

	WT	**NOX2-Tg**	***P*-value**
n	*63*	*61*	
Male (%)	32 (51)	29 (48)	
RR, ms	**135 ± 18**	**142 ± 20**	**0.037***
P wave, ms	22.4 (21.2 – 24.1)	23 (21.6 – 24.3)	0.32
PQ, ms	40.7 ± 3.27	41.0 ± 3.84	0.67
QRS, ms	8.1 (7.71 - 8.93)	8.2 (7.18 - 9.4)	0.58
QT, ms	**54.9 ± 8.24**	**58 ± 8.93**	**0.041***
QTc, ms	47.5 ± 6.82	49 ± 7.63	0.23

Comparison of surface ECG parameters obtained from anesthetized WT and NOX2-Tg mice. Data shown are mean ± SD or median (25^{th} to 75^{th} percentile). *P*-values were calculated by a two-tailed un-paired Student's t-test or Mann-Whitney *U* test, as appropriate. *N* – number of mice, RR – R-R interval denoting the cardiac cycle duration, P wave – duration of atrial depolarization and repolarization, PQ – interval from the start of the P wave to the start of the QRS complex, QRS – ventricular depolarisation time, QT – duration of ventricular depolarisation and repolarisation, QTc – QT interval corrected for heart rate. *$P<0.05$

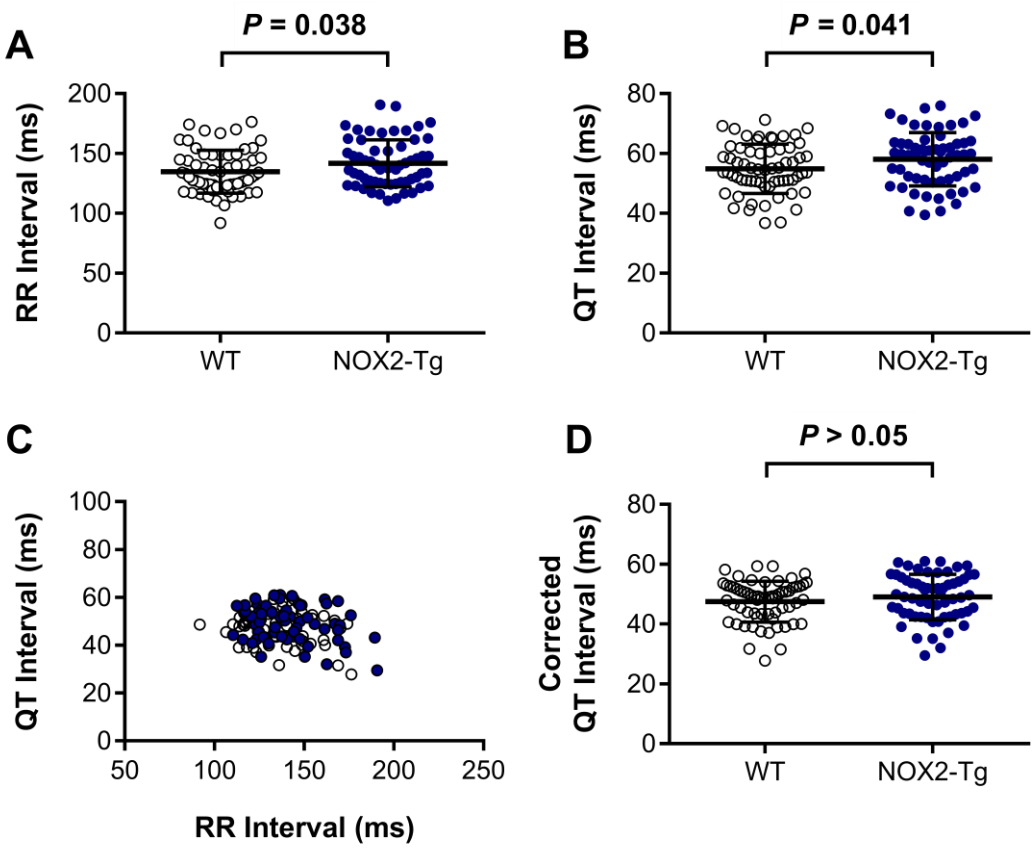

Figure 3.4: QT and RR intervals in anesthetized WT and NOX2-Tg mice. NOX2-Tg mice display longer RR intervals (**A,** *P*=0.038 *vs* WT, un-paired Student's t-test, **A**) and QT intervals (**B,** *P*=0.041 *vs* WT, un-paired Student's t-test). **C,** Relationship between the observed QT and RR intervals showing a small positive correlation in WT (○) and NOX2-Tg (●) mice (Pearson correlation coefficient, r=0.196, r^2=0.038, *P*=0.0291). **D,** When corrected for heart rate, the QT interval (QTc) is similar between WT (47.5 ± 6.82 ms) and NOX2-Tg mice (49.0 ± 7.63 ms, *P*=0.23 with un-paired Student's t-test). Data shown are individual values with mean ± SD. n=63 WT and n=61 NOX2-Tg mice.

3.3.4 NOX2-Tg mice display increased susceptibility to pacing-induced AF

A major objective of this study was to determine whether NOX2-derived $O_2^{\cdot -}$ production directly contributes to the development of AF. In the mouse, induction of AF by direct electrical stimulation of the atria can serve as an indicator for atrial vulnerability *in vivo*. To that end, we assessed the inducibility of AF by transesophageal atrial burst pacing in NOX2-Tg mice and their WT littermates, as described in Section 2.7.2.2 of Chapter 2. Neither group displayed spontaneous arrhythmic events; nevertheless, analysis of surface ECG traces after burst pacing revealed frequent episodes of atrial arrhythmias resembling AF and atrial flutter, as shown in Figure 3.5. Typical ECG characteristics of AF included absent P-waves, increased R-R interval variance, and evidence of rapid and irregular atrial activity, while atrial flutter manifested as a rapid, but regular atrial rhythm. Frequent transition between flutter and AF was inconsistently observed (Figure 3.5, bottom panel), especially during long-lasting episodes (minutes *vs* seconds). For simplicity of the data analysis and because the absence/presence of distinct P-waves could not be reliably distinguished in all recordings (due to sinusoidal interference in the ECG signal), both forms of atrial arrhythmias were grouped together and labelled as AF.

To examine the connection between NOX2 activity and AF, I first compared the sensitivity of NOX2-Tg and WT mice to AF induction by transesophageal pacing. AF episodes less than 2 seconds in duration were not included in the analysis. This was decided because large stimulation artefacts obscured atrial electrogram recordings immediately after each burst and identification of AF on the surface ECG was more reliable when a duration greater than 2 seconds was evaluated. As documented in Figure 3.6-A, atrial burst pacing provoked AF (with episodes lasting $\geq$ 2 seconds) in significantly more NOX2-Tg mice (P=0.023 *vs* WT, Fisher's exact test). Among those animals with inducible AF (40/57 WT and 49/56 NOX2-Tg), the probability of AF induction (*e.g.*, the number of AF episodes divided by the total number of burst stimulations delivered to the atria) was quantified and found to be similar between genotypes (WT: 9.3% [25^{th} to 75^{th} percentile: 4.17 to 15.6%] *vs* NOX2-Tg: 11.5% [25^{th} to 75^{th} percentile: 4.03 to 15.9%], P=0.83, Mann-Whitney U test).

In order to evaluate the induction of 'sustained' fibrillatory activity, I also quantified the sensitivity to develop AF lasting greater than 5 seconds and greater than 10 seconds. Although not statistically different, there was a trend towards more NOX2-Tg mice developing AF with episodes ≥5 sec (45/56 NOX2-Tg *vs* 36/57 WT, P=0.06 Fisher's exact test, Figure 3.6-B) and ≥10 sec (43/56 NOX2-Tg *vs* 35/57 WT, P=0.1, Fisher's exact test, Figure 3.6-C), with no differences in AF probability between groups, as shown in Figure 3.6-B and Figure 3.6-C.

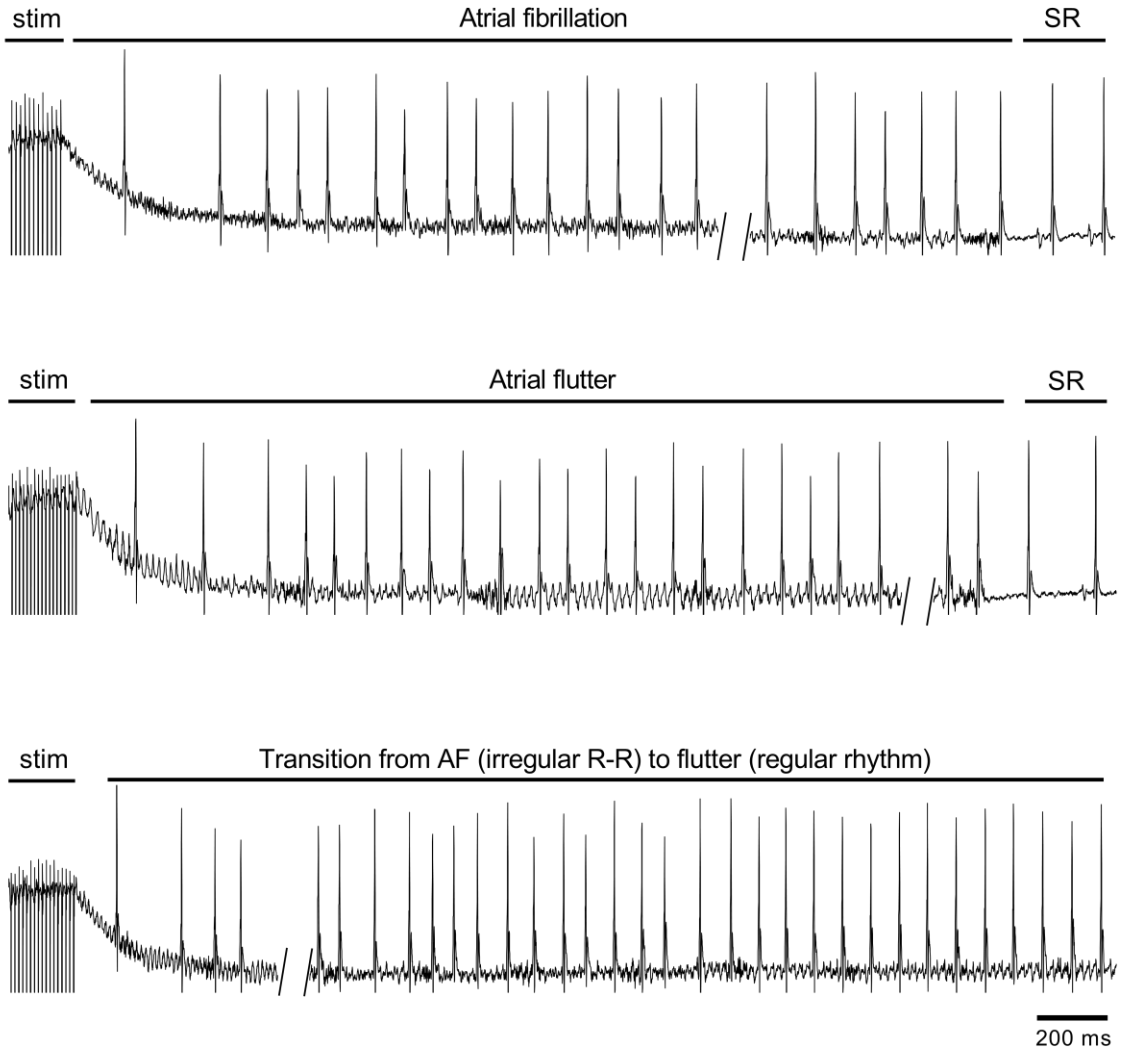

Figure 3.5: Atrial tachyarrhythmias induced by transesophageal atrial burst pacing. Surface ECG recordings illustrate episodes of atrial tachyarrhythmias resembling AF (*upper panel*) and atrial flutter (*middle panel*). Typical ECG characteristics of AF included absent P-waves and increased R-R interval variance, while atrial flutter manifested as a rapid, but regular atrial rhythm. Frequent transition between flutter and AF was inconsistently observed (*bottom panel*). These types of arrhythmias were observed in both WT and NOX2-Tg mice and were grouped together and labelled as AF. stim – atrial stimulation, SR – sinus rhythm.

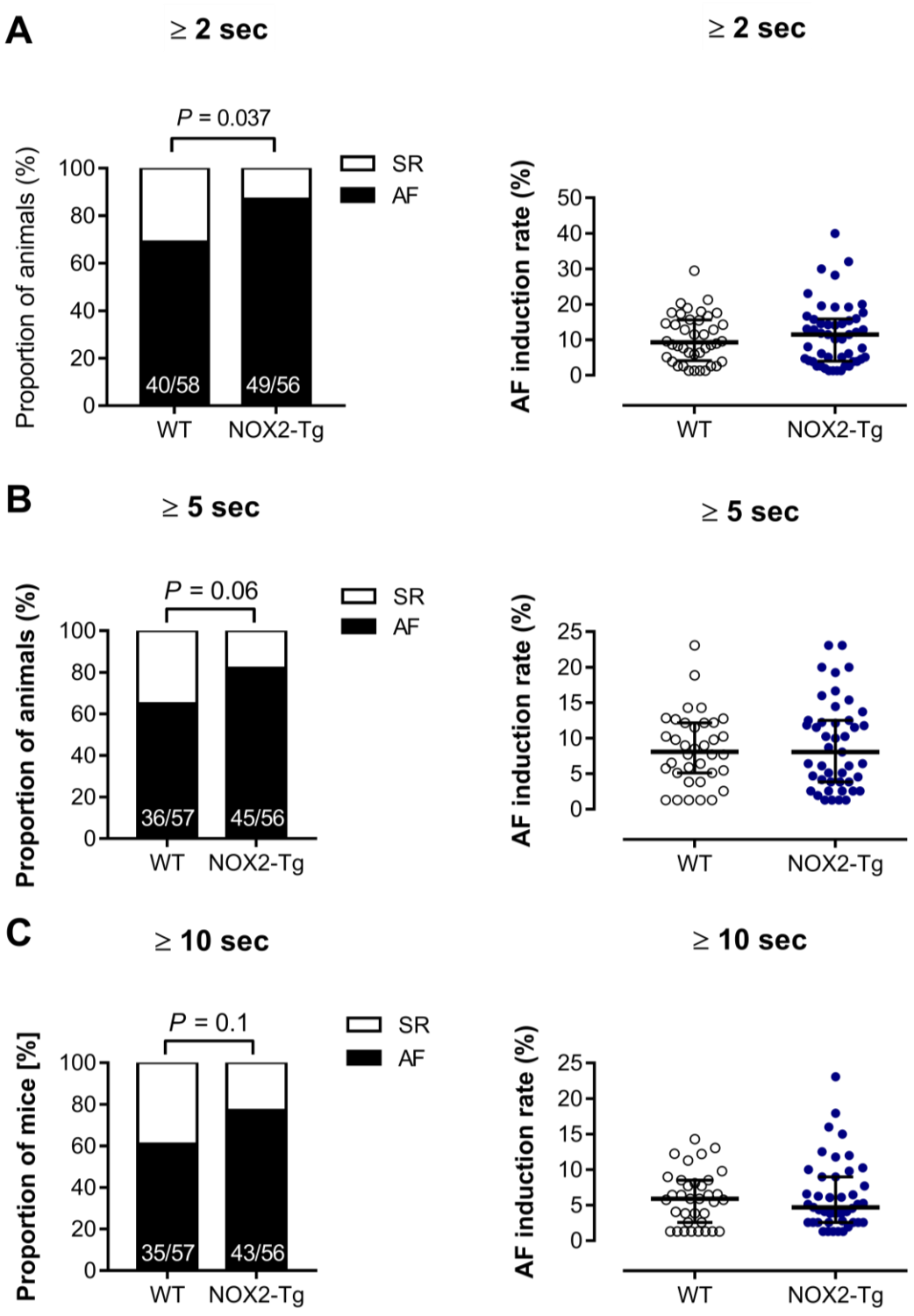

Figure 3.6: NOX2-Tg mice are more prone to pacing-induced AF. A, Percentages of NOX2-Tg and WT mice with inducible AF episodes lasting at least 2 seconds. Note higher incidence of pacing-induced AF (≥ 2 sec) in NOX2-Tg mice (*P*=0.023). The probability of AF induction (or AF induction rate) was not different between genotypes (*P*=0.83). **B,** Percentages of NOX2-Tg and WT mice with inducible AF episodes lasting at least 5 seconds and corresponding probability of AF induction are shown. **C,** Percentages of NOX2-Tg and WT mice with inducible AF episodes lasting at least 10 seconds and corresponding probability of AF induction rates are shown. Categorical data shown as percentages and *P*-values determined using Fisher's exact test. Continuous data shown as individual values with median (25^{th} to 75^{th} percentiles) and *P*-values determined using Mann-Whitney *U* test.

Next, I compared the duration of AF episodes between WT and NOX2-Tg mice. Because AF duration was found to be highly variable (*e.g.*, in one mouse, the shortest episode was <2 seconds and the longest >1800 seconds), three separate measurements were considered, including maximum AF duration (*e.g.*, the longest AF episode in each animal), cumulative AF duration (*e.g.*, cumulative sum of all discrete AF episodes in each animal), and mean AF duration (*e.g.*, average of all discrete AF episodes in each animal). The results of this analysis are summarized in Table 3.5. Maximum AF duration tended to be longer in NOX2-Tg mice (63.7 sec [25^{th} to 75^{th} percentile: 22-381 sec]) *vs* WT (47.1 sec [25^{th} to 75^{th} percentile: 25-343 sec]), but was not statistically different between groups (P=0.58). No differences in mean or cumulative AF duration (measured separately for AF episodes ≥ 2 sec and those ≥ 5 sec) were observed between genotypes.

Table 3.5: Summary of pacing-induced AF susceptibility and duration

	WT	**NOX2-Tg**	***P*-value**
Maximum duration (s)	47.1 (25 – 343)	63.7 (22.4 – 381)	0.58
AF episodes ≥ 2 sec			
Incidence (%, AF/Total)	**70% (40/57)**	**88% (49/56)**	**0.037***
Probability (%)	9.3 (4.17 – 15.6)	11.5 (4.03 – 15.9)	0.83
Duration - mean (s)	9.3 (4.17 – 15.6)	11.5 (4.03 – 15.9)	0.83
Duration - cumulative (s)	19.7 (10.2 – 55.6)	30.5 (10.3 – 66.6)	0.46
AF episodes ≥ 5 sec			
Incidence (%, AF/Total)	65% (36/57)	80% (45/56)	0.06
Probability (%)	8.4 ± 0.84	9.0 ± 0.93	0.66
Duration – mean (s)	37.1 (16.1 – 78.1)	31 (15.8 - 106)	0.79
Duration – cumulative (s)	115 (50.1 – 414)	97.7 (49.9 – 570)	0.96
AF episodes ≥ 10 sec			
Incidence (%, AF/Total)	61% (35/57)	77% (43/56)	0.1
Probability (%)	5.9 (2.56 – 8.51)	4.7 (2.56 – 8.97)	0.95
Duration – mean (s)	31.8 (18.7 – 111)	36.6 (20.1 – 253)	0.40
Duration – cumulative (s)	118 (39.2 – 411)	69 (40.2 – 584)	0.81

Comparison of AF incidence, probability, and duration between WT and NOX2-Tg mice. Data shown are mean ± SD or median (25^{th} – 75^{th} percentile). *P*-values comparing continuous data were calculated by a two-tailed unpaired Student's t-test or Mann-Whitney *U* test, as appropriate. Categorical variables were analyzed using Fisher's exact test. *P<0.05

3.4 Discussion

While a substantial number of studies have suggested an association between NOX2-derived $O_2^{\cdot -}$ and AF (Table 1.1 of Chapter 1), no direct link between enhanced NOX2 activity and atrial arrhythmia development has yet been made. In order to study the contribution of NOX2-derived $O_2^{\cdot -}$ in AF we first needed to obtain an appropriate model of enhanced NOX2 activity in the atria. Mice with cardiomyocyte-targeted NOX2 overexpression driven by the ventricular MLC-2v promoter were characterised previously and found to have approximately 5-fold higher expression of NOX2 in the LV compared with WT controls [207]; however, MLC-2v is not predicted to show transcriptional activity in the atria and the presence of the *NOX2* transgene in the atria was not reported in the study by Zhang *et al*. [207].

The present work demonstrates the expression of the *NOX2* transgene in both atrial chambers which produced relatively mild (~3-fold WT levels) overexpression of NOX2 at the protein level. Such mild overexpression of NOX2 is reminiscent of, but more marked than, increases in NOX2 expression that accompany AF in humans, *e.g.*, approximately 2-fold in the right atria of post-operative AF patients [138]. In our study, NOX2 is expressed as a protein of 58 kDa in both WT and NOX2-Tg atria, presumably representing the un-glycosylated form of the protein; NOX2 undergoes *N*-glycosylation at asparagine residues in two of the external α-helices at the N-terminal, the extent of which determines its apparent molecular weight [167, 224]. The fully-glycosylated protein has been detected at ~70-91 kDa while complete removal of carbohydrate chains produces a 55 kDa protein [167].

To show that NOX2 is overexpressed as a functional enzyme, measurement of atrial $O_2^{\cdot -}$ was essential. In the present study, the level of formation of 2-OHE from DHE was used as an indicator of intracellular $O_2^{\cdot -}$ production [212]. The level of NADPH-stimulated $O_2^{\cdot -}$ production in NOX2-Tg atria (~1.5 fold WT levels) was found to be in a relevant range to that observed in patients with post-operative and paroxysmal AF [128, 138, 143]. Collectively, these molecular

investigations demonstrate the presence of a functional NOX2 enzyme in the atrial myocardium of NOX2-Tg mice and support the use of this model to study the role of NOX2-derived $O_2^{\cdot -}$ in AF.

Having established that NOX2-Tg mice produce a greater amount of $O_2^{\cdot -}$ in the atria, the next major objective was to evaluate cardiac conduction and AF susceptibility. Surface ECG features were not different between genotypes, except for longer QT and RR intervals in NOX2-Tg mice. QT interval prolongation is likely a consequence of the slower heart rate in NOX2-Tg mice as they are known to be dynamically related (at faster heart rates the QT interval shortens while it prolongs at slower heart rates); indeed, heart rate correction abolished the differences in QT interval between groups.

The underlying cause of the mild heart rate reduction in NOX2-Tg mice is as yet unclear. Although a number of ion channels known to be involved in heart rate modulation are redox-sensitive (*e.g.* L-type Ca^{2+} channels [84], RyR2 channels [152, 153]), very few studies have looked at this directly. One report examining the role of oxidized CaMKII in sinus node dysfunction [225], demonstrated a reduction (~15%) in the resting heart rate of AngII-infused (3 mg/kg/day for 28 days) WT mice in association with increased atrial ROS production and oxidation of CaMKII that was absent in $p47^{phox}$-deficient mice, thus implying the involvement of NADPH oxidase-derived ROS (although not specifically from NOX2). On the other hand, in the study by Zhang *et al.* [207], NOX2-Tg mice did not show any difference in heart rate neither under basal conditions nor upon chronic stimulation with Ang-II (1.1 mg/kg/day for 14 days) to activate NOX2. The attribution of statistical difference to the detection of such a small difference in heart rate (~3%) in our study could be explained by the much larger sample size (approximately 60 *vs* 10 mice) and the use of surface ECG monitoring (as opposed to echocardiography, which may not allow the detection of such small differences).

In agreement with previous observations, we here show that a NOX2-mediated increase in atrial $O_2^{\cdot -}$ production increases AF vulnerability in mice. Spontaneous AF was not found in our study but could be consistently induced by atrial burst pacing. Previously, mice with cardiac overexpression of constitutively-active Rac1-GTPase, a necessary NOX2 co-factor, were found to develop AF spontaneously (up to 44% and 75% of mice aged 10 and 16 months, respectively)

[145]. However, no specific information was provided regarding the extent to which perpetuation of AF depended on NOX2-derived ROS. It is plausible that the spontaneous AF is a consequence of the profound atrial and ventricular hypertrophy, interstitial fibrosis, and LV dysfunction observed in Rac1 transgenic hearts [145, 226]. This notion is supported by the fact that inhibition of Rac1 and related NADPH oxidase activity with rosuvastatin did not affect atrial collagen content or size and only partially reduced the incidence of AF (from 44% to 20%), but did not completely eliminate the AF phenotype [145].

In our NOX2-Tg model, we did not observe any differences in AF duration which may suggest that NOX2 is involved in the generation rather than maintenance of AF. In studying the sources of ROS at different stages of AF, Reilly *et al.* [138] suggested that NOX2-dependent $O_2{\cdot}^-$ likely accounts for the early development of AF. In their goat model of pacing-induced AF, production of $O_2{\cdot}^-$ by NADPH oxidases, as well as expression of NOX2 and $p22^{phox}$, were shown to be increased after two weeks of AF but returned to baseline 6 months later. At the 6 month time-point, elevations in $O_2{\cdot}^-$ production were predominantly from mitochondria (Complex I) and uncoupled NOS. Similar observations were made in patients with AF. For instance, NOX2-mediated $O_2{\cdot}^-$ production was shown to be predictive of AF development in the post-operative period [142, 143]. In these studies, NADPH oxidase activity was measured in atrial samples obtained before cardiopulmonary bypass (*e.g.* preceding the onset of ischemia/reperfusion injury and inflammation after cardiac surgery). In the case of permanent AF, increased levels of $O_2{\cdot}^-$ production in right atrial appendages were attenuated by rotenone and L-NAME (inhibitor of NOS), but not apocynin, implicating mitochondrial sources and NOS uncoupling [138].

The apparent expression of NOX2 in the ventricles (see Figure 3-1 and ref. [207]) is a potential confounding variable as it has been associated with the development of LV hypertrophy [207, 223], a major risk factor for AF [27]. In assessing basal cardiac function, we made the unanticipated finding that LV posterior wall thickness at diastole, an indicator of LV hypertrophy, was enhanced in transgenic mice. LV mass and indexed LV mass also tended to be higher. The inconsistency in these findings with Zhang *et al.* [207], who observed higher interventricular septal thickness at diastole in Ang-II-infused NOX2-Tg mice but not in WT controls or in untreated

NOX2-Tg mice at 3 months or 12 months of age, is unclear. Nevertheless, the increase in mass was not detrimental to cardiac function as both ejection fraction and fractional shortening were preserved.

In summary, the data presented in this chapter show that NOX2 expression and related NADPH-stimulated $O_2{\cdot}^-$ production are elevated in NOX2-Tg atria and associated with an increase in the vulnerability to AF after atrial pacing, in the absence of significant alterations in left ventricular function. These findings predict that interference with, or reductions in, NOX2-mediated $O_2{\cdot}^-$ production could prove useful in preventing the new onset of AF. In Chapter 4, pharmacological inhibition of NOX2-derived $O_2{\cdot}^-$ production is studied.

4 Effect of Atorvastatin on AF Susceptibility in NOX2-Tg mice

4.1 Introduction

Statins are a class of lipid-lowering drugs that act as competitive inhibitors of HMG-CoA (3-hydroxy-3methylglutaryl-coenzyme-A) reductase, the rate-limiting enzyme within the mevalonate pathway of cholesterol biosynthesis [227]. In addition to their lipid-lowering effects, statins have been shown to exert antioxidant properties owing to their ability to inhibit the generation of isoprenoid intermediates which serve as lipid attachments for small GTPase signalling molecules, including RhoA, Cdc42, and Rac1 [228, 229]. Of note, Rac1-GTPase is a necessary activator of NOX2; upon binding of GTP, Rac1 translocates to the membrane and interacts with both flavocytochrome b558 (the heterodimeric protein comprised of NOX2 and $p22^{phox}$) and $p67^{phox}$ to initiate the one-electron reduction of molecular oxygen to $O_2^{\cdot -}$ (refer to Chapter 1 for a review of this process).

By inhibiting the geranylgeranylation and membrane translocation of Rac1 [228, 229], statins have been shown to attenuate $O_2^{\cdot -}$ production from NOX2 [138, 142, 230]. Work by Antoniades and colleagues demonstrated that it is possible to modulate both vascular [230] and myocardial [142] NOX2 activity with short-term statin therapy in patients. In the latter double-blind, placebo-controlled clinical trial evaluating the efficacy of statin therapy to improve myocardial redox balance, 42 patients were randomized to receive a 3-day treatment regimen with atorvastatin (40 mg daily) or placebo before cardiac surgery [142]. Analysis of right atrial appendage samples (collected at the time of surgery) showed a significant reduction in NADPH-stimulated and apocynin-inhibitable $O_2^{\cdot -}$ production, as well as Rac1 activity (*ex* vivo studies), in the atorvastatin-treatment group compared with placebo, implying inhibition of NOX2 activity.

It is conceivable then that statins may have potential utility in the prevention of AF with elevated NOX2 activity, as seen in patients with paroxysmal [128] and post-operative AF [138,

143]. Indeed, in mice with cardiac-specific overexpression of Rac1, rosuvastatin inhibited atrial Rac1 activity and reduced NADH-stimulated $O_2\cdot^-$ production, effects which were associated with a profound reduction (~50%) in the incidence of AF [145]. In patients, small clinical trials evaluating the efficacy of statins in the prevention of post-operative AF have shown positive results. For instance, in the ARMYDA-3 (Atorvastatin for Reduction of Myocardial Dysrhythmia After cardiac surgery) randomized clinical trial enrolling 200 patients, treatment with atorvastatin (40 mg daily administered 7 days before cardiac surgery) significantly reduced the incidence of post-operative AF (odds ratio = 0.39, 95% CI = 0.18 – 0.85) compared with placebo [231]. Furthermore, a recent meta-analysis of 13 randomized controlled trials (1216 patients undergoing cardiac surgery) showed that statins reduce the incidence of post-operative AF by approximately 50% (odds ratio = 0.39, 95% CI = 0.29 – 0.51) [232], as suggested by other meta-analyses [233-235].

However, data from the recently reported Statin Therapy in Cardiac Surgery (STICS) clinical trial, evaluating the effect of preoperative rosuvastatin (20 mg daily given up to 8 days before cardiac surgery) in 1922 patients undergoing cardiac surgery patients, showed no significant effect on the incidence of post-operative AF (odds ratio = 1.04, 95% CI = 0.84 – 1.34) in patients randomized to rosuvastatin or placebo [232]. It is worth mentioning that rosuvastatin was tested under the assumption that it can inhibit myocardial $O_2\cdot^-$ generation from NOX2 which was not reported in the STICS trial. In fact, none of the clinical trials reported thus far had included both the incidence of post-operative AF and the effectiveness of statins to inhibit NOX2-derived $O_2\cdot^-$ as study endpoints. Therefore, it remains unclear whether different statin treatment regimens (*e.g.*, different types of statins and duration of dosing period) are efficacious in inhibiting NOX2 activity and whether a reduction in NOX2 activity coincides with a reduction in post-operative AF risk in these clinical trials.

The NOX2-Tg mouse model, in which an increase in atrial NOX2 activity is accompanied by an increase in susceptibility to pacing-induced AF (Figure 3.6 and Table 3.5), is a useful tool for studying this further. Accordingly, this chapter investigates whether inhibition of NOX2-derived $O_2\cdot^-$ production by atorvastatin abolishes AF susceptibility by transesophageal pacing in NOX2-Tg mice.

4.2 Methods

The following procedures were performed in this chapter as described in detail in Chapter 2:

- 2.2 Tissue Collection and Processing
- 2.5 Measurement of $O_2^{\cdot -}$ Production
    - 2.5.1 Detection of Dihydroethidium Oxidation Products by HPLC
- 2.6 Cholesterol Assay
- 2.7 In-Vivo Interventions
    - 2.7.1 Echocardiography
    - 2.7.2 Electrophysiology
        - 2.7.2.1 Surface ECG Recordings
        - 2.7.2.2 Transesophageal Atrial Burst Pacing
        - 2.7.2.3 Data Collection and Offline Analysis
- 2.10 Statistical Analysis

Specific details relevant to this chapter are provided below.

4.2.1 Dietary Intervention

Short-term administration of atorvastatin was previously shown to inhibit the membrane translocation of Rac1 and attenuate $O_2^{\cdot -}$ production from NOX2 in atrial tissue samples from patients undergoing cardiac surgery [142]. In this study, atorvastatin, 30 mg/kg/day, *p.o.*, was used to inhibit NOX2-derived $O_2^{\cdot -}$ release. Tablets were ground into a fine powder, mixed with powder rodent chow ingredients and compressed into food pellets. Based on a daily food intake of approximately 3 g chow/mouse, 250 mg atorvastatin was prepared per kilogram of chow. WT and NOX2-Tg mice received either atorvastatin or placebo (*e.g.* diet prepared in the same way but without the active drug) at 14-18 weeks old and were maintained on the diet for a total period of 14 days. Food consumption and body weight were monitored throughout the dosing period.

4.2.2 Statistical Analysis

Statistical significance of differences was assessed by two-way ANOVA with the following factors: genotype, diet (placebo *vs* atorvastatin) and interaction between diet and genotype. Two-way ANOVA was followed by Tukey's multiple comparison *post-hoc* test with adjusted *P*-values. Non-parametric data were either log-transformed or square root-transformed to obtain normality. The null hypothesis was rejected at a value of $P < 0.05$.

4.3 Results

4.3.1 Effect of atorvastatin on food intake, body weight and cholesterol profile

Body weight and food consumption in all experimental groups are shown in Table 4.1. Incorporation of atorvastatin (30 mg/kg/day) into the rodent chow did not affect food consumption of WT and NOX2-Tg mice compared with the placebo diet. Likewise, body weight in all four experimental groups was maintained over the whole treatment period. To determine whether the effects of atorvastatin are independent of cholesterol lowering, we measured free cholesterol content in LV tissue lysates and plasma samples. Atorvastatin had no significant influence (P>0.05, two-way ANOVA with Tukey *post-hoc* analysis) on myocardial and plasma concentrations of free cholesterol in either WT or NOX2-Tg mice compared with placebo diet (Figure 4.1).

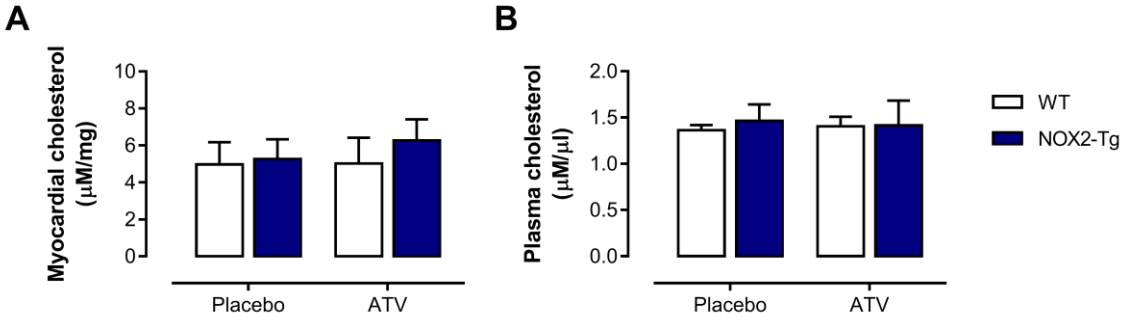

Figure 4.1: Effect of atorvastatin on myocardial and plasma cholesterol content. A, There was no significant difference in the left ventricular free cholesterol content between WT and NOX2-Tg mice who received atorvastatin (WT: n=7, 5.01 ± 1.4 μM/mg; NOX2-Tg: n=9, 6.27 ± 1.1 μM/mg) and those who received placebo (WT: n=7, 4.97 ± 1.2 μM/mg; NOX2-Tg: n=5, 5.26 ± 1.1 μM/mg). **B,** Free cholesterol content in plasma samples was not affected by atorvastatin treatment (WT: n=8, 1.41 ± 0.1 μM/μl; NOX2-Tg: n=4, 1.42 ± 0.27 μM/μl) compared with placebo (WT: n=7, 1.36 ± 0.06 μM/μl; NOX2-Tg: n=4, 1.47 ± 0.18). *P*-values were calculated by two-way ANOVA with Tukey *post-hoc* analysis. Data shown are mean ± SD. ATV – atorvastatin.

Table 4.1: Body weight and food consumption of WT and NOX2-Tg mice

	PLACEBO		ATORVASTATIN	
	WT	**NOX2-Tg**	**WT**	**NOX2-Tg**
Food Intake (g/day/mouse)	3.52 (2.85 – 3.98)	3.33 (2.77 – 4.0)	2.90 (2.31 – 3.65)	2.90 (2.41 – 3.65)
Body weight (g)				
Day 1	27.0 ± 4.38	27.1 ± 4.58	27.9 ± 5.17	26.7 ± 4.81
Day 3	27.2 ± 4.13	27.0 ± 4.19	26.8 ± 5.03	26.5 ± 4.49
Day 6	28.0 ± 4.13	27.0 ± 4.08	26.3 ± 5.12	26.4 ± 4.77
Day 8	28.7 ± 4.13	26.4 ± 5.21	26.5 ± 4.61	27.1 ± 4.45
Day 10	26.3 ± 4.56	27.3 ± 4.16	25.8 ± 4.60	24.8 ± 2.93
Day 14	27.1 ± 4.17	26.6 ± 4.73	25.6 ± 4.65	25.3 ± 4.05

Comparison of food consumption and body weight between placebo and atorvastatin-treated NOX2-Tg mice and WT littermates. Data shown are mean ± SD or median (25^{th} to 75^{th} percentile). *P*-values were calculated by two-way ANOVA with Tukey *post-hoc* analysis. Non-parametric data were square-root transformed before statistical analysis.

4.3.2 Effect of atorvastatin on atrial $O_2^{\cdot -}$ production

Statins attenuate $O_2^{\cdot -}$ production from NADPH oxidases by inhibiting the production of mevalonate that is required for the isoprenylation of Rac1-GTPases to the plasma membrane [138, 142, 230]. The effect of atorvastatin on atrial $O_2^{\cdot -}$ production in WT and NOX2-Tg mice was assessed by HPLC-based detection of 2-OHE using NADPH as a substrate for NOX2 enzyme activity and tiron to ensure specificity for $O_2^{\cdot -}$, as described in Section 2.5.1 of Chapter 2. Representative HPLC chromatograms of $O_2^{\cdot -}$ production (2-OHE peak) in LA homogenates of placebo and atorvastatin-treated mice are shown in Figure 4.2-A. Consistent with the data reported in Chapter 3 (Figure 3.3), NADPH-stimulated $O_2^{\cdot -}$ production was significantly higher in placebo-treated NOX2-Tg RA (P=0.0029 *vs* WT, two-way ANOVA with Tukey multiple comparison test, Figure 4.2-B) and LA homogenates (P=0.006 *vs* WT, two-way ANOVA with Tukey multiple comparison test, Figure 4.2-C).

Importantly, dietary administration of atorvastatin prevented the NADPH-stimulated increase in $O_2^{\cdot -}$ production in NOX2-Tg atria. Figure 4.2-B demonstrates that NADPH-stimulated $O_2^{\cdot -}$ production in RA homogenates from atorvastatin-fed NOX2-Tg mice was significantly lower when compared with placebo-fed NOX2-Tg mice (P=0.04, two-way ANOVA with Tukey multiple comparison), with no differences between atorvastatin-fed WT and NOX2-Tg mice (P>0.05). Similarly, $O_2^{\cdot -}$ production in LA homogenates was significantly lower in atorvastatin-fed NOX2-Tg mice (P=0.014 *vs* placebo-fed NOX2-Tg, two-way ANOVA with multiple comparison test), with no differences between atorvastatin-fed groups (P>0.05, Figure 4.2-C).

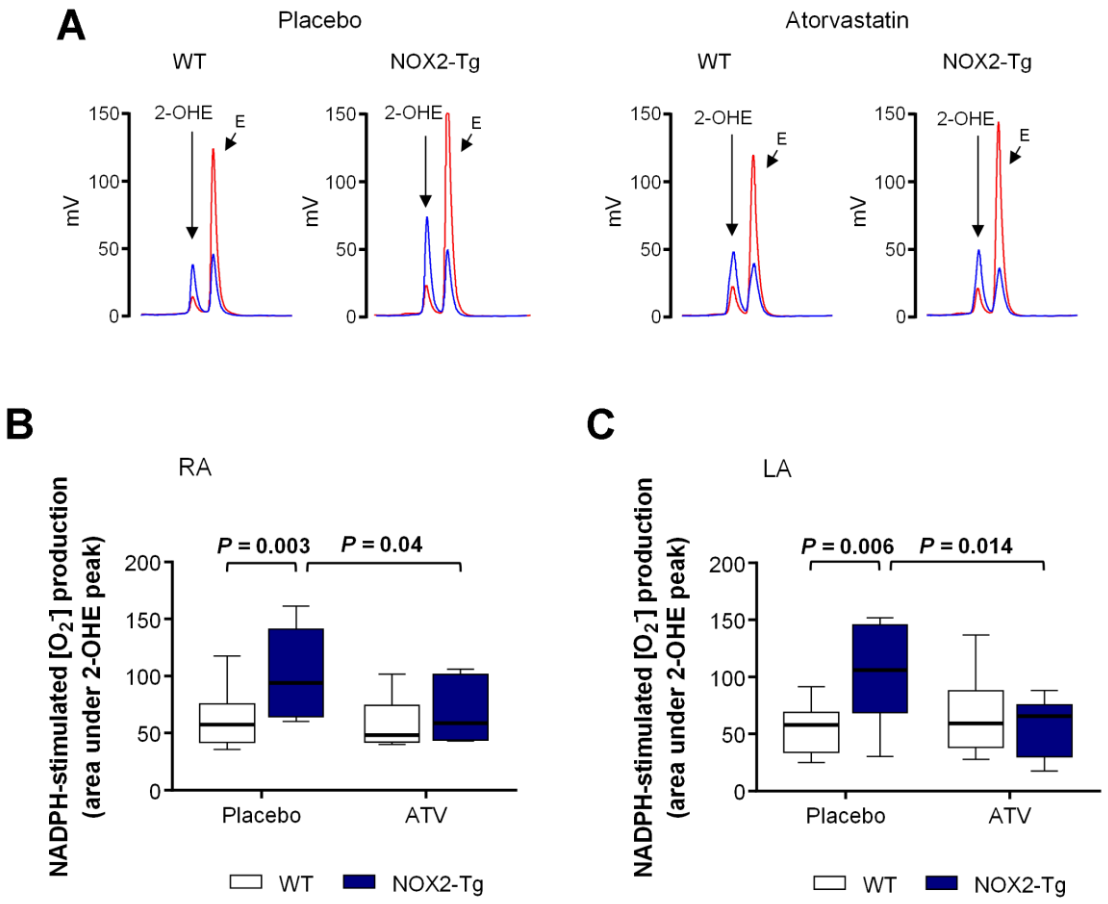

Figure 4.2: Atorvastatin prevents the increase in NADPH-stimulated atrial $O_2^{\cdot-}$ production secondary to NOX2 overexpression. **A,** HPLC chromatograms of $O_2^{\cdot-}$ production (2-OHE peak) in LA homogenates from WT and NOX2-Tg mice given atorvastatin or placebo diet are shown. — NADPH, — Tiron. **B,** NADPH-stimulated $O_2^{\cdot-}$ production is higher in RA homogenates of placebo-treated NOX2-Tg mice (*P*=0.003 *vs* WT-placebo; n=16 for WT, n=11 for NOX2-Tg). This difference is abolished by atorvastatin treatment (*P*=0.9). **C,** The increase in NADPH-stimulated $O_2^{\cdot-}$ production in LA homogenates of placebo-treated NOX2-Tg mice (n=8) compared with WT controls (n=11, *P*=0.006) is prevented by atorvastatin treatment, with no differences between atorvastatin-treated groups (WT, n=12; NOX2-Tg, n=9; *P*=0.84). Data shown as box and whisker plots: maximum and minimum. Two-way ANOVA with Tukey *post-hoc* analysis was used to determine statistical significance of placebo and $O_2^{\cdot-}$ production with atorvastatin between groups. 2-OHE – 2-hydroxyethidium, E – ethidium, ATV – atorvastatin, AUC – area under curve.

4.3.3 Effect of atorvastatin on cardiac function and electrical conduction

To assess the effect of atorvastatin administration on cardiac function and morphology, 2-D M-mode echocardiography was performed. No significant differences in systolic or diastolic measurements were detected between placebo-fed WT and NOX2-Tg mice and there was no significant effect of atorvastatin compared with placebo diet, as summarized in Table 4.2. Consistent with the data reported in Chapter 3, we here show a similar increase in end-diastolic posterior wall thickness of placebo-fed NOX2-Tg hearts *vs* WT littermates (WT: 0.84 ± 0.06 mm, n=6; and NOX2-Tg: 0.92 ± 0.19 mm, n= 6), but the differences were not statistically significant between groups in this smaller cohort. LV mass showed a similar upward trend in placebo-fed NOX2-Tg mice (94.5 ± 24.1 mg *vs* 80.9 ± 20.7 mg for placebo-fed WT). Analysis of surface ECG parameters revealed significantly longer QT intervals in placebo-fed NOX2-Tg mice (P=0.035 *vs* WT-placebo; Table 4.3), as observed previously (Figure 3.4 and Table 3.3). This difference did not persist when QT was corrected for heart rate (QTc). No other differences in ECG parameters were statistically significant between genotypes and there was no effect of atorvastatin administration.

Table 4.2: Left ventricular structure and function assessed by echocardiography

	PLACEBO		ATORVASTATIN	
	WT	**NOX2-Tg**	**WT**	**NOX2-Tg**
N	6	6	5	7
Heart rate				
Baseline HR (bpm)	469 ± 23	472 ± 15	467 ± 36	487 ± 14
HR for diastolic measurements	350 ± 44	372 ± 22	334 ± 44	354 ± 29
LV dimensions				
LV diastolic posterior wall (mm)	0.84 ± 0.06	0.92 ± 0.19	0.89 ± 0.12	0.89 ± 0.17
LV systolic posterior wall (mm)	1.36 ± 0.20	1.33 ± 0.15	1.33 ± 0.24	1.38 ± 0.24
LV diastolic internal diameter (mm)	3.41 ± 0.39	3.61 ± 0.23	3.51 ± 0.52	3.69 ± 0.55
LV systolic internal diameter (mm)	2.0 ± 0.45	2.2 ± 0.27	2.15 ± 0.43	2.27 ± 0.57
Indexed LV diastolic volume (µL/g)	2.24 ± 0.44	2.33 ± 0.76	2.37 ± 0.43	2.75 ± 0.76
Indexed LV systolic volume (µL/g)	0.62 ± 0.29	0.72 ± 0.34	0.73 ± 0.27	0.88 ± 0.54
LV mass				
LV mass (mg)	80.9 ± 20.7	94.5 ± 24.1	92.4 ± 43.6	95.3 ± 30.6
Indexed LV mass (mg/g)	3.78 ± 0.90	3.86 ± 1.06	4.13 ± 1.16	4.35 ± 0.70
LV systolic function				
LV ejection fraction (EF, %)	73.1 ± 9.72	70.3 ± 5.52	69.9 ± 6.71	69.6 ± 9.91
Fractional shortening (FS, %)	42.0 ± 9.12	39.2 ± 4.7	38.8 ± 5.71	39.2 ± 7.25
LV diastolic function				
Mitral valve E/A ratio	1.82 ± 0.17	1.75 ± 0.20	1.92 ± 0.58	1.89 ± 0.38
Tissue doppler E'/A' ratio	1.38 ± 0.19	1.34 ± 0.08	1.36 ± 0.26	1.29 ± 0.35
Combined E/E' ratio	28.9 ± 7.43	27.8 ± 5.03	34.6 ± 1.37	36.5 ± 12.2

Echocardiographic measurements evaluating left ventricular mass, and systolic and diastolic function of placebo and atorvastatin-treated WT and NOX2-Tg mice. Data shown are mean ± SD. Data were analysed by two-way ANOVA with Tukey multiple comparison test. N – number of animals; E – early mitral valve inflow velocity (passive filling); A – late mitral valve inflow velocity (active filling); E' – early tissue Doppler mitral valve annulus velocity; A' – late tissue Doppler mitral valve annulus velocity; IVCT – isovolumetric contraction time; IVRT – isovolumetric relaxation time.

Table 4.3: Standard electrophysiology parameters

	PLACEBO		ATORVASTATIN	
	WT	**NOX2-Tg**	**WT**	**NOX2-Tg**
n	*29*	*30*	*32*	*33*
Male (%)	16 (55)	17 (57)	16 (50)	14 (42)
RR, ms	130 ± 19	138 ± 18	134 ± 19	135 ± 18
P wave, ms	22.6 ± 1.66	22.4 ± 2.13	22.5 ± 1.42	22.2 ± 2.0
PQ, ms	41.5 ± 3.13	40.9 ± 4.61	42.1 ± 3.83	40.9 ± 3.0
QRS, ms	8.09 ± 0.80	7.58 ± 0.87	7.89 ± 0.87	7.58 ± 0.79
QT, ms	**58.2 ± 6.92**	**63.4 ± 7.21***	57.4 ± 7.46	60.7 ± 7.30
QTc, ms	51.0 ± 4.21	54.0 ± 4.79	49.6 ± 5.28	52.4 ± 4.93

Comparison of surface ECG parameters obtained from placebo and atorvastatin-treated WT and NOX2-Tg mice. Data shown are mean ± SD or median (25^{th} to 75^{th} percentile). P-values were calculated by two-way ANOVA with Tukey multiple comparison test. Non-parametric data were log- or square root-transformed before statistical analysis, as appropriate. N – number of mice, RR – R-R interval denoting the cardiac cycle duration, P wave – duration of the atrial depolarization and repolarization, PQ – interval from the start of the P wave to the start of the QRS complex, QRS – ventricular depolarisation time, QT – duration of ventricular depolarisation and repolarisation, QTc – QT interval corrected for heart rate. *P=0.035 compared with WT, placebo.

4.3.4 Effect of atorvastatin on susceptibility to pacing-induced AF

In the previous chapter, we reported that NOX2-Tg mice are more susceptible to pacing-induced AF, particularly when assessing atrial arrhythmias longer than 2 seconds in duration. To examine the effect of inhibiting NOX2 on this phenotype, mice were allocated to treatment with or without atorvastatin for 2 weeks and AF susceptibility was interrogated by trans-esophageal atrial burst pacing. As documented in Figure 4.3-A, electrical stimulations delivered to the atria provoked AF (with episodes lasting ≥ 2 sec) in 25/27 (93%) NOX2-Tg mice compared with 19/25 (76%) WT littermates receiving placebo (P=0.13, Fisher's exact test). In the atorvastatin treatment group, 22/27 (81%) WT mice and 27/32 (84%) NOX2-Tg mice were sensitive to developing pacing-induced AF. Among those animals with inducible AF (19 WT and 25 NOX2-Tg mice receiving placebo; 22 WT and 27 NOX2-Tg receiving atorvastatin), the probability of AF induction was quantified and found to be similar between all four groups (Figure 4.3-B).

As observed in Chapter 3, cumulative AF duration was not significantly different between WT and NOX2-Tg mice; however, two-way ANOVA showed a significant effect of atorvastatin administration (P=0.0378, F=4.45, Figure 4.3-D). We also observed a trend towards longer maximum AF duration in NOX2-Tg mice (117 sec [25^{th} to 75^{th} percentile: 40.4–381 sec]) compared with WT littermates (67.5 sec [25^{th} to 75^{th} percentile: 31.7–433 sec]) in the placebo group (Table 4.4). Both WT and NOX2-Tg mice receiving atorvastatin had shorter maximum AF durations (WT: 43.2 sec [25^{th} to 75^{th} percentile: 25.4-242 sec]; and NOX2-Tg: 64.6 sec [25^{th} to 75^{th} percentile: 22.3–261 sec]; Figure 4.3-C and Table 4.4) compared with respective placebo-fed controls, although the differences were not statistically significant. Similar results were obtained for AF incidence, probability, and duration when analyzing AF episodes longer than 5 seconds in duration, as summarized in Table 4.4.

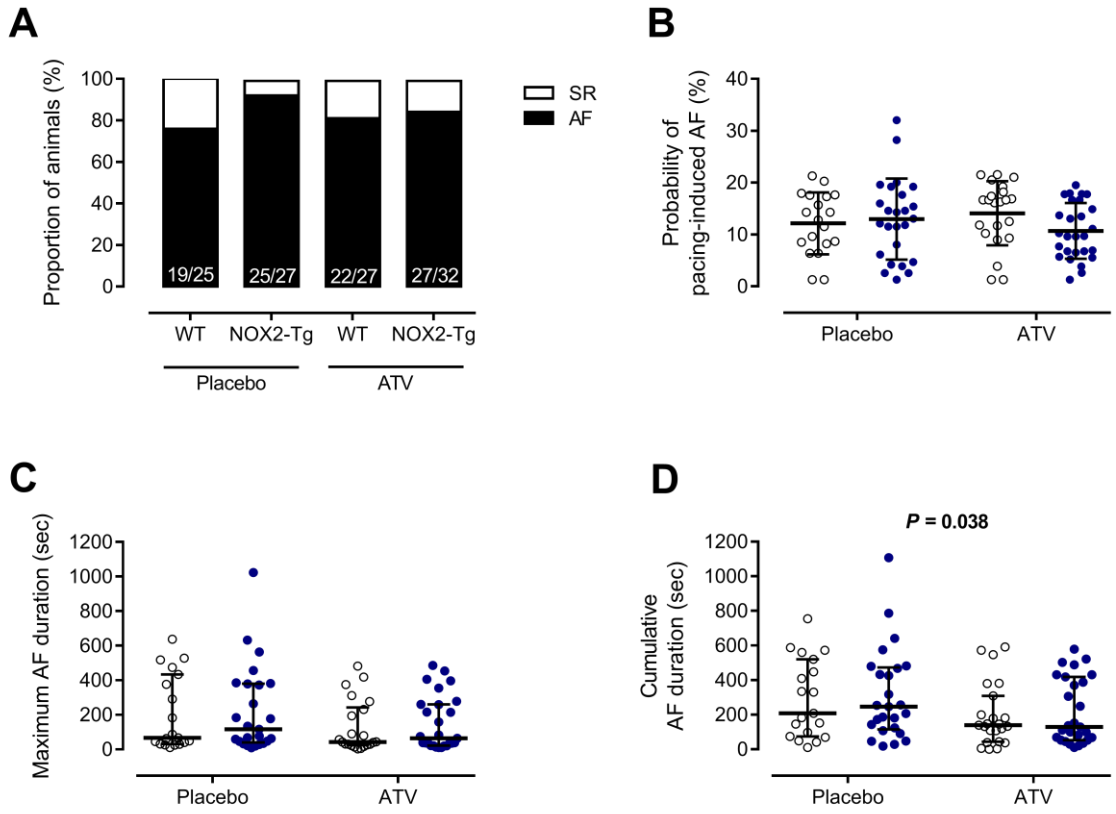

Figure 4.3: Pacing-induced AF susceptibility in placebo and atorvastatin-treated WT and NOX2-Tg mice. A, Percentages of NOX2-Tg and WT mice with inducible AF episodes lasting at least 2 seconds. **B,** The probability of AF (≥ 2 s) induction per mouse was not different between genotypes (P = 0.83) and there was no effect of atorvastatin (P=0.89). **C,** Maximum AF durations tended to be longer in placebo-fed NOX2-Tg mice (117 sec, 25th to 75th percentile: 40-381 *vs* 68 sec, 25th to 75th percentile: 32-433 sec for placebo-fed WT) and shorter with atorvastatin treatment (P=0.07; WT, 43 sec, 25th to 75th percentile: 25-242 sec *vs* NOX2-Tg, 65 sec, 25th to 75th percentile: 22-261 sec). **D,** Cumulative AF duration was significantly lower in mice who received atorvastatin (P=0.038 *vs* placebo), independent of genotype. Categorical data shown as percentages and P-values were calculated using Fisher's exact test. Continuous data shown as individual values with mean ± SD or median (25th to 75th percentile) and P-values were calculated by two-way ANOVA with Tukey multiple comparison test. Non-parametric data were log-transformed before statistical analysis. ATV – atorvastatin; SR – sinus rhythm

Table 4.4: Summary of pacing-induced AF susceptibility and duration in placebo and atorvastatin-treated mice

	PLACEBO		ATORVASTATIN	
	WT	**NOX2-Tg**	**WT**	**NOX2-Tg**
Maximum duration (s)	67.5 (31.7 – 433)	117 (40.4 – 381)	43.2 (25.4 – 242)	64.6 (22.3 – 261)
AF episodes ≥ 2s				
Incidence (%, AF/Total)	76% (19/25)	93% (25/27)	81% (22/27)	84% (27/32)
Probability (%)	12.2 ± 6.0	13.0 ± 7.83	14.1 ± 6.18	10.7 ± 5.37
Duration – mean (s)	25.5 (10.9 – 62.3)	31 (16.6 – 78.3)	14 (10.3 – 45)	18.5 (10.9 – 68.8)
Duration – cumulative (s)	208 (74 – 520)	246 (116 – 474)	**139 (44 – 309) ***	**129 (53 – 418) ***
AF episodes ≥ 5s				
Incidence (%, AF/Total)	76% (19/25)	93% (25/27)	78% (21/27)	84% (27/32)
Probability (%)	8.58 ± 4.85	10.7 ± 5.92	10.3 ± 4.34	7.34 ± 4.03
Duration – mean (s)	49.6 (29.7 – 103)	31 (17.4 – 96.4)	19.9 (12.9 – 57.8)	24.8 (16.5 – 96.4)
Duration – cumulative (s)	201 (83.8 – 508)	207 (103 – 446)	110 (77.4 – 340)	124 (49.7 – 411)

Comparison of AF incidence, probability, and duration between placebo and atorvastatin-treated WT and NOX2-Tg mice. Data shown are mean ± SD or median (25^{th} to 75^{th} percentile). P-values comparing continuous data were calculated with two-way ANOVA and Tukey multiple comparison test. Categorical variables were analyzed with Fisher's exact test. *P=0.038 *vs* placebo

4.4 Discussion

To more directly assess the involvement of NOX2 in AF, pharmacological inhibition of NOX2-derived $O_2^{\cdot -}$ production was investigated. For this study, atorvastatin was chosen based on previous studies demonstrating inhibition of NOX2 activity in atrial tissues. For example, *ex vivo* incubation of right atrial samples from post-operative AF patients with atorvastatin (20 μmol/L) for 1 hour caused a mevalonate-reversible reduction in NADPH-stimulated $O_2^{\cdot -}$ production that was associated with a significant decrease in Rac1 activity (evidenced by a decrease in the ratio of GTP-bound to total Rac1) [138] and in the membrane translocation of $p47^{phox}$ and $p67^{phox}$ [138]. Furthermore, a randomized, double-blind, placebo controlled study of 42 patients undergoing cardiac surgery demonstrated a significant reduction in atrial NADPH-stimulated $O_2^{\cdot -}$ production in patients who were randomized to receive atorvastatin (40 mg/day) for 3 days before cardiac surgery compared with patients receiving placebo [142].

In keeping with these findings, our results show a significant reduction in NADPH-stimulated $O_2^{\cdot -}$ production in left and right atrial homogenates from atorvastatin-treated NOX2-Tg mice compared with placebo controls. To determine whether this action was independent of cholesterol-lowering, we measured plasma and myocardial free cholesterol in our mice and found no significant differences between animals receiving atorvastatin when compared with placebo. These results are consistent with previous reports demonstrating that oral atorvastatin reduces NADPH-stimulated $O_2^{\cdot -}$ production independently of changes in low-density lipoprotein (LDL) cholesterol in human saphenous vein grafts [230].

We were therefore surprised not to observe a significant effect of atorvastatin on the incidence of pacing-induced AF in our NOX2-Tg mice. It is worth mentioning that statins have also been shown to inhibit $O_2^{\cdot -}$ production by enhancing the activity of endogenous antioxidant enzymes, including catalase and glutathione peroxidase [236], as well as increasing nitric oxide bioavailability [237, 238], which may explain our *in vivo* pacing data. However, as shown in Figure 4.2, atorvastatin did not have any effect on atrial NADPH-stimulated $O_2^{\cdot -}$ in WT mice,

suggesting that the reduction in $O_2^{\cdot -}$ production in atorvastatin-treated NOX2-Tg atria is unlikely to be due to antagonism of other oxidant pathways. Nevertheless, it would be useful to repeat these studies using a different inhibitor of NOX2 activity, such as gp91ds-tat peptide (thought to be specific for NOX2).

Another plausible explanation for the apparent lack of effect of atorvastatin on AF susceptibility is that we were underpowered to detect a significant reduction in AF incidence as the initial sample size calculation was based on detecting large group differences (~2-fold) in AF probability. In fact, in this smaller study (25-32 mice/group) we did not even detect a statistical difference in AF incidence between placebo-fed WT and NOX2-Tg mice despite having a similar group difference (~17% difference in AF incidence between WT and NOX2-Tg mice) as the study in Chapter 3 which had a much larger sample size (~60 mice/group). Our observed effect size in this cohort was 0.398; assuming 80% power, we would need 40 mice in each group to detect the 17% group difference reported here. Perhaps with a larger sample size and greater statistical power we may observe a significant reduction in AF incidence with atorvastatin.

Nevertheless, atorvastatin treatment was shown to have a significant effect on AF duration after analysis with two-way ANOVA. We observed a significant reduction in the cumulative duration of AF (with an AF cut-off of ≥ 2 sec), as well as a trend towards lower maximum AF durations, in atorvastatin-treated mice compared with placebo controls. The observation that cumulative AF duration was decreased to a similar extent in both WT and NOX2-Tg mice suggests an anti-arrhythmic effect of statins that is independent of NOX2 inhibition, and which may occur via effects on the atrial refractory period. Experimental animal studies have previously shown that atrial electrical remodelling, characterized by a reduction of the atrial refractory period (reviewed in refs. [4, 239]), is significantly attenuated by statins. In a canine model of pacing-induced AF, oral administration of simvastatin (80 mg daily) beginning 3 days before the onset of atrial tachypacing significantly reduced the duration of AF episodes and the shortening of the atrial refractory period [211]. This is likely attributed to enhanced I_{CaL}, as simvastatin also attenuated the tachypacing-induced downregulation of the L-type Ca^{2+} channel α-subunit at the protein level, which is associated with the electrophysiological impairment underlying AF promotion (see

Chapter 1 and refs. [4] and [239]). Similar findings were reported in a canine sterile pericarditis model, where longer atrial refractory periods, shorter intra-atrial conduction times (*e.g.*, faster conduction), and shorter AF durations were observed in the atorvastatin treatment group compared with controls [240]. Here, the effects of atorvastatin were linked to reductions in C-reactive protein (CRP) and regression of myocardial inflammation and fibrosis, which is consistent with the anti-inflammatory effects of statins [241].

5 Optical Imaging of Atrial Repolarization and Conduction

5.1 Introduction

AF occurs when electrical and/or structural abnormalities of the atria alter tissue properties to promote abnormal impulse formation and/or propagation (reviewed in ref. [4] and Chapter 1). The hallmark feature of electrical remodelling in AF is a shortening of the atrial refractory period (synonymous with the APD) that facilitates the progression of paroxysmal to persistent AF in both experimental animal models [72] and patients with AF [73-75]. The abbreviation of the atrial APD has been attributed primarily to reductions in the density of I_{CaL} [39, 76] and I_{to} [86, 87] caused by down-regulation of the underlying subunits, Cav1.2 [77, 80] and Kv4.3 [86], respectively, although alterations in I_{Na} and the repolarizing K^+ currents, I_{K1} and I_{Kur}, have also been reported in atrial myocytes from patients with AF [85, 87]. Key pathophysiological features of structural remodelling include interstitial fibrosis, inflammation, myocyte hypertrophy and apoptosis, and alterations in gap junction organization [92, 106]. Mechanistically, these changes impede impulse propagation through the atrial tissue by disrupting the normal ordered pathways for cell-to-cell conduction, and hence provoke inhomogeneity of electrical conduction and decrease conduction velocity (both of which favour re-entrant circuits) [4].

To explore the underlying arrhythmogenic substrate in NOX2-Tg mice, we interrogated for changes in atrial APD and wave propagation, information which can then be used to make predictions about the cellular and molecular mechanisms driving atrial arrhythmogenesis in response to NOX2 overexpression (*e.g.*, whether electrical and/or structural remodelling had occurred). Optical imaging (or mapping) using fluorescent, voltage-sensitive dyes offers a high-resolution method to study the electrophysiology of cardiac tissues or multi-cellular preparations (as opposed to single cells) [242] and has been widely used to map the spread of electrical wave

propagation in both atrial and ventricular arrhythmias in isolated animal hearts as well as human cardiac tissue preparations (reviewed in ref. [243]). The aim of this chapter was to establish a method for optical imaging of isolated atrial tissues and to use this technique to compare atrial repolarization and conduction between WT and NOX2-Tg mice.

5.2 Methods

5.2.1 Optical Imaging of Isolated Atrial Preparations

As part of my DPhil, I developed a protocol for optical imaging to measure transmembrane potentials and wavefront conduction patterns in isolated atrial tissues. This section describes the atrial tissue preparation, the individual components of the optical imaging system, the acquisition of optical action potentials, as well as methods developed to analyse the acquired data.

5.2.1.1 Optical Imaging System

Optical mapping studies are based on the principle that voltage-sensitive dyes alter their fluorescence spectra in response to changes in the membrane potential [244]. 4-(2-(6-(dibutylamino)-2-napthalenyl)-ethenyl)-1-(3-sulfopropyl)-pyridinium (di-4-ANEPPS) is a commonly used potentiometric dye, developed by the Loew laboratory [244], with absorption and fluorescence emission maxima at around 485 nm and 685 nm, respectively. The dye binds with high affinity to the plasma membrane of cells (due to the presence of a polar group and two hydrocarbon chains at opposite sides of the chromophore [244]) and undergoes a shift in its peak emission spectrum towards shorter wavelengths upon depolarization, such that a decrease in fluorescence is observed that is inversely proportional to changes in the transmembrane potential.

To excite the dye, illuminating light (545 nm) from an LED source (MacroLED, Cairn Research Labs) is passed through a selection filter and reflected off a dichroic mirror (565 nm, Chroma Technology) onto the tissue preparation. For imaging transmembrane voltage kinetics, the emitted fluorescent light is passed through a band-pass filter (545/25 nm, Chroma Technology) and captured using a high-speed complementary metal-oxide semiconductor (CMOS) camera (NeuroCMOS-DW128-II, Cairn Research Labs) with high spatial (128 by 128 pixels) and temporal (10,000 frames per sec) resolution. The camera is mounted onto an Olympus MVX10 Macro-view fluorescent microscope equipped with a 1x or 2x MV PLAPO objective (Olympus). A photograph depicting the components of the optical imaging hardware setup is provided in Figure 5.1.

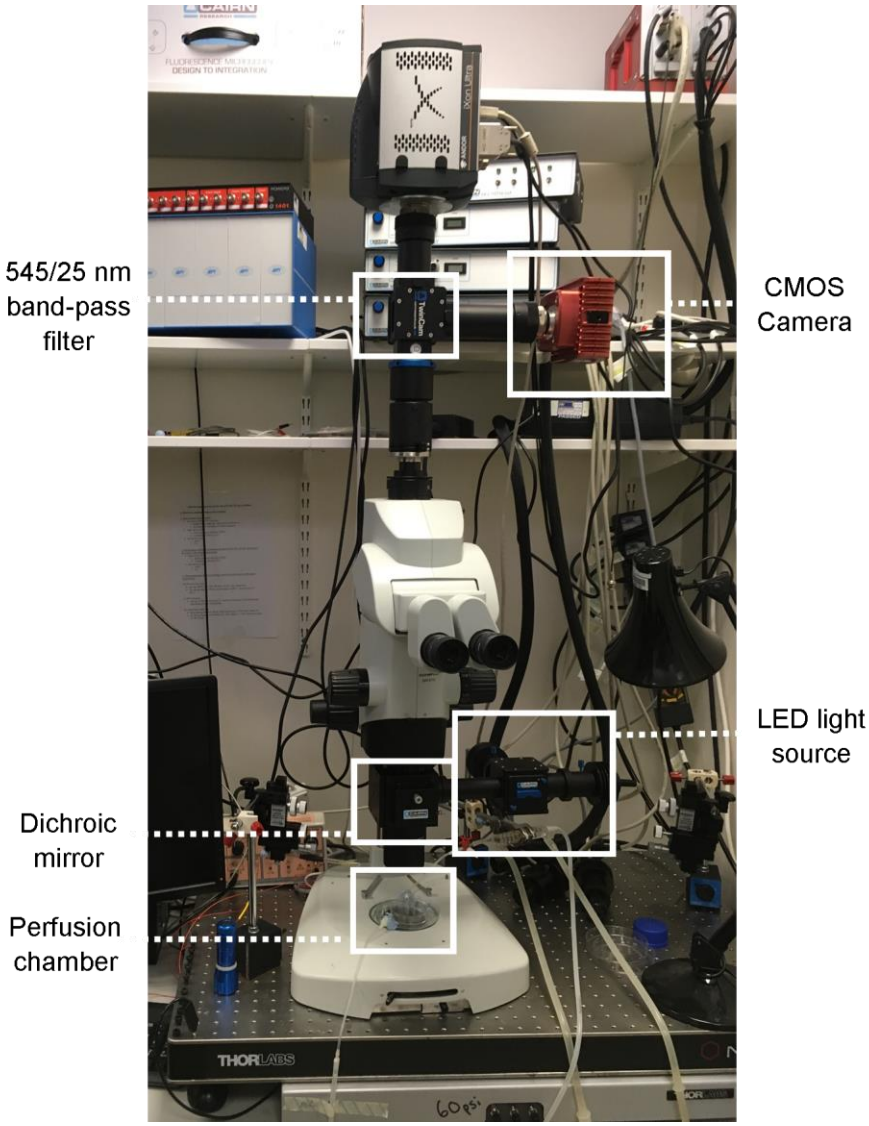

Figure 5.1: Photograph depicting the components of the optical imaging system. Di-4-ANEPPS-stained atrial preparations are placed in the perfusion chamber and illuminated by an LED light source at 545 nm. The emitted light passes through a band-pass filter (545/25 nm) and captured using a high-speed CMOS camera that is mounted onto an Olympus MVX10 Macro-view fluorescent microscope equipped with a 1x or 2x MV PLAPO objective (Olympus). All imaging data was collected using the GView optical mapping software.

5.2.1.2 Atrial Tissue Preparation and Data Acquisition

Mice were heparinized (1000 U/mL, *i.p.*) to prevent blood clotting and sacrificed by cervical dislocation. After mid-sternal incision, the heart was immediately excised and placed into Tyrode solution (37°C) consisting of (in mmol/L): 130 NaCl, 5.6 KCl, 3.5 $MgCl_2$, 5.0 HEPES, 0.4 Na_2HPO_4, 10 glucose, 20 taurine, and 1.4 $CaCl_2$. The heart was then pinned to the bottom of a clear Sylgard-coated petri dish and the lungs, thymus, and any other residual tissue were removed from the heart. An incision was made along the atrioventricular connective tissue and the ventricles were carefully separated from the atria, leaving a preparation consisting of the interconnected left and right atrial chambers. The superior and inferior vena cavae were cut open and the atrial tissue was stretched and pinned to the bottom of a 30 mm superfusion chamber so that the crista terminalis and interatrial septum were visible. A photograph of a typical atrial preparation is shown below in **Figure 5.2**.

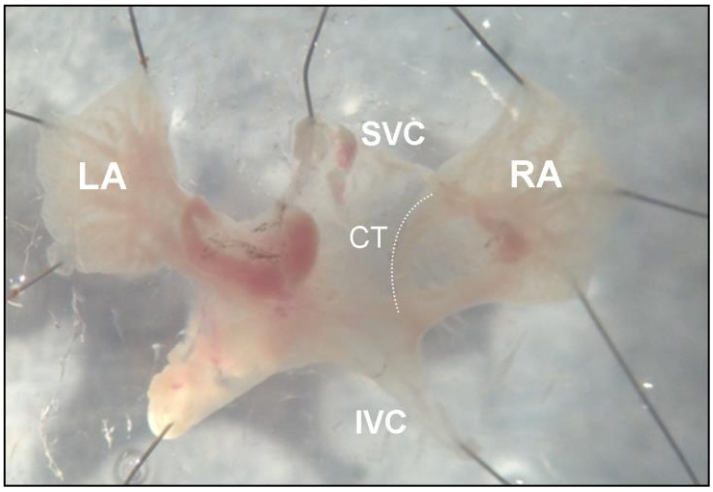

Figure 5.2: Photograph of an isolated murine atrial preparation. Atria were separated from the ventricles by cutting along the atrioventricular connective tissue. An incision was made along the superior vena cava and the atria were stretched and pinned so that the crista terminalis could be identified. The atria were then incubated with di-4-ANEPPS for optical imaging of transmembrane voltage kinetics. Anatomical features are annotated in white. LA – left atria, RA – right atria, SVC – superior vena cava, IVC – inferior vena cava, CT – crista terminalis.

Following isolation, atrial preparations were incubated in Tyrode solution containing di-4-ANEPPS (20 µmol/L) and blebbistatin (5 µmol/L) for 30 min at 37°C. Blebbistatin was used to immobilize the tissue and prevent motion artefacts in the acquired data. The Tyrode solution was then removed and the atria were continuously perfused with Krebs-Henseleit solution of the following composition (in mmol/L): 118 NaCl, 4.2 KCl, 1.2 KH_2PO_4, 1.2 $MgSO_4$, 11 $NaHCO_3$, 11 glucose, 2 Na-pyruvate, and 1.5 $CaCl_2$, and supplemented with 1 µmol/L blebbistatin. The solution was continuously bubbled with a 95% O_2-5% CO_2 mixture and the temperature was monitored and held at 35-37°C using a thermal immersion circulator and a glass water jacket placed immediately before the inflow of the solution. Both the inflow and the outflow were controlled by the same peristaltic pump (Masterflex L/S Easy-Load II) to ensure equal flow into and out of the perfusion chamber.

Electrogram recordings of isolated atria were obtained continuously during the experimentation period by placing custom-made platinum bipolar electrodes directly onto the atrial tissue. Electrodes were connected to an Iso-DAM8A amplifier system (World Precision Instruments) and signals were obtained at a sampling rate of 2000 Hz using the Spike 2 acquisition software, as described in Section 2.7.2 of Chapter 2. Tissues were given a 10 min equilibration period for the spontaneous beating rate to stabilize before imaging and image sequences were acquired in sinus rhythm and during pacing at a fixed cycle length of 100-ms. Electrical stimulation was provided by a custom-made platinum unipolar electrode. Capture threshold was determined by pacing at 100-ms cycle length and increasing the threshold amperage until 1:1 conduction was observed (*e.g.,* each electrical stimulation evoked an atrial signal) on the atrial electrogram recordings. Subsequent pulses were delivered at twice the threshold amperage. Because NOX2 is not constitutively active, the experiments described herein were conducted under basal conditions and using Ang-II (1 µmol/L, 30 min) to simulate ROS production from NOX2. Ang-II was chosen on the basis of previous studies demonstrating a rapid increase in NOX2-dependent ROS production in a number of cell systems and tissue preparations, including isolated

mouse atrial [245] and ventricular cardiomyocytes [207, 208] and human vascular smooth muscle cells [246].

Image sequences of up to 4000 frames were captured at 1000 frames/sec using GView, a custom-written optical mapping software (courtesy of Professor Gil Bub of McGill University, Canada). The data is saved as a series of 128-by-128 matrixes and each pixel represents a measure of fluorescence intensity acquired from a specific location on the tissue preparation. To estimate atrial APD and epicardial CV, zoomed images of the left and right atria were acquired. The processing and analysis of this data is described below.

5.2.1.3 Processing and Analysis of Optical Imaging Data

5.2.1.3.1 Action Potential Duration

Image sequences were processed using the GView software. The graphical interface allows users to select regions of interest on the image (corresponding to specific anatomical features of the atria) and generates a time series of optical action potentials that is exported as plain text. Optical action potentials were obtained from five different 12-by-12 pixel regions and APD values were computed from inverted fluorescence data using custom-written MATLAB scripts (version R2015a, Mathworks) that were developed in collaboration with Dr Klemen Ziberna and based on the methods and recommendations provided by Laughner *et al*. [247]. The steps used to obtain APD values are illustrated in Figure 5.3 and summarized below.

First, baseline drift in the raw optical recordings was corrected by fitting a fifth-order polynomial and subtracting that from the raw signal to establish a constant baseline level (Figure 5.3-B). A bi-directional filter (5^{th} order Butterworth filter) with a 100 Hz cut-off was then applied to the fluorescence trace to reduce high frequency noise (>100 Hz) and increase the signal-to-noise ratio (Figure 5.3-C). Next, individual action potentials were identified using the *findpeaks* function which locates the local maxima within the trace (Figure 5.3-C). To ensure the software did not detect unwanted peaks buried in noise, a minimum peak interval and amplitude was defined.

Action potentials were then analysed to determine the amplitude and activation and repolarization times. The amplitude was given by the difference between the maximum value and the baseline of the fluorescence trace which was an average of 50 frames preceding the action potential upstroke. The activation time was determined as the time of the first derivative of the fluorescence signal (dF/dt) corresponding to the steepest segment, or the maximum slope, of the action potential upstroke (Figure 5.3-D). Repolarization time was measured as a time when a specified level of repolarization (30%, 50% and 80%) was reached during the repolarization phase of the action potential (Figure 5.3-E). APD was calculated as the difference between repolarization and activation times and averaged to give an estimate of the global APD in each atria. The standard deviation of APD_{80} values measured between successive action potentials and between different sites in each atria was used an index of temporal and spatial APD heterogeneity, respectively.

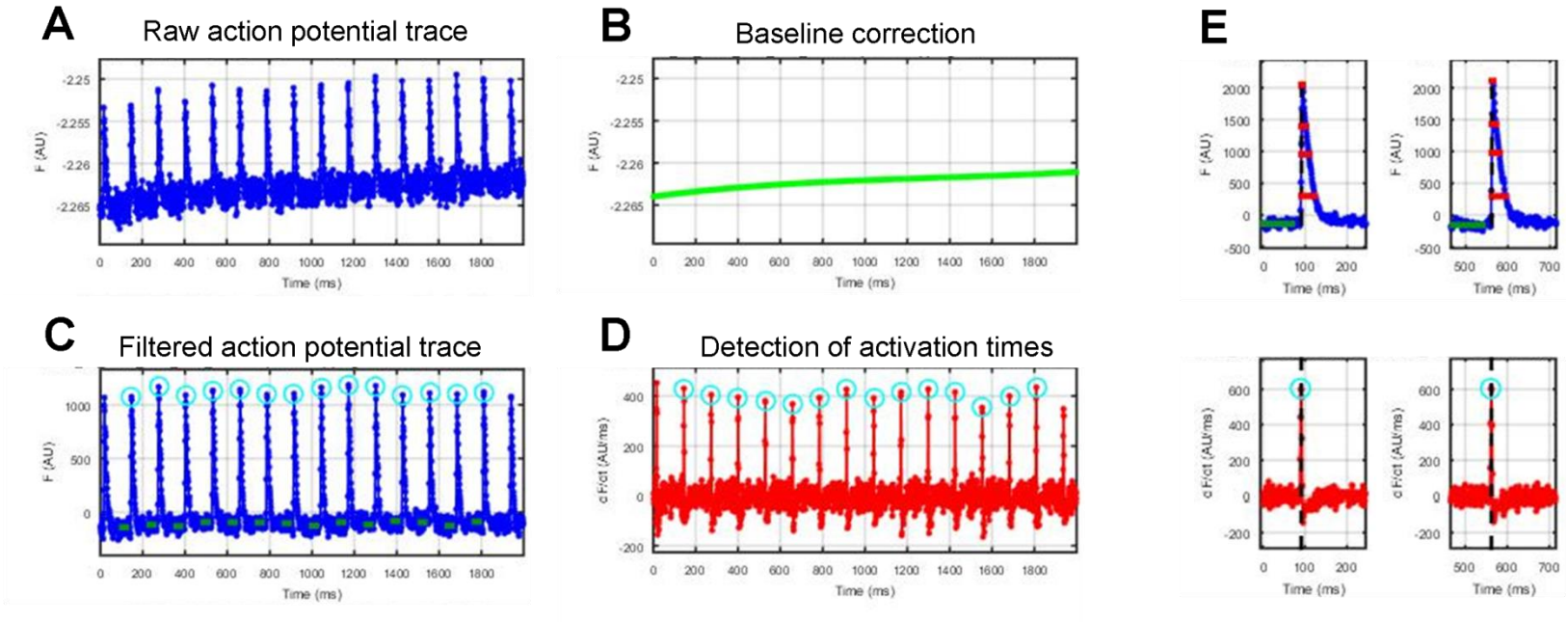

Figure 5.3: Processing and analysis of optical action potentials. A time course (2000 frames at 1000 frames/second) of optical action potentials (**A**) was obtained by selecting a region of interest on the optical images and traces were saved as plain text and imported into MATLAB. **B,** The baseline drift (green trace) was corrected by fitting a 5th-order polynomial and subtracting that from the raw signal to establish a constant baseline level. **C,** The action potential trace is further processed by applying a 5th order Butterworth filter with a 100 Hz cut-off to remove high frequency noise and individual action potentials are identified using the *findpeaks* function. The blue circle annotates the local maxima within the trace, corresponding to the peak of each action potential. **D,** The upstroke of each action potential was then differentiated and then peak of the differentiated signal (blue circle) was used to define the activation time (*e.g.*, steepest segment or maximum slope of the action potential upstroke). **E,** The action potential amplitude was calculated as the difference between the maximum value and the baseline of the fluorescence trace (average of 50 frames preceding the action potential upstroke, annotated in green), and APD30, APD50, and APD80 were calculated as the difference between activation time and repolarisation time at 30%, 50%, and 80% of the amplitude of the descending tail of the signal, respectively.

5.2.1.3.2 Conduction Velocity

Epicardial conduction velocities were analysed from optical image sequences using the *Ccoffinn* (Cardiomyocyte Cultures Optically-mapped: Fast Feature extractIoN and trackiNg) toolkit implemented in MatLab (courtesy of Jakub Tomek, University of Oxford) [221]. *Ccoffinn* is a tool that constructs a representation of cardiac waves and tracks their movement, using that information to describe the properties of the observed waves. Specific details describing the methodology are found in reference [221] and summarized here. On a frame by frame basis, a peak-finding algorithm identifies the location of pixels that are activated in each frame of the recording (to estimate which parts of the tissue are firing in a synchronized manner) and groups them together as 'wavefronts'. From this, waves are detected frame by frame and the movement of wavefronts is tracked throughout the recording. Importantly, this process is automated which allows for high throughput analysis of wave propagation and conduction velocity and minimizes operator bias. The process of identifying and tracking waves through a typical recording is shown in Figure 5.4. The tracking information (speed, distance, and direction) is then used to extract the conduction velocity of each wavefront. The mean (*e.g.* average of all wavefronts in the activation sequence) and maximum conduction velocities (*e.g.* fastest wavefront in the activation sequence) were calculated and averaged for each atria during sinus rhythm.

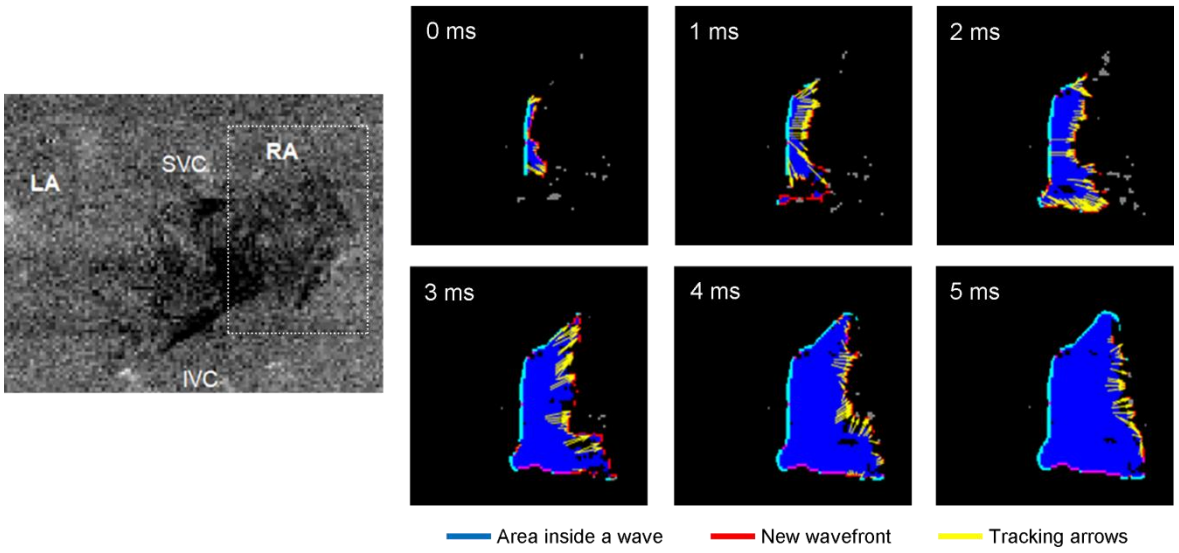

Figure 5.4: Conduction velocity analysis with the *Ccoffinn* toolkit. Gray-scale image illustrates right atrial activation collected by optical mapping of a di-4-ANEPPS-stained atrial preparation. To estimate epicardial conduction velocity, the zoom factor is increased so that only one atria is visible in the viewing window. This increases the number of pixels per unit area which increases the spatial resolution and decreases the signal-to-noise ratio. The time sequence (1 ms apart) illustrates an example output of frame-by-frame wave segmentation and tracking using the *Ccoffinn* toolkit during the sequence of activation in the right atria. Annotation in blue corresponds to the location of pixels that are activated in each frame of the recording, in red corresponds to the new wavefront in each frame (*e.g.*, the front edge of the propagating wave), and in yellow corresponds to the tracking arrows that link the pixels activated in one frame to those activated in the succeeding frame. The length of each tracking arrow is equal to the conduction velocity of an individual wavelet and the mean value of all tracking arrows in a sequence of activation (5 consecutive frames in this example) is the mean conduction velocity in that region of the tissue.

5.2.2 Statistical Analysis

All optical imaging experiments were performed in a blinded manner and genotypes were only decoded after completion of the measurements. Power calculations of sample size were determined using GPower 3.1 as described in Section 2.10 of Chapter 2. Based on a pilot study assessing APD, it was determined that a total of 26 atria (13 atria/genotype) would provide 90% power to identify an effect size of 1.36 with a 5% significance level. Data collected from several atria was not analyzed due to poor signal to noise ratio which made it difficult to detect individual wavefronts; therefore the final numbers presented in this chapter are 11 WT and 10 NOX2-Tg atria. Statistical significance was determined by two-tailed unpaired Student's t-test or Mann-Whitney *U* test, as deemed appropriate.

5.3 Results

5.3.1 Spatiotemporal patterns of atrial repolarization in WT and NOX2-Tg mice

Electrophysiologic remodelling of the atria, consistent with a shortening of the atrial APD, predisposes to AF [72]. Using optical imaging of di-4-ANEPPS-stained atrial preparations to measure APD, I characterized the impact of NOX2 overexpression on atrial repolarization. These experiments were performed under basal conditions and during NOX2 stimulation with Ang-II (1 μmol/L for 30 minutes). Optical action potentials were recorded from at least five different regions in each atrium and APD30, APD50, and APD80 were calculated and averaged to obtain an estimate of the global duration of repolarization in each atrial chamber. Global APDs were not significantly different ($P>0.05$) between WT and NOX2-Tg atria at baseline (Figure 5.5) or in response to Ang-II exposure ($P>0.05$), as shown in Figure 5.6.

As dispersion of repolarization throughout the atrial tissue (*i.e.*, heterogeneity of the APD) also provides a favourable substrate for AF [248, 249], I further characterized the spatial inhomogeneity of repolarization and beat-to-beat changes in the repolarization pattern (*e.g.*, temporal heterogeneity) by measuring the standard deviation of APD80 values between different regions of interest in each atria and between successive action potentials with each region, respectively. As summarized in Figure 5.7, both spatial and temporal dispersion of repolarization were found to be similar between genotypes under all of the experimental conditions examined.

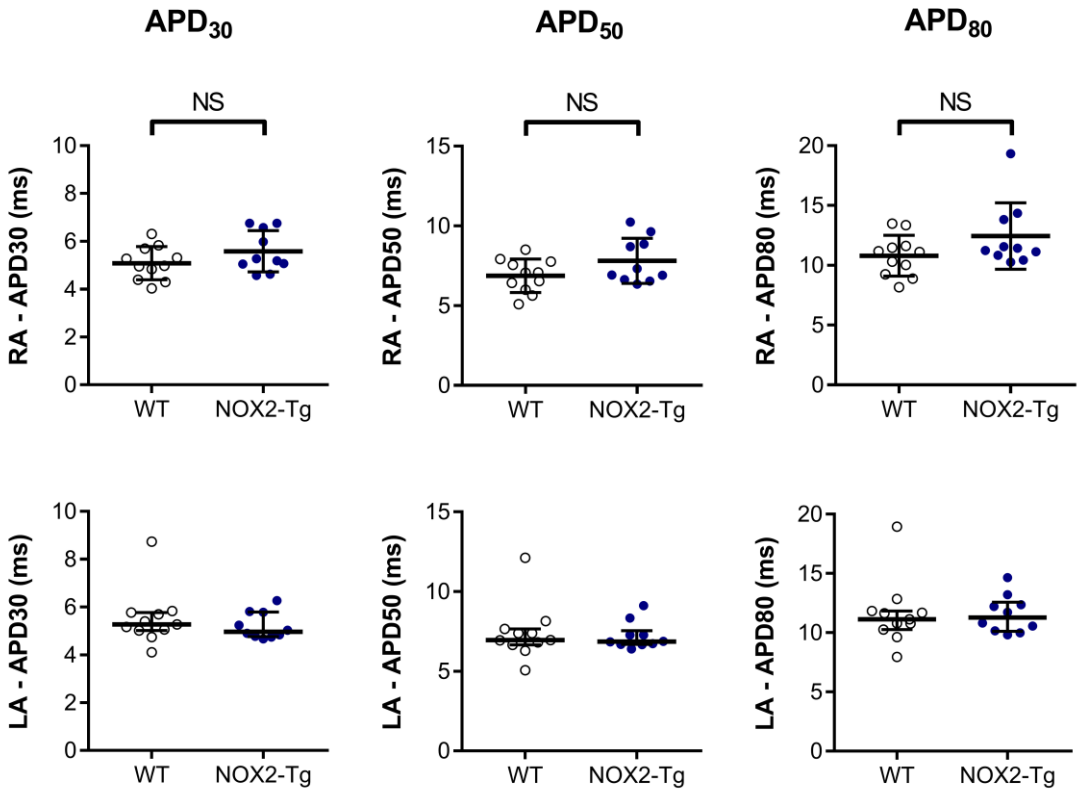

Figure 5.5: Action potential duration of WT and NOX2-Tg atria at baseline. Summarized data for APD30, APD50 and APD80 in the RA (*top*) and LA (*bottom)* shows no significant differences between WT and NOX2-Tg mice. Data shown as individual values with mean ± SD or median (25^{th} to 75^{th} percentile), as appropriate. Each point represents the mean value of a minimum of ten action potentials from five different regions of interest. Statistical significance between groups was determined using unpaired Student's t-test or Mann-Whitney *U* test. n = 11 and 9-10 for WT and NOX2-Tg atria, respectively. NS – not statistically significant.

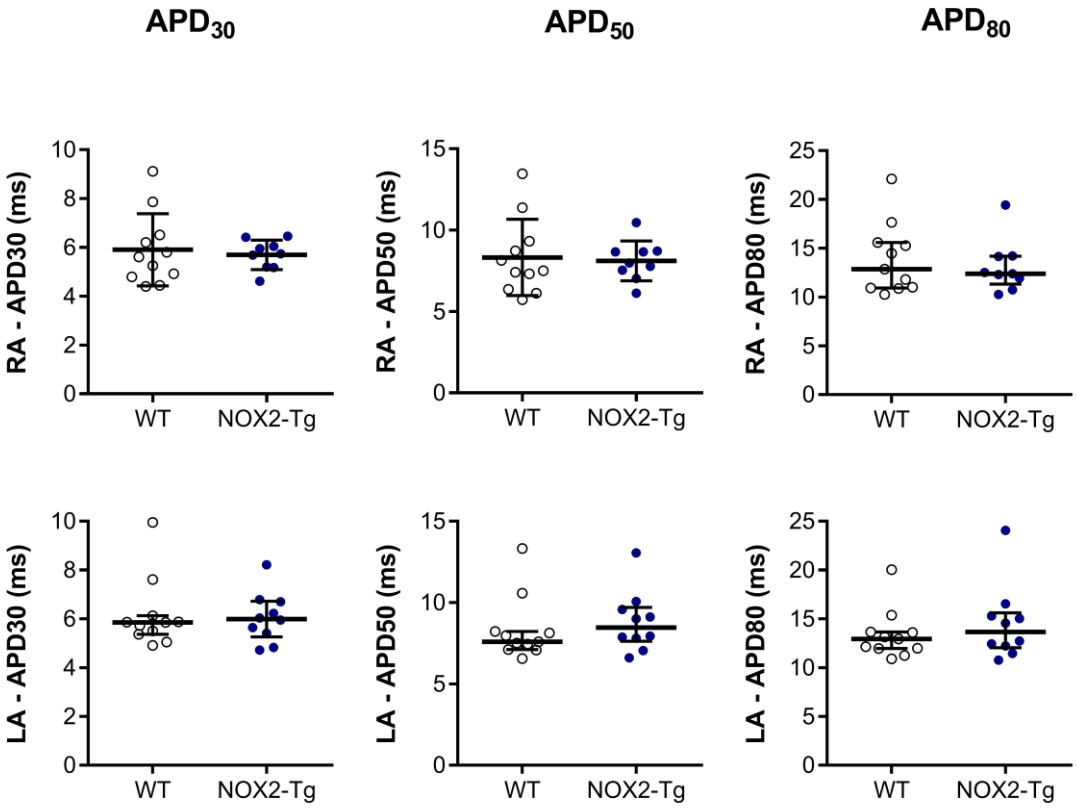

Figure 5.6: Action potential duration of WT and NOX2-Tg atria following acute stimulation with Ang-II. Summarized data for APD30, APD50 and APD80 in right (*top*) and left (*bottom*) of WT and NOX2-Tg mice show no significant differences between groups. Data shown as individual values with mean ± SD or median (25^{th} to 75^{th} percentile), as appropriate. Statistical significance between groups was determined using unpaired Student's t-test or Mann-Whitney *U* test. n = 11 and 9-10 for WT and NOX2-Tg atria, respectively.

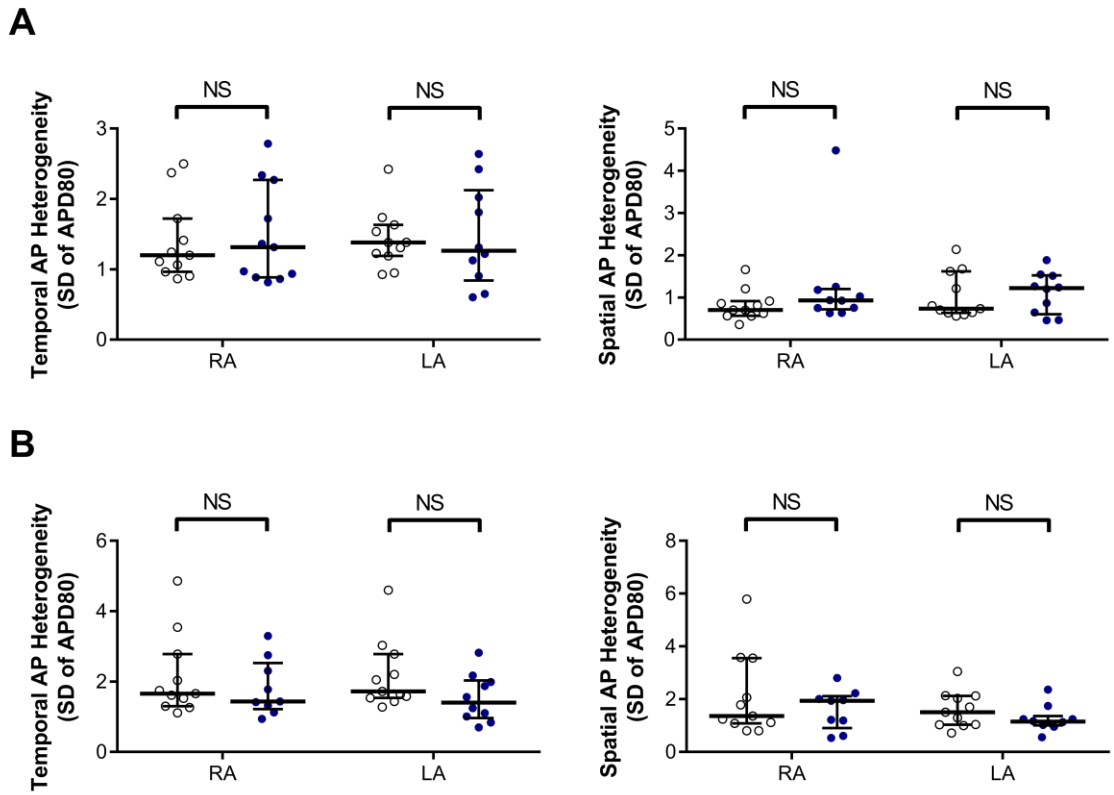

Figure 5.7: Spatial and temporal dispersion of atrial repolarization in WT and NOX2-Tg atria. The standard deviation of APD80 between successive action potentials and between different regions of interest within each atrium was used as a measure of temporal and spatial action potential repolarization heterogeneity, respectively. There were no significant differences in APD80 heterogeneity between WT and NOX2-Tg atria at baseline (**A**) and in response to Ang-II stimulation (**B**). Data shown are individual values with median (25^{th} to 75^{th} percentiles). Statistical significance between groups was determined using Mann-Whitney *U* test. n = 11 and 9-10 for WT and NOX2-Tg atria, respectively. NS – not statistically significant, SD – standard deviation, AP – action potential

5.3.2 Atrial conduction velocities in WT and NOX2-Tg mice

To determine the effect of NOX2 overexpression on atrial conduction, I next compared atrial activations maps and atrial conduction velocities between WT and NOX2-Tg mice. Spontaneous impulse generation during normal sinus rhythm was observed to originate in regions of the sinus node (region bounded by the crista terminalis, superior vena cava, and right atria [1]) and spread rapidly and uniformly toward the left and right atria. This pattern of activation was consistent between WT and NOX2-Tg atrial tissues at baseline (Figure 5.8) and in response to Ang-II (Figure 5.9). To compare the spread of depolarization between WT and NOX2-Tg atria, I also quantified the CV of propagating action potentials. Image sequences of up to 4000 frames (recorded at 1000 frames/second) were analyzed using the *Ccoffinn* analysis toolkit according to the methods described in Section 5.2.3.1 of this chapter and Figure 5.4. Analysis of the wavefront CV within each atria revealed no significant differences ($P>0.05$) in maximum or mean CV between WT and NOX2-Tg atria under any of the conditions examined (Figure 5.8 and Figure 5.9).

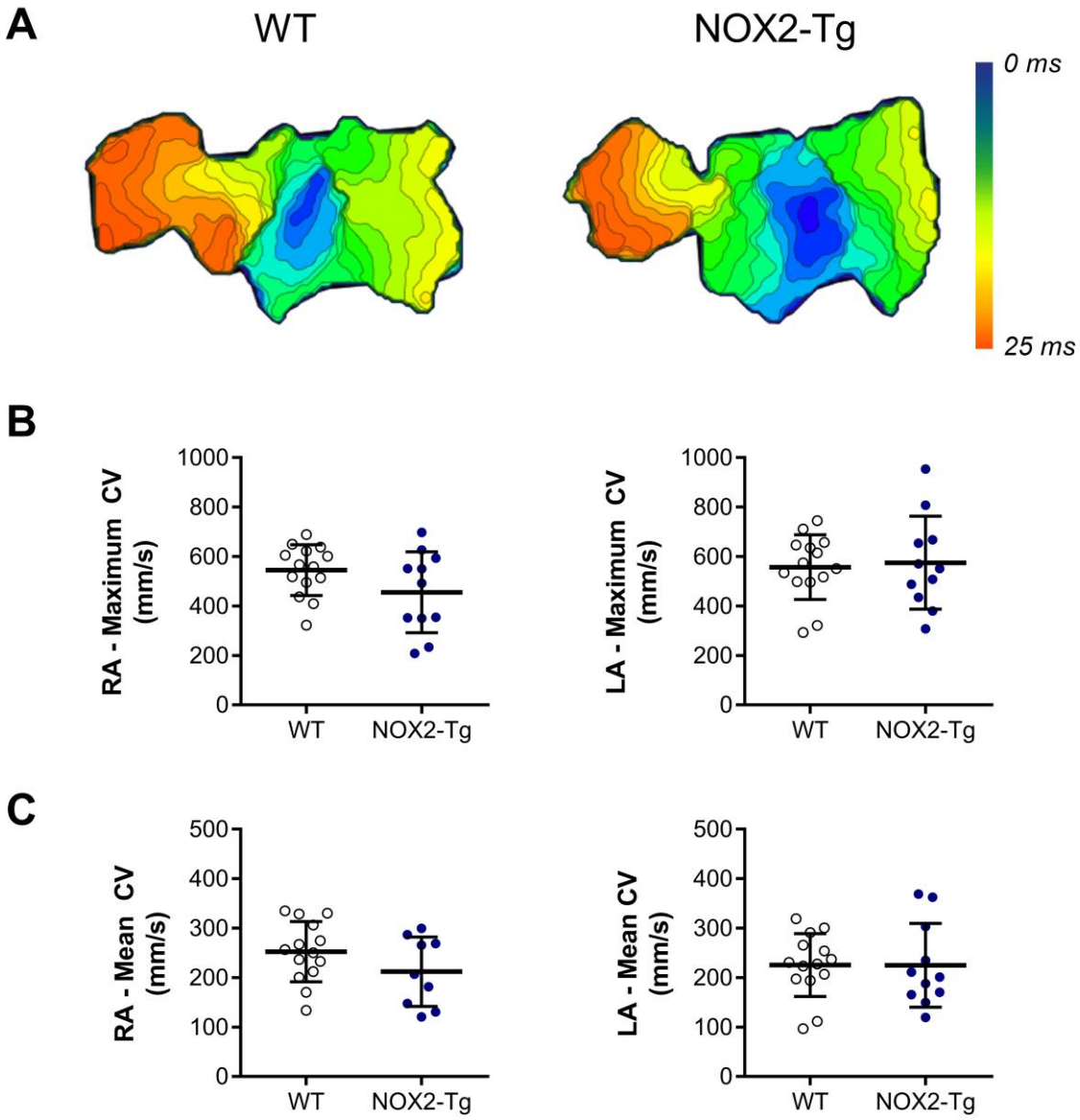

Figure 5.8: Atrial conduction velocities are similar between WT and NOX2-Tg mice at baseline. A, Representative activation maps of a single spontaneous wave depolarization in WT and NOX2-Tg atrial tissues showing similar patterns of impulse conduction between genotypes. Action potential initiation is shown in blue, with excitation of distal regions shown in orange. Each isochrone line represents 1 ms. Summarized CV data show no significant differences in maximum (**B**) or mean (**C**) CV in the RA or LA between genotypes. *n* = 14 and 11 for WT and NOX2-Tg atria, respectively. Data shown as individual values with mean ± SD. Statistical significance between groups was determined using unpaired Student's t-test.

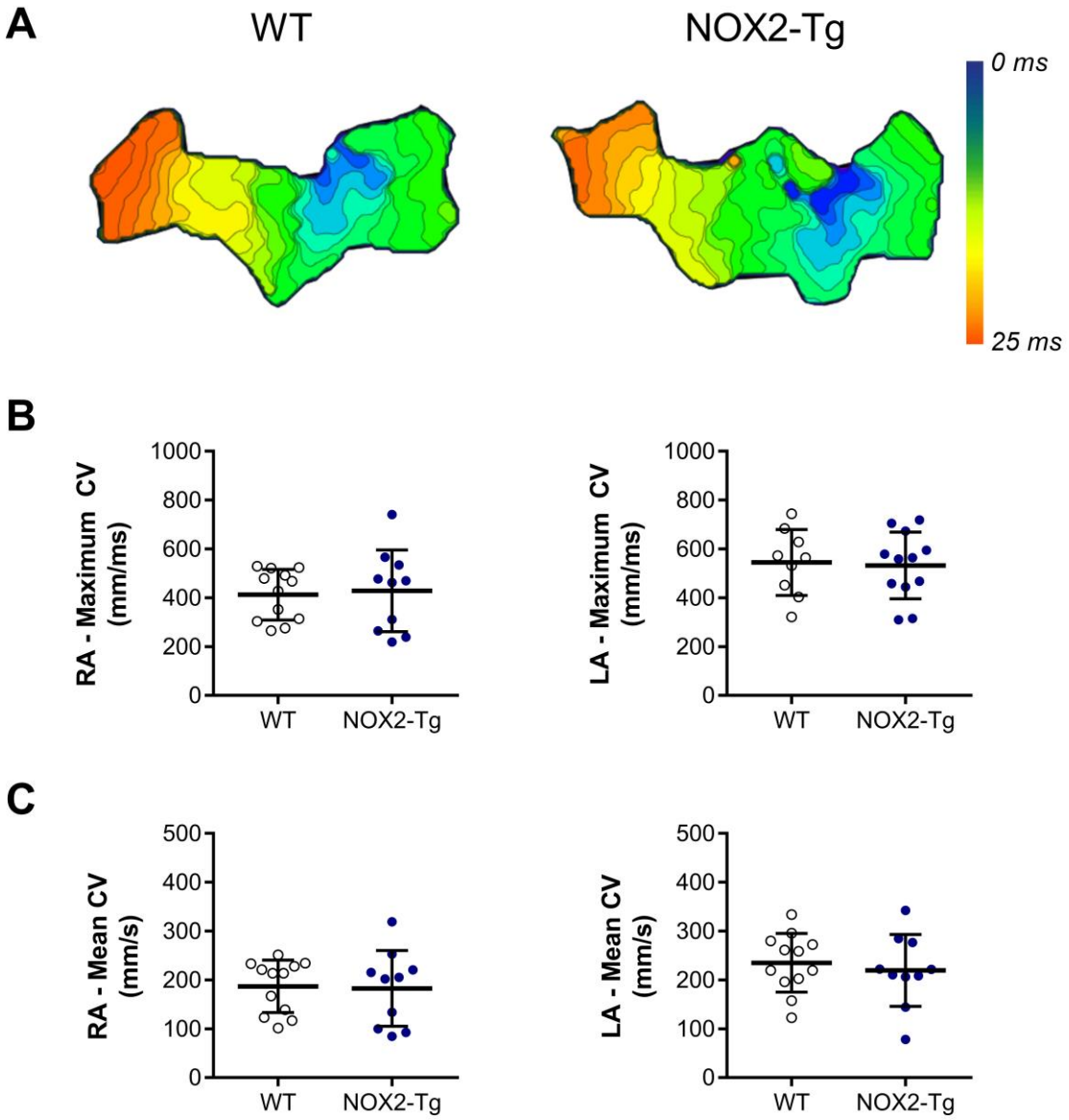

Figure 5.9: Atrial conduction velocities are similar between WT and NOX2-Tg mice following acute stimulation with Ang-II. A, Representative activation maps of a single spontaneous wave depolarization in WT and NOX2-Tg atria exposed to Ang-II (1 µmol/L for 30 minutes) showing similar patterns of impulse conduction between genotypes. Action potential initiation is shown in blue, with excitation of distal regions shown in orange. Each isochrone line represents 1 ms. Summarized CV data show no significant differences in maximum (**B**) or mean (**C**) CV in the RA or LA between genotypes. *n* = 14 and 11 for WT and NOX2-Tg atria, respectively. Data shown as individual values with mean ± SD. Statistical significance between groups was determined using unpaired Student's t-test.

5.4 Discussion

AF is characterized by a shortening of the atrial APD that facilitates the progression from paroxysmal to persistent/chronic AF. This was originally demonstrated by Wijffels *et al.* [72] in a goat model of pacing-induced AF, where the progression from short, self-terminating episodes of AF to chronic AF was accompanied by a reduction in the APD (by as much as 45%). Persistent AF in humans is also associated with a reduction in the atrial APD [73-75]. Given that upregulation of NOX2 activity and expression occurs in the early stages of AF development (*e.g.*, in patients with paroxysmal [128] and post-operative AF [138, 142, 143], and within two weeks of rapid atrial pacing in a goat model [138]), a valid assumption is that increased NOX2 activity might promote AF by shortening the atrial APD.

Our data showing no significant differences in the APD of left and right atria between WT and NOX2-Tg mice suggests that this is unlikely to be the case and is consistent with previous findings reported by Wagner and colleagues [208]. Using $gp91^{phox}$-deficient mice, they showed that the Ang-II-mediated increase in ROS in isolated ventricular myocytes requires the presence of NOX2; however, when they measured action potentials in isolated ventricular myocytes, the authors reported no significant differences in duration or diastolic membrane potential between WT and $gp91^{phox}$-deficient myocytes [208]. In fact, Ang-II-dependent activation of NOX2 was shown to increase peak I_{CaL} and I_{Na} which would be expected to prolong the duration of action potentials.

Structural remodelling also forms an important substrate for the development of AF by promoting slow and/or heterogeneous electrical impulse conduction [4]. Although the mechanistic link between altered NOX2 activity and structural impairment in AF is unknown, the involvement of NOX2 was previously suggested by a number of observations. For instance, mice with cardiac-specific overexpression of constitutively active Rac1, a necessary activator of NOX2, were found to develop AF spontaneously and to exhibit an increase in atrial NADPH-stimulated ROS production [145], in association with increased fibrosis and up-regulation of CTGF and N-cadherin [145, 226]. By the same token, Ang-II, a potent stimulator of $O_2^{\cdot -}$ production from NOX2 and a

major pro-fibrotic signalling molecule, is up-regulated in atrial tissues of patients with AF [250]. Likewise, NOX2 activity in cardiac myocytes is increased by stretch [202] which has also been shown to activate TNF-α [251, 252], a potent stimulator of atrial fibrosis [253].

However, we observed similar conduction patterns in the atria of WT and NOX2-Tg mice under basal conditions and in response to Ang-II, as shown by the atrial activation maps. We also observed no significant differences in mean or maximum CV between genotypes. These data suggest that NOX2 overexpression alone does not promote atrial structural remodelling and is consistent with our *in vivo* data showing no differences in P wave duration or PQ interval between genotypes and no evidence of spontaneous AF, which is commonly observed in transgenic mouse models with atrial dilatation and fibrosis [254].

In summary, our optical mapping data suggest that electrical and structural remodelling are unlikely to underlie the enhanced arrhythmogenesis in NOX2-Tg mice *in vivo.* Notwithstanding the importance of APD shortening and conduction slowing for the maintenance of AF, it is widely accepted that triggered activity, resulting from impaired Ca^{2+} handling, contributes significantly to initiating AF. By promoting RyR2 Ca^{2+} release [202, 208], enhanced NOX2 activity may promote AF by triggering spontaneous action potentials (*e.g.,* delayed afterdepolarizations). This hypothesis will be tested in **Chapter 6**.

6 Effect of NOX2 Overexpression on Diastolic Ca^{2+} Leak

6.1 Introduction

Abnormalities in intracellular Ca^{2+} handling feature prominently in AF. In particular, diastolic SR Ca^{2+} leak through RyR2 has been suggested to promote AF by inducing spontaneous electrical activity (*e.g.*, diastolic depolarizations) [4]. As outlined in Chapter 1, I_{CaL} produces a local rise of $[Ca^{2+}]_i$ that initiates robust Ca^{2+} release from the SR through RyR2 during excitation-contraction coupling [31]. In addition, individual (or clusters of) RyR2 channels have also been shown to open randomly during diastole, mediating a measurable SR Ca^{2+} leak in the form of non-propagating Ca^{2+} sparks [255]. These spontaneous local increases in $[Ca^{2+}]_i$ are usually confined to a single Ca^{2+} release unit (within ~2 μm) because RyR2 clusters are spatially separated and the amount of Ca^{2+} released from one cluster is too small to trigger release from neighbouring clusters. However, under conditions when cytosolic or SR Ca^{2+} concentrations are elevated, or RyR2 channels are otherwise sensitized (*e.g.*, by post-translational modifications and/or regulatory proteins), enhanced diastolic Ca^{2+} leak can trigger Ca^{2+} sparks at neighbouring RyR2 clusters and produce cell-wide waves of Ca^{2+}-induced Ca^{2+} release. These waves are potentially arrhythmogenic as they are able to drive a substantial inward current (via the electrogenic NCX) which in turn may trigger global membrane depolarizations and premature action potentials.

Hove-Madsen *et al.* [256] were the first to study the patterns of SR Ca^{2+} release in AF patients, showing an increase in the frequency of Ca^{2+} sparks and Ca^{2+} waves that were capable of generating triggered action potentials in right atrial myocytes from patients with a history of AF compared with patients in sinus rhythm. In addition, AF patients had larger spontaneous inward currents/depolarizations at resting (-80 mV) and partially depolarized (-50 mV) holding potentials, indicating increased I_{NCX} [256]. Although that particular study did not distinguish between types of AF, subsequent work showed this to be the case in paroxysmal [257] as well as chronic AF [111,

258]. In the case of paroxysmal AF, these changes were observed to occur in the absence of reductions in I_{CaL} or APD (*e.g.*, preceding AF-related electrical remodelling) supporting the notion that Ca^{2+}-dependent ectopic/triggered activity may facilitate the initiation of AF.

The occurrence of abnormal diastolic SR Ca^{2+} release in AF results from SR Ca^{2+} overload and/or intrinsic RyR2 dysfunction. One of the fundamental properties of the RyR2 channel is the activation by Ca^{2+} in the SR lumen, which is manifested as an increase in SR Ca^{2+} leak (or Ca^{2+} spark frequency) at a higher SR Ca^{2+} load [115]. In paroxysmal AF, sensitization of RyR2 by elevated SR Ca^{2+} contributes to the generation of diastolic Ca^{2+} leak and the occurrence of delayed after-depolarizations, with SR Ca^{2+} uptake likely driven by PKA-dependent phosphorylation of PLN (inhibitor of SERCA2a in its dephosphorylated state) [257]. RyR2 expression was also increased in paroxysmal AF and shown to contribute to the spontaneous diastolic SR Ca^{2+} release events in right atrial cardiomyocytes [257]. Likewise, an increase in SR Ca^{2+} content has been described in canine models of congestive heart failure-related AF, where CaMKII-dependent phosphorylation of PLN was shown to drive SR Ca^{2+} uptake [119].

RyR2 has a number of regulatory binding sites and serves as a scaffold for a myriad of accessory proteins, including PKA, CaMKII, FKBP12.6, PP1 and PP2A, and PDE-4D3 on the cytosolic side, and calsequestrin, triadin, and junctin on the SR luminal side [259]. Consequently, RyR2 open probability is modulated indirectly by post-translational modifications (*e.g.*, phosphorylation) or via direct interaction with stabilizer proteins (*e.g.*, triadin, junction, FKBP12.6) that alter RyR2 Ca^{2+}-sensitivity [259-263]. Changes in RyR2 phosphorylation have been reported consistently in chronic AF and suggested to account for the enhanced diastolic Ca^{2+} leak observed in these patients [111, 258]. In the right atria of chronic AF patients, RyR2 is hyper-phosphorylated by CaMKII at Ser2814 [258], possibly resulting from increased expression and Thr-287 auto-phosphorylation (and thus activity) of CaMKII [111, 258]. Moreover, inhibition of CaMKII reduced RyR2-dependent Ca^{2+} leak and prevented the development of spontaneous Ca^{2+} release events and delayed afterdepolarizations [111, 258]. In support, pharmacological inhibition of CaMKII and genetic inhibition of CaMKII-dependent RyR2 phosphorylation were also shown to prevent AF initiation in mice with a genetic gain of function defect in RyR2 [113]

and in mice with chronic (3 weeks) infusion of Ang-II [156]. PKA-dependent phosphorylation of RyR2 (at Ser2808) is also increased in chronic AF and appears to cause RyR2 Ca^{2+} leak by mediating the dissociation of FKBP12.6 [121], a high affinity RyR2 binding protein that stabilizes the closed state of the channel [263].

RyR2 activity is also influenced by the prevailing myocardial redox state [152]. Endogenous ROS, including $O_2\cdot^-$, H_2O_2, and OH^- can modulate RyR2 function by direct oxidation of cysteine thiol (sulfhydryl) residues [264], as well as indirectly through phosphorylation by the redox-sensitive kinases PKA and CaMKII [265]. Of particular relevance to the work being undertaken in this thesis, activation of RyR2 by NOX2-derived ROS has been linked to aberrant Ca^{2+} release and arrhythmias in the diseased myocardium. NOX2 is expressed in sarcolemmal/t-tubule membranes of ventricular myocytes and in close proximity to RyR2 channels [202], and has been shown to fine-tune RyR2 Ca^{2+} release in excitation-contraction coupling [202, 206, 207]. However, augmented NOX2-mediated ROS production has also been reported to promote Ca^{2+} wave generation in isolated ventricular myocytes from the *mdx* mouse model of muscular dystrophy [202] and may underlie ventricular arrhythmogenesis in these hearts [209].

Furthermore, Wagner and colleagues presented data demonstrating that increased NOX2-dependent ROS production downstream of Ang-II promotes diastolic SR Ca^{2+} leak and cellular arrhythmias by activating CaMKII [208]. Experiments conducted on isolated ventricular myocytes showed that Ang-II increased the frequency of Ca^{2+} sparks (a measure of SR Ca^{2+} leak) and delayed afterdepolarizations in WT but not $gp91^{phox}$-deficient or CaMKII-deficient myocytes [208]. NOX2-derived ROS can activate CaMKII by direct oxidation of methionine residues in the CaMKII regulatory domain [265] or by promoting auto-phosphorylation of Thr-287 in the auto-inhibitory region of CaMKII [208].

Unlike the ventricular myocardium, the effects of NOX2-derived ROS on RyR2 function and Ca^{2+} signalling have not been studied in the context of atrial arrhythmias. Accordingly, the work in this chapter investigates whether NOX2-derived $O_2\cdot^-$ alters atrial Ca^{2+} handling and tests the hypothesis that NOX2-derived $O_2\cdot^-$ promotes pacing-induced AF in NOX2-Tg mice by increasing diastolic SR Ca^{2+} release through RyR2.

6.2 Methods

The following procedures were performed in this chapter as described in detail in Chapter 2:

- 2.2 Tissue Collection and Processing
- 2.4 Western Blot Analysis
- 2.9 Studies on Isolated Atrial Myocytes
    - 2.9.1 Atrial Myocyte Isolation
    - 2.9.2 Measurement of Diastolic RyR2 Ca^{2+} Leak
- 2.10 Statistical Analysis

Specific details relevant to this chapter are provided below.

6.2.1 Measurement of Diastolic Ca^{2+} Leak

Measurements of RyR2 diastolic Ca^{2+} leak were performed as described in Section 2.9 of Chapter 2, on individual right and left atrial myocytes from NOX2-Tg mice and their WT littermate controls, using Ang-II (1 μmol/L) to stimulate $O_2{\cdot}^-$ production from NOX2. These experiments were performed with 1.8 mmol/L extracellular [Ca^{2+}] and field-stimulation at a frequency of 2 Hz. $[Ca^{2+}]_i$ transients were analyzed for diastolic $[Ca^{2+}]_i$, amplitude, and rate of decay (tau), and the SR Ca^{2+} content was measured by rapid application of caffeine (10 mmol/L). RyR2 leak was analyzed as the tetracaine-dependent shift in cytosolic $[Ca^{2+}]_i$ (Figure 6.1). The leak-load relationship was calculated by plotting the RyR2 leak as a function of the SR load.

It should be emphasized that the experiments described herein were only conducted in the presence of Ang-II; we did not assess intracellular Ca^{2+} handling and diastolic Ca^{2+} leak under basal conditions. This was decided partly for technical reasons, as power calculations determined that we would need approximately 40 myocytes/atria/genotype (details provided below) and atrial myocyte isolations are technically challenging with relatively low yield of high-quality calcium-tolerant cardiomyocytes. Furthermore, because NOX2 is not constitutively active in a cellular

context and intracellular Ca^{2+} handling is preserved in NOX2-Tg ventricular myocytes compared with WT controls [207], we did not expect to see a difference in atrial myocyte Ca^{2+} handling between WT and NOX2-Tg mice. Ang-II was chosen on the basis of previous studies demonstrating an increase in NOX2-dependent ROS production in murine atrial [245] and ventricular cardiomyocytes [207, 208].

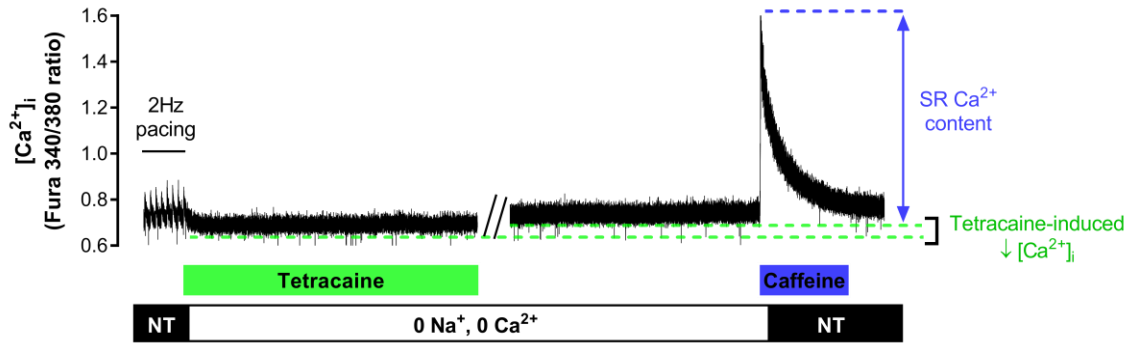

Figure 6.1: Protocol for assessment of diastolic SR Ca^{2+} leak. Atrial myocytes are field-stimulated at 2 Hz and 1.8 mmol/L extracellular [Ca^{2+}] until steady-state $[Ca^{2+}]_i$ is reached. Pacing was then stopped and the bath solution was switched to a Na^+-free, Ca^{2+}-free solution containing tetracaine (1 mmol/L) for 60 seconds. The solution was changed again to a Na^+-free, Ca^{2+}-free solution without tetracaine for 90 seconds followed by a pulse of caffeine (10 mmol/L) to release Ca^{2+} from the SR. SR Ca^{2+} leak through RyR2 is then quantified as the tetracaine-dependent change in diastolic $[Ca^{2+}]_i$ during the periods of Na^+-free, Ca^{2+}-free Tyrode perfusion. NT – normal Tyrode

6.2.2 Western Blot Analysis

Sample preparation for western blotting was carried out as described in Section 2.4 of Chapter 2. For immunological detection of phosphorylated and total RyR2, 20 µg of homogenate protein was loaded onto NuPage 4-12% Tris-Acetate gradient gels (*ThermoFisher Scientific*) and electrophoretic separation was performed at 180 V for 90 minutes. Proteins were transferred onto nitrocellulose membranes at 250 mA for 180 minutes at 4 °C. Western blot transfer was performed and blotted onto nitrocellulose membranes. Membranes were incubated with blocking solution (5% non-fat milk in TBS containing 0.1% Tween-20 (TBS-T)) for 1 hour at room temperature and then incubated overnight at 4 °C with the following primary antibodies:

Phospho-RyR2-Ser2808 – 1:1 000 in 5% milk-TBS-T

Phospho-RyR2-Ser2814 – 1:5 000 in 5% milk-TBS-T

Total RyR2 – 1:500 in 2.5% milk-TBS-T

HRP-conjugated GAPDH – 1:25 000 in 0.1% BSA

Protein expression was detected using anti-rabbit HRP (1:50 000) or anti-mouse HRP (1:25 000) as the secondary antibodies for 1 hour at room temperature. Band intensities were detected and quantified using the ChemiDoc Imaging system (*Bio-Rad Technologies*) and data are presented by normalizing the densitometry signal obtained by the phosphorylated fraction to the total protein.

6.2.3 Statistical Analysis

Power calculations of sample size were determined using GPower 3.1 (*Universitat Dusseldorf, Germany*) as described in Section 2.10 of Chapter 2. Based on a pilot study assessing diastolic Ca^{2+} leak in left ventricular cardiomyocytes, it was determined that a total of 82 cardiomyocytes (41 cells/genotype) would provide 80% power to identify an effect size of 0.63 with α=0.05 (or a 5% significance level). This effect size is similar to that previously observed in atrial myocytes of mice with impaired diastolic closure of RyR2 Ca^{2+}-release channels [218].

Statistically speaking, Sikkel *et al.* [222] have suggested that $[Ca^{2+}]_i$ handling data collected from isolated cardiomyocytes shows considerable clustering (*e.g.* measurements from

multiple cells of the same animal on a given day are more similar than from different animals), such that common statistical tests that assume independence of data points may not be suitable to analyse this type of data. Therefore, statistical significance was determined by two-tailed unpaired Student's t-test or Mann-Whitney *U* test using a hierarchical statistical clustering model. This was performed using R and the lmerTest R package according to the methods described in the study by Sikkel *et al.* [222], and results were compared with common statistical approaches (un-paired Student's t-test). Any non-parametric data were log-transformed prior to analysis. Table 6.1 shows the analysis of $[Ca^{2+}]_i$ transient morphology using standard and hierarchical statistical tests. Apart from the $[Ca^{2+}]_i$ transient amplitude data obtained from the right atria, the hierarchical analysis did not produce a significantly better fit than the Student's t-test. Nevertheless, some degree of clustering of the Ca^{2+} data was observed (~10-30%), therefore *P*-values produced by the hierarchical analysis are reported.

Table 6.1: Statistical analysis of Ca^{2+} transient morphology

	Clustering of data (ICC) (%)	***P*-value**		**Comparison of goodness of fit**
		Student's t-test	**Hierarchical test**	
Right atria				
Diastolic calcium (Fura-2 ratio)	12	0.24	0.39	0.282
Log Transient amplitude (F/F_0)	28	0.044	0.22	**0.015 ***
Log Tau (ms)	18	0.056	0.21	0.079
Log Caffeine amplitude (F/F_0)	1.5e-12	0.57	0.56	1
Log Fractional release (%)	11	0.125	0.213	0.303
Left atria				
Diastolic calcium (Fura-2 ratio)	10	0.32	0.34	0.38
Log Transient amplitude (F/F_0)	18	0.03	0.085	0.15
Tau (ms)	17	0.76	0.79	0.11
Caffeine amplitude (F/F_0)	6	0.017	0.04	0.48
Fractional release (%)	12	0.93	0.98	0.30

Comparison of right and left atrial Ca^{2+} transient morphology between WT and NOX2-Tg mice using Student's t-test and hierarchical statistical tests. The interclass coefficient (ICC) quantifies the amount of clustering in the dataset (*e.g.*, 0% for data showing no clustering and 100% for intensely clustered data) and is used as a correction factor in the statistical analysis. $*P < 0.05$ indicates that the hierarchical technique is more appropriate for the analysis of calcium transient amplitude data obtained from the right atria.

6.3 Results

6.3.1 Intracellular Ca^{2+} dynamics in isolated atrial myocytes

Although the primary purpose of this study was to assess the link between NOX2-derived $O_2^{\cdot -}$ production and RyR2 Ca^{2+} leak, I began by characterizing atrial Ca^{2+} handling properties in WT and NOX2-Tg mice. Atrial cardiomyocytes were exposed to Ang-II (1 μmol/l for 20 minutes) to stimulate NOX2 activity and $[Ca^{2+}]_i$ transients were evoked by field-stimulating individual right and left atrial myocytes at 2 Hz with $[Ca^{2+}]_o$ = 1.8 mmol/L. There was no significant difference in the diastolic $[Ca^{2+}]_i$ in NOX2-Tg atrial myocytes compared with WT controls (*P* = 0.39 for RA; *P* = 0.34 for LA, Figure 6.2).

The $[Ca^{2+}]_i$ transient amplitude in NOX2-Tg myocytes tended to be higher than WT in both the RA ($F_{365/380}$: 0.192, 25th to 75th percentile: 0.14 – 0.28 for WT *vs* 0.253, 25th to 75th percentile: 0.17 – 0.35 for NOX2-Tg, *P* = 0.22; Figure 6.3-C) and LA ($F_{365/380}$: 0.146, 25th to 75th percentile: 0.096 – 0.21 for WT *vs* 0.177, 25th to 75th percentile: 0.12 – 0.29 for NOX2-Tg, *P* = 0.085; Figure 6.3-D), but this did not reach statistical significance. The $[Ca^{2+}]_i$ transient decay time constant (tau, τ) in RA (Figure 6.3-E) and LA myocytes (Figure 6.3-F) was not significantly different between genotypes, but tended to be shorter in transgenic RA myocytes when compared with WT controls.

Analysis of the caffeine-induced $[Ca^{2+}]_i$ transients revealed no significant differences in the SR Ca^{2+} content of RA myocytes between WT ($F_{365/380}$: 0.93, 25th to 75th percentile: 0.64 – 1.05) and NOX2-Tg hearts ($F_{365/380}$: 0.80, 25th to 75th percentile: 0.61 – 1.07; *P* = 0.56; Figure 6.4-A). However, the SR Ca^{2+} content in NOX2-Tg LA myocytes ($F_{365/380}$: 0.93, 25th to 75th percentile: 0.64 – 1.05) was significantly greater than in WT ($F_{365/380}$: 0.93, 25th to 75th percentile: 0.64 – 1.05; *P* = 0.04; Figure 6.4-B). The fractional release of Ca^{2+} (*e.g.*, the ratio of the $[Ca^{2+}]_i$ transient amplitude to the SR Ca^{2+} content) measured from RA and LA myocytes did not differ between the genotypes (Figure 6.5-A and Figure 6.5-B, respectively).

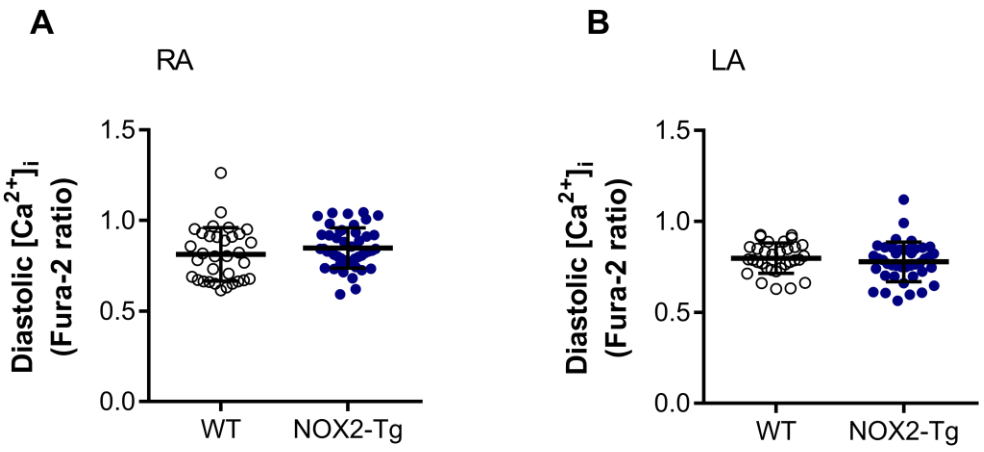

Figure 6.2: Diastolic $[Ca^{2+}]_i$ is unaffected by NOX2 overexpression. The diastolic $[Ca^{2+}]_i$ content in the RA ($F_{365/380}$: 0.81 ± 0.15 in WT *vs* 0.85 ± 0.11 in NOX2-Tg; n=33 and 46 cells from 9 mice per genotype, **A**) and the LA ($F_{365/380}$: 0.80 ± 0.08 in WT *vs* 0.77 ± 0.11 in NOX2-Tg; n=32 and 41 cells from 8 WT and 11 NOX2-Tg mice per genotype, **B**) did not differ between WT and NOX2-Tg mice. Data shown as individual data points with mean ± SD.

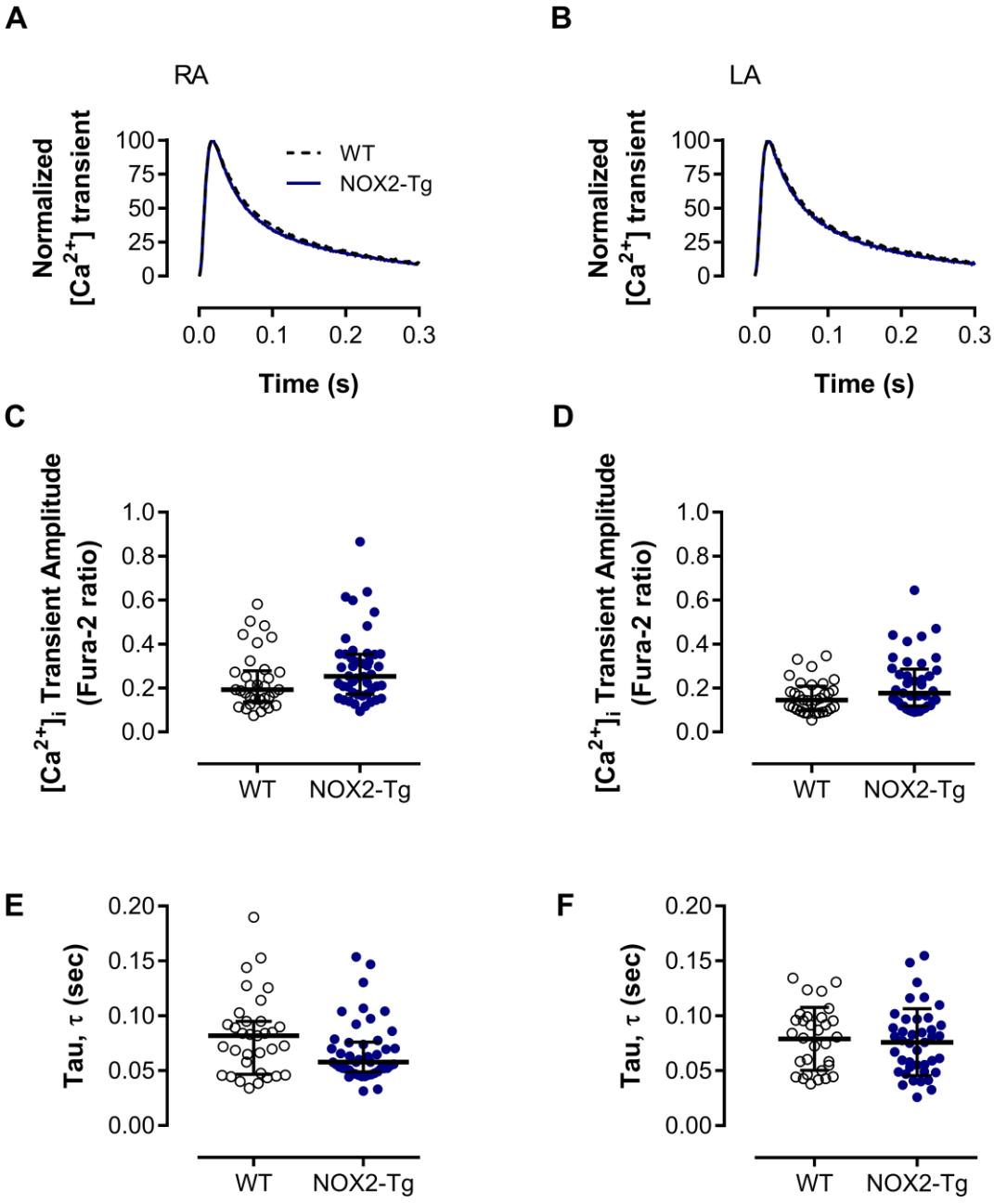

Figure 6.3: The $[Ca^{2+}]_i$ transient amplitude and rate of decay of the $[Ca^{2+}]_i$ transient are not significantly modified by NOX2 overexpression. Overlays of averaged and normalized Ca^{2+} transients from right (**A**) and left (**B**) atrial myocytes of WT and NOX2-Tg mice are shown. The amplitude of the $[Ca^{2+}]_i$ transient measured from RA (n=33 and 46 cells from 9 mice per genotype, P=0.22, **C**) and LA (n=32 and 41 cells from 8 WT and 11 NOX2-Tg mice, P=0.085, **D**) myocytes was not significantly different between genotypes, although the $[Ca^{2+}]_i$ transient amplitude tended to be longer in RA myocytes from NOX2-Tg mice. The rate of decay of the $[Ca^{2+}]_i$ transient (tau, in sec) measured from the same RA and LA myocytes was not different between genotypes. Data shown as individual data points with median (25^{th} to 75^{th} percentile).

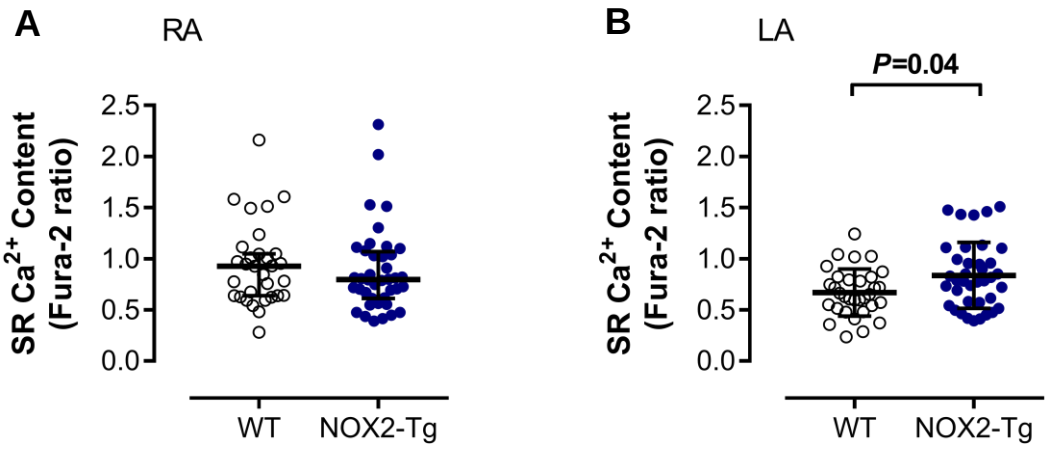

Figure 6.4: SR Ca^{2+} content in atrial myocytes from WT and NOX2-Tg mice. The SR Ca^{2+} content, measured from the amplitude of the caffeine-induced $[Ca^{2+}]_i$ transient, in RA myocytes (n=31 and 40 cells from 9 mice per group, **A**) did not differ between genotypes but was prolonged in LA myocytes (**B**) of NOX2-Tg mice (n=38 cells from 11 mice; 0.785, 25^{th}-75^{th} percentile: 0.56 – 1.02) compared with WT controls (n=32 cells from 8 mice; 0.64, 25^{th}-75^{th} percentile: 0.52 – 0.81; P = 0.04). Data shown as individual data points with median (25^{th} to 75^{th} percentiles).

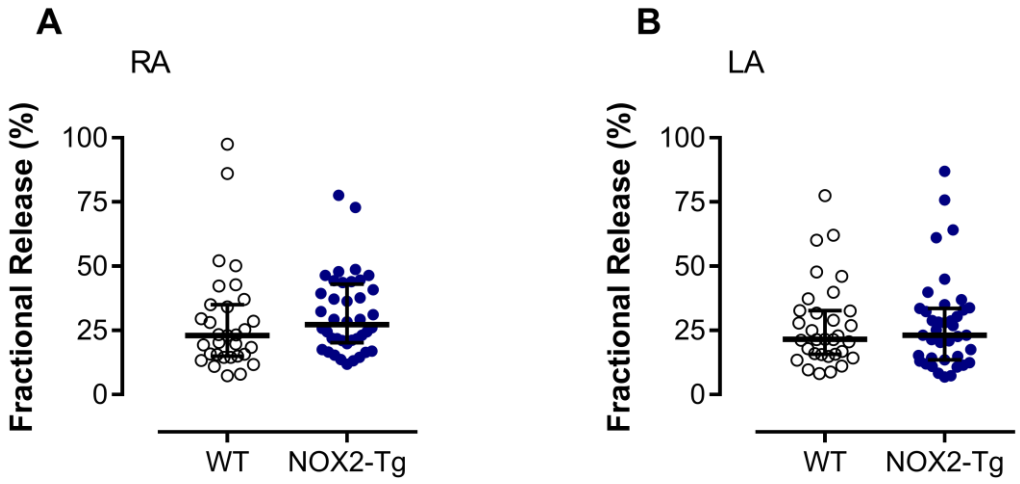

Figure 6.5: Fractional release was unaffected by NOX2 overexpression. The ratio of the $[Ca^{2+}]_i$ transient amplitude to the SR Ca^{2+} content (*e.g.*, the fractional release of Ca^{2+} from the SR) measured from RA (n=31 and 40 cells from 9 WT and NOX2-Tg mice, respectively; **A**) and LA (n=32 and 39 cells from 8 WT and 11 NOX2-Tg mice; **B**) myocytes was not different between genotypes. Data shown as individual values with median (25^{th} to 75^{th} percentile).

6.3.2 Assessment of diastolic RyR2 Ca^{2+} leak

Diastolic SR Ca^{2+} leak through RyR2 has previously been shown to trigger atrial arrhythmias [218]. Based on the higher incidence of pacing-induced AF in NOX2-Tg mice (shown in Chapter 3), we expected to observe increased diastolic Ca^{2+} leak in isolated NOX2-Tg atrial myocytes. To test this hypothesis, we measured the Ca^{2+} leak through RyR2 in individual RA and LA myocytes using a protocol described by Shannon *et al.* [217], and modified in our laboratory. Cells were field-stimulated at 2 Hz in normal Tyrode solution for at least 30 seconds (until $[Ca^{2+}]_i$ transients reached steady-state) before the bath solution was switched to a Tyrode solution containing 0 Na^+ and 0 Ca^{2+} with or without 1 mmol/L tetracaine. The SR Ca^{2+} leak was quantified as the change in basal Fura-2 fluorescence (corresponding to a change in diastolic $[Ca^{2+}]_i$) in response to tetracaine, which blocks RyR2 Ca^{2+} release causing a shift of Ca^{2+} from the cytosol into the SR (lowering $[Ca^{2+}]_i$ and raising $[Ca^{2+}]_{SR}$) that is proportional to the SR Ca^{2+} leak [217]. A sample raw data trace showing the RyR2 leak measurement protocol is reproduced in Figure 6.1. For more details on the interpretation of the protocol, refer to Section 2.9.2 of Chapter 2.

I first considered the proportion of atrial myocytes that showed some degree of RyR2 Ca^{2+} leak (*e.g.*, $\Delta F/F0 > 0$). In the RA of NOX2-Tg hearts, Ca^{2+} leak was detected in a greater proportion of myocytes compared with WT (11/33 cells (33%) for WT *vs* 23/40 cells (58%) for NOX2-Tg; $P = 0.06$, Fisher's exact test), though not statistically different (Figure 6.6-A). Among those cells with Ca^{2+} leak > 0 (n=11 and 23 cells from WT and NOX2-Tg, respectively), I quantified the absolute tetracaine-dependent shift in $[Ca^{2+}]_i$ and observed no significant difference (P>0.05) between the genotypes (Figure 6.6-B). Similar results were observed when expressing the RyR2 leak as a ratio of the total SR Ca^{2+} load to control for differences in the SR Ca^{2+} content (Figure 6.6-C and Figure 6.6-D). In the LA, the proportion of myocytes with SR Ca^{2+} leak was similar between genotypes (18/32 (56%) for WT *vs* 25/39 (64%) for NOX2-Tg; P=0.63, Fisher's exact test; Figure 6.7-A), however, the amount of diastolic Ca^{2+} leak tended to be smaller in NOX2-Tg LA myocytes ($F_{365/380}$: 0.016, 25th to 75th percentile: 0.006 – 0.0275) compared with WT ($F_{365/380}$: 0.026, 25th to 75th percentile: 0.011 – 0.039, P =0.098, Mann-Whitney U test; Figure 6.7-

B). As shown in Figure 6.4-B, NOX2 overexpression is associated with an increase in the SR Ca^{2+} content in LA myocytes compared with WT cells. Controlling for differences in the SR Ca^{2+} content, the ratio of RyR2 leak to SR load was found to be significantly smaller in NOX2-Tg LA myocytes (1.9%, 25th to 75th percentile: 0.64 – 3.78 for NOX2-Tg *vs* 3.9%, 25th to 75th percentile: 2.3 – 4.7 for WT, P = 0.022, Mann-Whitney U test; Figure 6.7-C). This means that the leak-load relationship was reduced in NOX2-Tg myocytes (Figure 6.7-D).

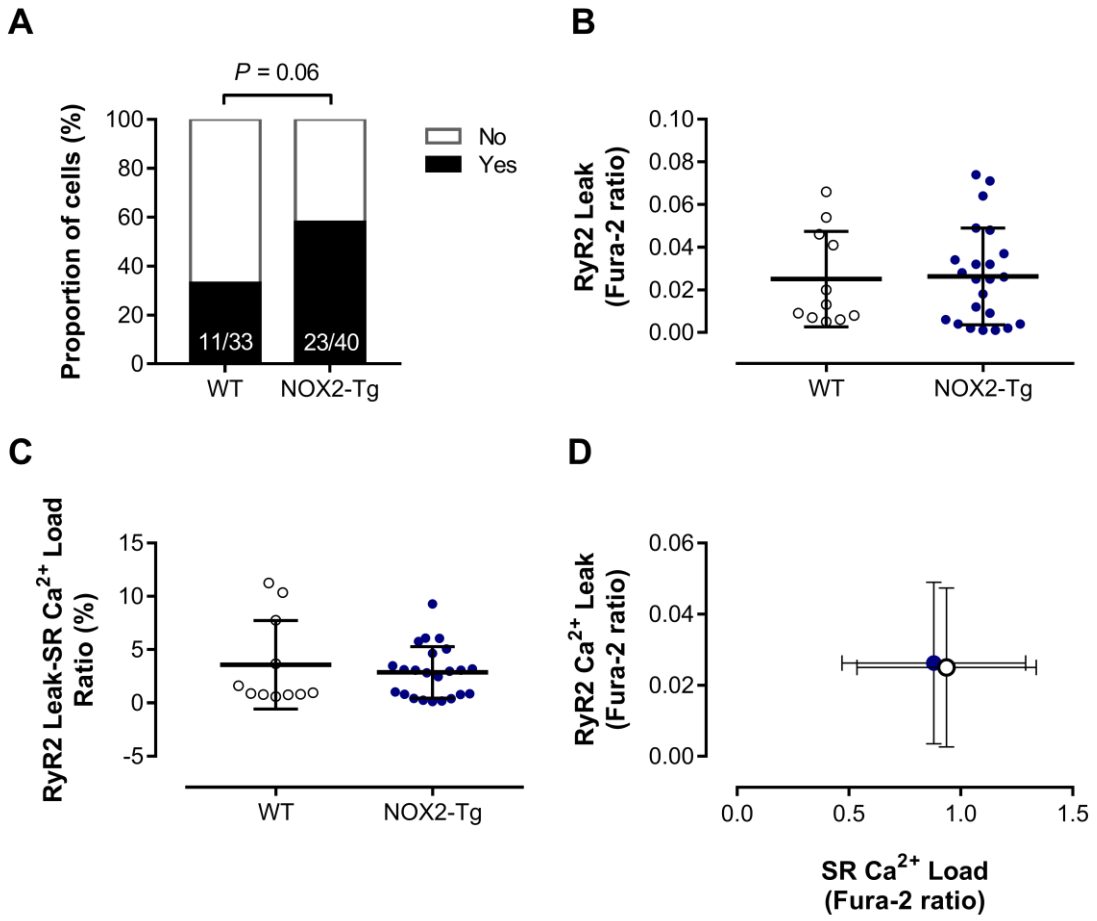

Figure 6.6: Assessment of diastolic SR Ca^{2+} leak and the leak-load relationship in WT and NOX2-Tg RA myocytes. A, The proportion of cells in which Ca^{2+} leak could be observed tended to be higher in NOX2-Tg myocytes (58%, 23/40 cells) compared with WT controls (33%, 11/33 cells), but this did not reach significance (P = 0.06, Fisher's exact). **B,** The tetracaine-induced shift in cytosolic Ca^{2+} (middle) was similar between NOX2-Tg (n = 23 cells from 9 mice) and WT myocytes (n = 11 cells from 9 mice), as was the RyR leak – SR load ratio (**C**) and the leak – load relationship (**D**) (○ – WT; ● – NOX2-Tg). Data shown as individual values with mean ± SD.

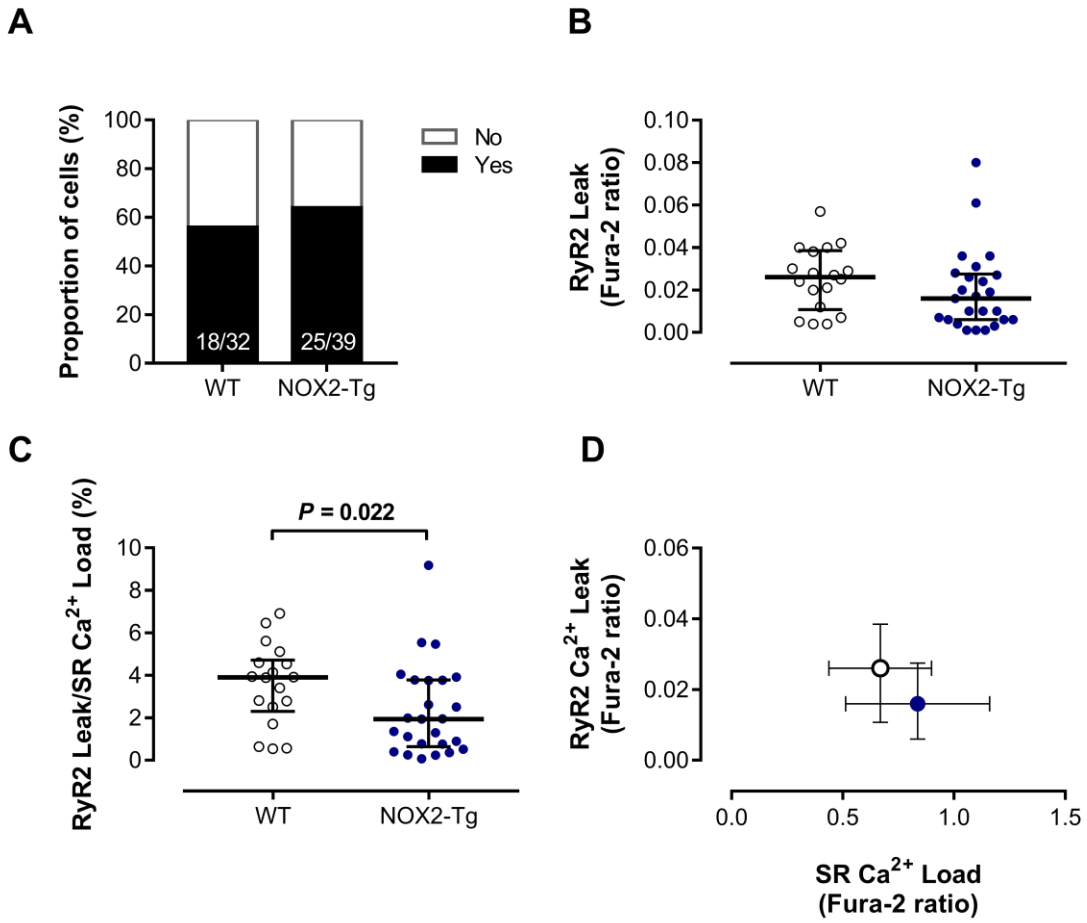

Figure 6.7: Assessment of diastolic SR Ca^{2+} leak and the leak-load relationship in WT and NOX2-Tg LA myocytes. A, The proportion of cells in which Ca^{2+} leak could be observed was not different between NOX2-Tg and WT LA myocytes (P = 0.63, Fisher's exact). **B,** The tetracaine-induced shift in Ca^{2+} was similar between NOX2-Tg (n = 25 cells from 11 mice) and WT myocytes (n = 18 cells from 8 mice; P = 0.1), however, the RyR leak – SR load ratio (**C**) was significantly smaller in NOX2-Tg LA myocytes ($F_{365/380}$: 1.93, 25^{th}-75^{th} percentile: 0.64 – 3.78) compared with WT cells ($F_{365/380}$: 3.94, 25^{th}-75^{th} percentile: 2.3 – 4.7, P = 0.022, Mann Whitney U test) which meant that the leak-load relationship was reduced (**D**) (○ – WT; ● – NOX2-Tg). Data shown as individual values with median ± interquartile range.

6.3.3 Assessment of RyR2 phosphorylation

As RyR2 phosphorylation is known to modify RyR2 channel activity, we investigated whether changes in RyR2 phosphorylation may account for the differences in RyR2 leak observed between NOX2-Tg and WT atrial myocytes. RyR2 phosphorylation status was assessed in WT and NOX2-Tg atrial tissue homogenates using antibodies specific to two of the main phosphorylation sites, Ser2808 and Ser2814, according to the methods described in Section 6.2.2 of this chapter. As shown in Figure 6.8, phosphorylation of Ser2808, thought to be predominantly a target for PKA [262], was similar between WT and NOX2-Tg atria. Similarly, the fraction of RyR2 phosphorylated at Ser2814, which is thought to be controlled by CaMKII [260], was unchanged between the genotypes in both RA (Figure 6.9-A) and LA homogenates (Figure 6.9-B).

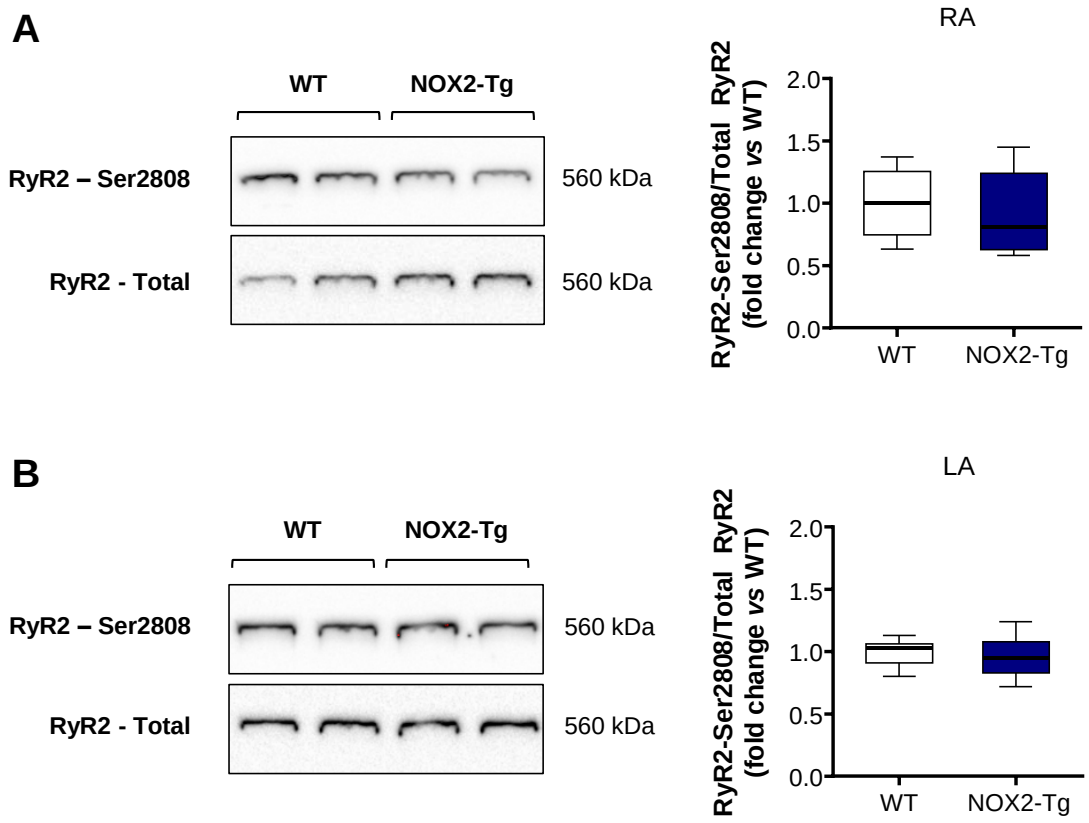

Figure 6.8: RyR2 phosphorylation at Ser2808 is unchanged in NOX2-Tg mice. The fraction of the total RyR2 phosphorylated at Ser2808 was assessed by western blot analysis and found to be similar between WT (ratio: 1.0 ± 0.28, n = 5) and NOX2-Tg RA (ratio: 0.91 ± 0.33, n = 9, $P > 0.05$, **A**) and LA (ratio: 1.0 ± 0.11, n = 7 for WT *vs* 0.95 ± 0.16, n = 9 for NOX2-Tg, $P > 0.05$, **B**) tissue homogenates. Representative western blots from each atrium are shown on the left. Data shown as box and whisker plot: maximum and minimum.

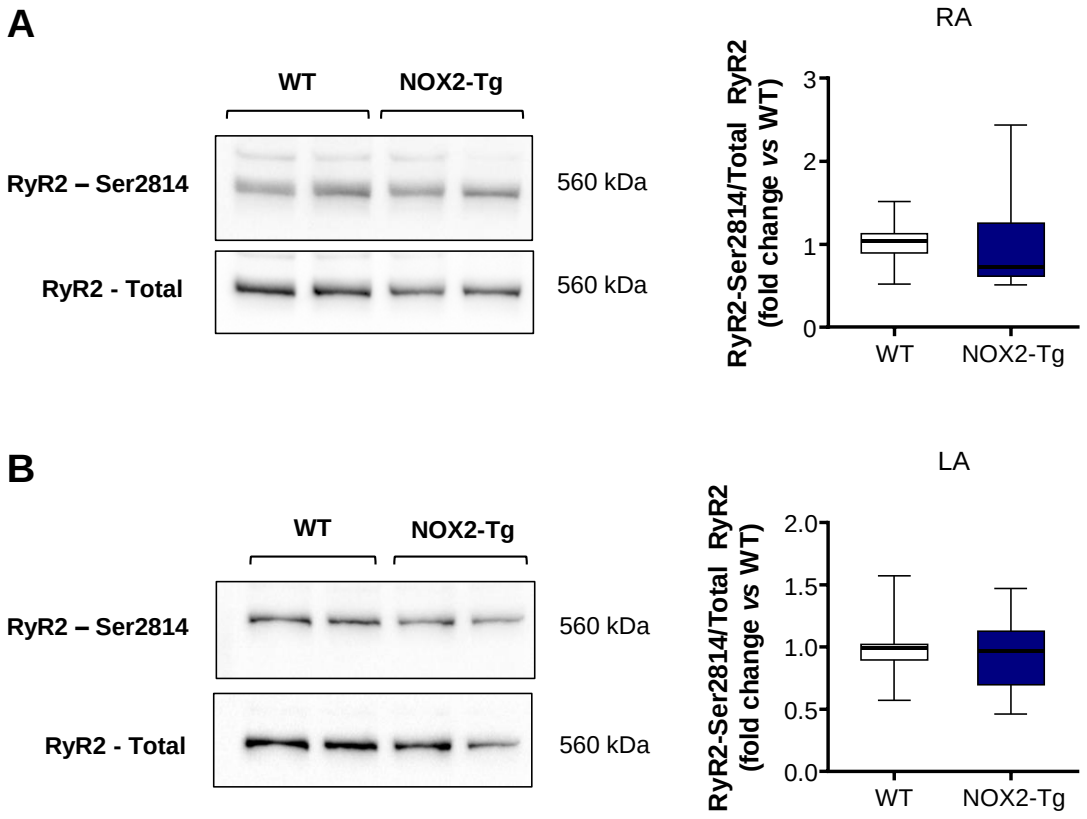

Figure 6.9: RyR2 phosphorylation at Ser2814 is unchanged in NOX2-Tg mice. The fraction of the total RyR2 phosphorylated at Ser2814, thought to be a target for CaMKII, was assessed by western blot analysis and found to be similar between WT (ratio: 1.0 ± 0.21, n = 17) and NOX2-Tg RA (ratio: 0.94 ± 0.48, n = 17, $P > 0.05$, **A**) and LA (ratio: 1.0 ± 0.25, n = 16 for WT *vs* 0.95 ± 0.29, n = 18 for NOX2-Tg, $P > 0.05$, **B**) tissue homogenates. Representative western blots from each atrium are shown on the left. Data shown as box and whisker plot: maximum and minimum.

6.4 Discussion

Diastolic SR Ca^{2+} leak is regarded as an important mechanism in the pathogenesis of AF. Spontaneous Ca^{2+} sparks promote the initiation and propagation of cell-wide Ca^{2+} waves and the elimination of cytosolic Ca^{2+} via NCX generates a depolarizing current which can give rise to delayed afterdepolarizations and spontaneous action potentials. Moreover, a number of studies have demonstrated that NOX2-derived ROS promotes SR Ca^{2+} release through RyR2 and may initiate Ca^{2+}-dependent triggered activity in ventricular myocytes [202, 208]. But does NOX2-derived $O_2^{\cdot -}$ have the same effect in atrial myocytes?

To answer this question, I measured the diastolic leak of Ca^{2+} through RyR2 in atrial myocytes isolated from NOX2-Tg and WT mice, using Ang-II (1 μmol/L) to stimulate ROS production from NOX2. RyR2 leak can be measured globally using whole-cell fluorescence [217] or locally as Ca^{2+} sparks using confocal imaging of fluorescent Ca^{2+} indicators [266]. Santiago *et al.* [267] used both methods simultaneously to measure Ca^{2+} leak in murine ventricular myocytes and showed that although the frequency of Ca^{2+} sparks and the global RyR2-mediated leak rate correlated, Ca^{2+} sparks may only account for about half of the total SR Ca^{2+} leak. The remainder is thought to be made up from non-spark SR Ca^{2+} release events originating from the opening of single or small clusters of RyR2 channels that cause such small, narrow, or brief fluorescent signals as to be indistinguishable from the background noise [267, 268]. Interestingly, Sobie *et al.* [269] suggested this form of Ca^{2+} release to be mediated by un-clustered RyR2 channels in the SR membranes that are more sensitive to phosphorylation (by PKA or CaMKII).

Given that these smaller, non-spark Ca^{2+} release events account for approximately half of the total RyR2 leak, we included them in our study by measuring global SR Ca^{2+} leak using the tetracaine method developed by Shannon *et al.* [217], where SR Ca^{2+} leak is quantified directly as the drop in cytosolic [Ca^{2+}] when RyR2 channels are blocked with tetracaine and trans-sarcolemmal Ca^{2+} fluxes are blocked with a Na^+-free, Ca^{2+}-free extracellular solution. This protocol has also been widely adopted by a number of research groups who showed that RyR2 leak is increased by cytosolic or SR Ca^{2+} overload, channel oxidation [270], or phosphorylation by PKA

or CaMKII, in the context of various cardiac pathologies, including paroxysmal [257] and chronic AF [111, 258].

In this study, right atrial myocytes isolated from NOX2-Tg mice were found to have a similar RyR2 Ca^{2+} leak-SR Ca^{2+} load ratio when compared with cells from WT littermates. Following further subgroup analysis it was noted that a greater proportion of NOX2-Tg right atrial myocytes had 'leaky' RyR2 channels compared with WT myocytes. The significance of this observation is unclear but may reflect an increased propensity for SR Ca^{2+} release. In left atrial myocytes, NOX2 overexpression was associated with a lower RyR2 Ca^{2+} leak-SR Ca^{2+} load ratio, despite an increase in SR Ca^{2+} content. These findings appear to disagree with previous work that studied the effect of NOX2-derived ROS on RyR2 function. For instance, Wagner *et al.* [208] found that NOX2-derived ROS production downstream of Ang-II stimulation increased Ca^{2+} spark frequency and diastolic Ca^{2+} leak (measured as a composite of Ca^{2+} spark frequency, amplitude, and width) in WT ventricular myocytes, but not $gp91^{phox}$-deficient myocytes. Additionally, NOX2-derived ROS production was shown to underlie the increase in RyR2 Ca^{2+} spark rate in ventricular myocytes in response to physiological stretch, and in dystrophic ventricles, augmented NOX2-ROS signalling was found to promote the formation of arrhythmogenic Ca^{2+} waves [202].

An important consideration here is the difference in methodology used to assess RyR2 Ca^{2+} leak. We used the tetracaine-induced drop in diastolic Fura-2 fluorescent ratio as an estimate of diastolic SR Ca^{2+} leak. However, this approach has been suggested to be more appropriate for assessing high leak rates (where SR Ca^{2+} leak limits SR Ca^{2+} load) [271]. Therefore, the amount of Ca^{2+} released through RyR2 in response to NOX2 stimulation in atrial myocytes could be too small to be distinguishable from the background noise of whole-cell fluorescence. The fact that we were not able to detect Ca^{2+} leak in a significant proportion of myocytes (~50% of all myocytes studied) suggests that this may be the case, especially since the presence of Ca^{2+} sparks in quiescent myocytes means that SR Ca^{2+} is never truly zero [255]. This also means that we were underpowered to detect differences in RyR2 leak; sample size calculations determined that we would need approximately 41 myocytes/group, while I was only able to estimate diastolic Ca^{2+} leak in 11 and 18 right and left atrial myocytes, respectively, from WT mice and 23 and 25 right

and left atrial myocytes, respectively, from NOX2-Tg mice. Therefore, recording the formation of spontaneous Ca^{2+} sparks with confocal microscopy could address this limitation and would be useful to corroborate previous findings.

These apparent discrepancies could also be explained by the difference in subcellular structure between atrial and ventricular myocytes (reviewed in refs. [46] and [48]. In particular, the absence of a pronounced t-tubular network in atrial cardiomyocytes may alter the spatial distribution of NOX2 and hence the proximity to RyR2 channels [46, 47]. In ventricular myocytes that have t-tubules, NOX2 is evident on the sarcolemma and at the Z-lines deep inside the cells and has been shown to stimulate junctional RyR2 channels [202, 207], while in the atria, NOX2 may not be close enough to colocalize with RyR2 channels and influence Ca^{2+} release.

Another possibility is that NOX2 is concentrated at a distinct population of RyR2 channels (junctional or non-junctional) such that the RyR2 Ca^{2+} release is highly localized. Since the sarcolemma does not protrude deep into atrial cells, NOX2 is presumably concentrated around the periphery of the cells (similar to the subcellular distribution of atrial L-type Ca^{2+} channels [272] and NCX [46]), and in close apposition with junctional RyR2 channels which form a very small proportion of the total RyR2 population in atrial myocytes [50, 51]. As a consequence, RyR2 Ca^{2+} release in response to NOX2 stimulation may only occur in the immediate sub-sarcolemmal space at the cells' edge. Such spatial information would be difficult to obtain using whole-cell fluorescence, which may have caused an underestimation of SR Ca^{2+} leak in our study, at least in right atrial myocytes. Clearly, additional studies will be required to address these speculations. Nevertheless, they are unlikely to explain the reduced RyR2 leak observed in NOX2-Tg left atrial myocytes.

Spontaneous diastolic SR Ca^{2+} release is mediated by an increase in RyR2 Ca^{2+} sensitivity or an increase in SR Ca^{2+} content, both of which increase the propensity of the channels to open [116, 117]. To assess whether the decrease in RyR2 Ca^{2+} in NOX2-Tg left atrial myocytes depends on a reduction in SR Ca^{2+} content, I also measured SR Ca^{2+} load using caffeine to release the Ca^{2+} in the SR and did not observe a decrease, but rather an increase, in SR Ca^{2+} content. This would suggest that the decrease in SR Ca^{2+} leak is most likely due to a direct effect on RyR2 Ca^{2+} release.

As RyR2 function is known to be modulated by the phosphorylation status of the channel the extent of RyR2 phosphorylation by CaMKII and PKA was investigated. Both CaMKII- and PKA-dependent phosphorylation of RyR2 have previously been shown to enhance RyR2 open probability and the amplitude of diastolic Ca^{2+} leak in AF [111, 258]. The data presented in this chapter show that RyR2 phosphorylation was not different between genotypes at Ser2814 (thought to be a residue specific to CaMKII [260]) or Ser2808 (PKA phosphorylation site [262]). Therefore, differences in RyR2 phosphorylation do not appear to explain the reduced diastolic leak following NOX2 overexpression in left atrial myocytes.

We cannot exclude the possibility that other post-translational modifications contribute to the reduced leak-load relationship. For instance, RyR2 open probability has been shown to be sensitive to redox modifications [153, 264]. This is attributed to the presence of highly reactive cysteine residues whose thiol side chains are able to form disulfide bonds with adjacent thiols or with glutathione in a process termed S-glutathionylation. In general, oxidation of RyR2 thiols enhances, while reduction decreases, channel activity [264]. Previously, NOX2-derived ROS has been shown to promote RyR2 S-glutathionylation and enhance SR Ca^{2+} release in ventricular myocytes [205]. Based on this knowledge, we would expect an increase in RyR2 S-glutathionylation in NOX2-Tg atria which would not explain the observed reduction in diastolic Ca^{2+} leak in left atrial myocytes. Nevertheless, the relative levels of RyR2 S-glutathionylation warrant investigation in these mice.

As part of the RyR2 leak measurement protocol, I also characterized the Ca^{2+}-handling properties of right and left atrial myocytes from NOX2-Tg and WT mice. Previous data from mouse models of NOX2 overexpression or gene deletion have shown that NOX2-dependent $O_2{\cdot}^-$ generation in response to acute Ang-II exposure (1 μmol/L) increases both the influx of Ca^{2+} through L-type Ca^{2+} channels and the SR Ca^{2+} content in isolated ventricular cardiomyocytes, resulting in an increased amplitude and rate of decay of the $[Ca^{2+}]_i$ transient [207, 208]. Similar observations were made in the atrial myocardium. For instance, Ang-II stimulation of WT atrial myocytes produced a significant increase in the $[Ca^{2+}]_i$ transient amplitude and the diastolic $[Ca^{2+}]_i$ concentration that was absent in myocytes treated with apocynin or lacking functional NOX2

(gp91^{phox}-knockout myocytes) [245]. Furthermore, ROS production secondary to Ang-II exposure was associated with an increase in diastolic $[Ca^{2+}]_i$, $[Ca^{2+}]_i$ transient amplitude, and SR Ca^{2+} load that was more pronounced in atrial myocytes from mice with selective gene deletion of Pak1 (p21-activated kinase 1), a serine-threonine kinase that inhibits $O_2^{\cdot -}$ production via NOX2 by preventing the membrane translocation of Rac1 [245].

The data presented in this chapter are somewhat consistent with those reports. For instance, in left atrial cardiomyocytes, NOX2 overexpression was associated with enhanced SR Ca^{2+} loading, although the $[Ca^{2+}]_i$ transient amplitude and tau, as well as the diastolic $[Ca^{2+}]_i$ concentration, remained normal. In the right atria, we did not observe a difference in the diastolic $[Ca^{2+}]_i$ concentration or the SR Ca^{2+} content between NOX2-Tg and WT myocytes, but the amplitude and rate of decay of the $[Ca^{2+}]_i$ transient tended to be enhanced by NOX2 overexpression.

The precise mechanisms underlying these changes in Ca^{2+} handling are unclear. However, a number of studies have demonstrated that NOX2-derived ROS can alter the activity of Ca^{2+}-handling proteins and/or protein kinases that regulate Ca^{2+}-handling proteins and may offer insight into how NOX2 could modify $[Ca^{2+}]_i$ in atrial myocytes. For instance, voltage-clamp studies demonstrated that Ang-II stimulation of WT ventricular cardiomyocytes produced a significant increase in peak I_{CaL} that was absent in gp91^{phox}-deficient myocytes [208]. The mechanism of NOX2-mediated activation of I_{Ca} likely involves activation of PKA and subsequent phosphorylation of the L-type Ca^{2+} channel, since inhibition of PKA with H89 was shown to abolish the Ang-II-dependent increase in peak I_{Ca} [208]. Direct oxidation of the pore-forming α1c subunit of the L-type Ca^{2+} channel has also been described [84], although this has not been linked mechanistically to NOX2.

NOX2-derived ROS has also been suggested to modulate SERCA and NCX function [207, 245]. In the forward mode, NCX controls the rate of cytosolic Ca^{2+} removal by transporting Ca^{2+} ions across the sarcolemma while SERCA pumps Ca^{2+} back into the SR and therefore controls both the rate of intracellular Ca^{2+} removal and the degree of SR Ca^{2+} load (see ref. [31] for review). Using the same NOX2-Tg mouse model, Zhang *et al.* [207] recently found that NOX2-mediated

phosphorylation of PLN leads to increased SERCA activity in left ventricular myocytes, causing more rapid removal of Ca^{2+} from the cytosol into the SR, as evidenced by a faster decay of the Ca^{2+} transient and an increase in SR Ca^{2+} load. DeSantiago *et al.* [245] found that NOX2-dependent ROS production, secondary to Ang-II exposure, was associated with an increase in the rate of decay of the caffeine-evoked Ca^{2+} transient in atrial myocytes, suggesting enhanced NCX function [245].

Based on these studies, we can speculate that the increased SR Ca^{2+} load observed in NOX2-Tg left atrial myocytes could be due to higher Ca^{2+} uptake by SERCA, although we did not observe a difference in PLN phosphorylation between NOX2-Tg and WT myocytes (data not shown). In the absence of any other changes in Ca^{2+} handling (*e.g.,* normal diastolic and systolic Ca^{2+} and tau), it is plausible that a decrease in the opening probability or single channel conductance of RyR2 would lead to an increase in the SR Ca^{2+} content [273, 274], as discussed previously. This hypothesis would be consistent with our data showing a decrease in diastolic Ca^{2+} leak via RyR2.

In NOX2-Tg right atrial myocytes, the increase in the $[Ca^{2+}]_i$ transient amplitude and faster decay of the $[Ca^{2+}]_i$ transient could be due to an increase in I_{CaL} and NCX activity. Increased Ca^{2+} entry provides a greater stimulus for Ca^{2+}-induced Ca^{2+} release by RyR2, resulting in an increased amplitude of the $[Ca^{2+}]_i$ transient. The increase in systolic $[Ca^{2+}]_i$ would be expected to increase Ca^{2+} efflux via NCX, particularly in the absence of any changes in SERCA activity. Indeed, our data showing no difference in PLN phosphorylation (data not shown) or SR Ca^{2+} load between NOX2-Tg and WT right atrial myocytes supports this hypothesis.

In summary, this chapter investigated the effect of NOX2 overexpression on intracellular Ca^{2+} handling and diastolic SR Ca^{2+} leak in isolated atrial myocytes. In right atrial myocytes of NOX-Tg mice, the cytosolic Ca^{2+} transient amplitude and rate of decay tended to be increased compared with WT, with no differences in the SR Ca^{2+} content or fractional release of Ca^{2+}. Direct measurements of SR Ca^{2+} leak revealed no differences in the RyR2 Ca^{2+}-SR Ca^{2+} load ratio between NOX2-Tg and WT myocytes, but the proportion of myocytes with measurable RyR2 leak was greater among NOX2-Tg mice when compared with WT littermates. In contrast,

overexpression of NOX2 in the left atria was associated with reduced diastolic leak of Ca^{2+} through RyR2, despite an increase in SR Ca^{2+} load. Neither CaMKII and/or PKA-dependent phosphorylation of RyR2 at Ser2814 and Ser2808, respectively, were significantly different between WT and NOX2-Tg atrial myocytes.

7 Concluding Remarks

7.1 Summary of Conclusions

It is well appreciated that AF is associated with oxidative stress [5]. Among the different sources of ROS in the myocardium, NOX2-containing NADPH oxidases are a significant source of $O_2^{\cdot -}$ production in atrial myocytes [128]. Previous work in this laboratory demonstrated that a NOX2-mediated increase in $O_2^{\cdot -}$ accompanies AF in patients [128, 138] and animal models of pacing-induced AF [138], and further showed a strong independent association between atrial NOX2 activity and post-operative AF in patients undergoing cardiac surgery [142, 143]. However, direct experimental evidence linking NOX2 activity to the initiation and/or maintenance of AF is lacking. Accordingly, the aim of this thesis was to test the hypothesis that $O_2^{\cdot -}$ released specifically from NOX2 oxidases directly contributes to the development of AF.

The results presented in **Chapter 3** support the conclusion that upregulation of atrial NOX2 expression and related increase in NADPH-stimulated $O_2^{\cdot -}$ production is sufficient to increase AF inducibility in transgenic mice, in the absence of significant alterations in cardiac function. Our data show that mice with myocardial-specific expression of NOX2 have higher levels of NADPH-stimulated $O_2^{\cdot -}$ production and are more susceptible to AF by transesophageal pacing when compared with WT littermates. Cardiac structure and function in NOX2-Tg mice was normal, except for a thickening of the LV posterior wall, which was not previously reported [207].

Under the assumption that the short-term administration of statins can inhibit NOX2 activity [138, 142, 230], the study in **Chapter 4** investigated the effects of atorvastatin on atrial $O_2^{\cdot -}$ production and AF susceptibility in NOX2-Tg mice and WT littermates. Our results show that oral atorvastatin treatment significantly inhibited atrial $O_2^{\cdot -}$ generation in NOX2-Tg but not WT atria, an effect which was found to be independent of cholesterol lowering. These findings are consistent with previous data from Antoniades and colleagues demonstrating that 3-day pre-operative treatment with atorvastatin causes a Rac1-dependent reduction in NADPH-stimulated

$O_2{\cdot}^-$ production in atrial [142] and vascular [230] samples from patients undergoing cardiac surgery, without affecting LDL cholesterol content.

Contrary to what was expected, interference with NOX2-signalling was not associated with a significant reduction in the incidence of pacing-induced AF in NOX2-Tg mice. In Chapter 4, I discussed the possibility that we were underpowered in our comparison of the incidence of AF between groups. In this regard, repeating the transesophageal pacing studies in a larger cohort of mice (*e.g.*, 60 mice/group) may provide a more definitive answer regarding the effect of atorvastatin on AF in these mice. It is also possible that atorvastatin did not specifically inhibit $O_2{\cdot}$ from NOX2 since statins have also been shown to increase NO bioavailability [237] and enhance the activity of endogenous anti-oxidant enzymes [236]; however, the observation that NADPH-stimulated $O_2{\cdot}^-$ production was not reduced in WT atria suggests that this is unlikely to be the case. Nevertheless, it would be worth testing the effect of a different pharmacological modulator of NOX2 activity, such as gp91ds-tat, on pacing-induced AF in these mice, particularly in light of the recently reported STICS randomized clinical trial in 1922 patients showing no discernible benefit of pre-operative statin therapy on post-operative AF [232].

Our data uncovered a significant reduction in the duration of AF with atorvastatin when analysed by two-way ANOVA. This effect was independent of genotype suggesting that it was also independent of NOX2 inhibition, and which is presumably mediated via effects on the atrial effective refractory period (possibly via alterations in I_{CaL} [211]). Consistent with this possible mechanism, atorvastatin significantly prolonged APD50 and APD80 in the left and right atria of both WT and NOX2-Tg mice (data not shown). Statins have also been shown to attenuate AF promotion by causing regression of myocardial inflammation and fibrosis [240]; however, this is unlikely to be the mechanism here as atorvastatin had no effect on atrial inflammation or fibrosis in our mice (data not shown).

Having established that NOX2-Tg mice are more prone to pacing-induced AF, I next investigated the mechanisms underlying this phenotype. Candidate mechanisms for increased AF vulnerability include abbreviated APD [4, 72], increased APD heterogeneity [249], and/or slowed conduction [4]. In **Chapter 5**, a high resolution optical imaging system was implemented as a

platform to study the spatiotemporal characteristics of repolarization and conduction in WT and NOX2-Tg isolated atrial preparations. These experiments were conducted under basal conditions (Krebs-Henseleit solution) and using Ang-II to enhance NOX2 activity. Analysis of optical imaging data revealed no significant differences in APD, APD heterogeneity (spatial and temporal), and conduction velocity between WT and NOX2-Tg atria under any of the conditions examined, suggesting that electrical and structural remodelling are unlikely to underlie the enhanced arrhythmogenesis of NOX2-Tg mice observed in our *in vivo* studies.

Another interpretation of this data is that Ang-II was not efficacious in activating NOX2 activity. Although the effects of Ang-II on NOX2-derived $O_2^{\cdot -}$ production have been validated both acutely in isolated cardiomyocytes [207, 208, 245] as well as chronically by subcutaneous infusion using osmotic mini-pumps *in vivo* [207], this possibility cannot be excluded and is an important limitation of these studies. However, in their study using isolated ventricular myocytes, Wagner *et al.* [208] previously showed that Ang-II-dependent activation of NOX2 was not associated with changes in APD, which is consistent with our data. Nevertheless, it would be important to measure the levels of $O_2^{\cdot -}$ production in Ang-II-treated atrial tissue homogenates from WT and NOX2-Tg mice in order to address this concern.

Another mechanism proposed to account for the increase in the susceptibility to AF is an increase in spontaneous RyR2 Ca^{2+} release [61]. As NOX2-derived $O_2^{\cdot -}$ has been shown to regulate RyR2 activity in ventricular myocytes [202, 208] and in isolated SR vesicles [205], we speculated this might also be the case in the atria. To fully explore the role of NOX2 in RyR2 Ca^{2+} release, I measured the diastolic leak of Ca^{2+} through RyR2 using a protocol established by Shannon *et al.* [217], where RyR2 Ca^{2+} leak is quantified as the basal change in Fura-2 fluorescence (corresponding to a change in diastolic $[Ca^{2+}]_i$) in response to tetracaine. The idea was that if Ca^{2+} flux across the sarcolemma is held constant (by perfusing the cells with a Na^+-free, Ca^{2+}-free solution), then abruptly blocking RyR2 with tetracaine should raise SR Ca^{2+} content and reduce $[Ca^{2+}]_i$, proportional to the amount of RyR2 Ca^{2+} leak [217, 271].

Contrary to what was expected, our studies uncovered a decrease in the leak-load ratio in NOX2-Tg left atrial myocytes when compared with WT. This occurred in the context of increased

SR Ca^{2+} load, which suggests the decrease in SR Ca^{2+} leak is most likely due to a direct effect on RyR2 Ca^{2+} release (since SR Ca^{2+} tends to promote RyR2 Ca^{2+} leak [275]). RyR2 function is known to be modulated by the redox-sensitive kinases PKA and CaMKII [259], as well as channel-associated phosphatases [276]. Therefore, I measured RyR2 phosphorylation in NOX2-Tg and WT left atrial homogenates and found no significant differences in RyR2 phosphorylation at Ser-2814 or Ser-2808. Perhaps this is to be expected, since both hyper- and hypo-phosphorylation of RyR2 have been shown to increase RyR2 Ca^{2+} sensitivity and open probability [257, 276]. In addition to phosphorylation, several oxidative modifications, including S-glutathionylation and S-nitrosylation, have been demonstrated to modify RyR2 channel activity [153, 264, 277] and should be assessed in follow-up work.

In right atrial myocytes, PKA and CaMKII phosphorylation of RyR2 was also unaffected by NOX2 overexpression. This observation supports the fact that the leak-load relationship was similar between NOX2-Tg and WT right atrial myocytes. However, more right atrial myocytes from NOX2-Tg mice tended to have 'leaky' RyR2 channels (*e.g.*, diastolic SR Ca^{2+} leak > 0) compared with WT. Although completely speculative, this may suggest an increased propensity for SR Ca^{2+} release in right atrial myocytes with NOX2 overexpression.

There are important limitations to the approach used to estimate RyR2 Ca^{2+} leak in our study. Measurement of whole-cell fluorescence is useful to estimate global diastolic Ca^{2+} leak (*e.g.*, both Ca^{2+} spark-dependent and independent RyR Ca^{2+} leak [267]) but at the expense of spatial information as it records bulk cytosolic $[Ca^{2+}]_i$. However, NOX2-derived ROS has been shown to promote Ca^{2+} sparks in ventricular myocytes [202, 208], which occur due to the opening of single or small clusters of RyR2 channels. Therefore, it would be useful to record the formation of spontaneous Ca^{2+} sparks in NOX2-Tg and WT atria using confocal microscopy, and to compare differences in Ca^{2+} spark frequency and amplitude.

The tetracaine method for measuring Ca^{2+} leak has also been suggested to be more appropriate for assessing high leak rates [271]. The fact that I was not able to detect Ca^{2+} leak in a significant proportion of myocytes suggests that the amount of RyR2 Ca^{2+} leak observed in atrial myocytes under our experimental conditions (2 Hz field-stimulation and 1.8 mmol/L $[Ca^{2+}]_o$) may

be too small to be distinguished from the background noise of whole-cell fluorescence. Therefore, it is difficult to conclude whether or not NOX2-derived $O_2^{\cdot -}$ alters RyR2 Ca^{2+} release in atrial myocytes and future work would be to corroborate our findings using other measures of RyR2 Ca^{2+} leak (*e.g.,* Ca^{2+} sparks).

As part of the RyR2 leak measurement protocol, I also assessed intracellular $[Ca^{2+}]_i$ transient morphology and observed no differences between WT and NOX2-Tg myocytes in the left atria, but there was a trend towards increased amplitude and rate of decay of the $[Ca^{2+}]_i$ transient in right atrial myocytes of NOX2-Tg mice compared with WT, as reported previously [207, 245]. NOX2-derived ROS has been demonstrated to increase I_{CaL} [208] and NCX activity [245] which could account for the observed differences in Ca^{2+} transient morphology between WT and NOX2-Tg atrial myocytes, particularly in the absence of differences in SR Ca^{2+} uptake (no differences in SR Ca^{2+} load or PLN phosphorylation).

Of note, enhanced NCX underlies the development of delayed afterdepolarizations and spontaneous action potentials and may contribute to the enhanced atrial arrhythmogenesis observed in NOX2-Tg mice. The caffeine transient decay time provides an indirect estimate of NCX-mediated Ca^{2+} removal (and thus activity) but was not measured because the cells were perfused with a Na^+-free Ca^{2+}-free solution. Future work will be to measure I_{NCX} and to record the formation of spontaneous arrhythmogenic depolarizations in isolated atrial myocytes. It should be mentioned that I did not observe any spontaneous action potentials during my optical imaging studies (data not shown); however, spontaneous action potentials are typically provoked by rapid atrial pacing which was not performed.

In summary, the data presented in this thesis show that myocardial NOX2 overexpression and related increase in NADPH-stimulated $O_2^{\cdot -}$ production are associated with increased AF susceptibility *in vivo* in a mouse model. Enhanced atrial NOX2 activity does not promote electrophysiologic or structural remodelling of the atria, but rather alters intracellular Ca^{2+} handling and RyR2 channel function. Future work will be required to corroborate these findings and to determine whether Ca^{2+} mishandling promotes atrial arrhythmogenesis in NOX2-Tg mice.

7.2 Limitations

Overall, our studies contribute to the evidence implicating elevated myocardial ROS production in the development of AF. However, there remain a number of limitations that need to be acknowledged. First, the mouse model used in our experiments is a humanized mouse that expresses the human *NOX2* gene in the heart. Understandably, investigating the behaviour of the human NOX2 protein within a murine environment could be problematic; since NOX2 is a multi-subunit enzyme, it is entirely possible that the human NOX2 protein may not interact with the corresponding mouse $p22^{phox}$, $p40^{phox}$, $p67^{phox}$, $p47^{phox}$ and/or Rac proteins to produce a functional enzyme (despite sharing ~96% amino acid sequence homology). This concern was addressed by measuring the amount of $O_2{\cdot}^-$ produced in the atria of NOX2-Tg mice, which was found to be higher than WT, suggesting that overexpression of the human NOX2 gene produces a functional enzymatic complex.

Furthermore, there are inherent limitations to mouse models when studying human myocardial biology which are relevant to our studies: (1) the mouse atria has a very short action potential (tens *vs* hundreds of milliseconds in human atria) owing to differences in the densities of ionic currents and expression of ion channels; (2) extensive t-tubule networks are present in human atria but are generally absent in atrial myocytes of small mammals, including mice [278], which can have a significant impact on intracellular Ca^{2+} handling; and (3) unlike humans, mice do not develop AF spontaneously and thus require a trigger (atrial burst stimulation) for AF to occur, suggesting that the underlying substrate is different. Therefore, the conclusions drawn above cannot be directly applied to humans.

List of References

1. Boyett MR, Honjo H, Kodama I. The sinoatrial node, a heterogeneous pacemaker structure. *Cardiovasc Res* 2000,**47**:658-687.
2. Hurst JW, Fuster V, Walsh RA, Harrington RA. *Hurst's the heart*. 13th ed. New York: McGraw-Hill; 2011.
3. Rhoades R, Bell DR. *Medical physiology : principles for clinical medicine*. 4th ed. Philadelphia, Pa. ; London: Wolters Kluwer, Lippincott Williams & Wilkins; 2013.
4. Heijman J, Voigt N, Nattel S, Dobrev D. Cellular and molecular electrophysiology of atrial fibrillation initiation, maintenance, and progression. *Circ Res* 2014,**114**:1483-1499.
5. Simon JN, Ziberna K, Casadei B. Compromised redox homeostasis, altered nitroso-redox balance, and therapeutic possibilities in atrial fibrillation. *Cardiovasc Res* 2016,**109**:510-518.
6. Kirchhof P, Benussi S, Kotecha D, Ahlsson A, Atar D, Casadei B, *et al.* 2016 ESC Guidelines for the management of atrial fibrillation developed in collaboration with EACTS. *Eur Heart J* 2016,**37**:2893-2962.
7. Kirchhof P, Benussi S, Kotecha D, Ahlsson A, Atar D, Casadei B, *et al.* 2016 ESC Guidelines for the management of atrial fibrillation developed in collaboration with EACTS. *Europace* 2016,**18**:1609-1678.
8. January CT, Wann LS, Alpert JS, Calkins H, Cigarroa JE, Cleveland JC, Jr., *et al.* 2014 AHA/ACC/HRS guideline for the management of patients with atrial fibrillation: a report of the American College of Cardiology/American Heart

Association Task Force on Practice Guidelines and the Heart Rhythm Society. *J Am Coll Cardiol* 2014,**64**:e1-76.

9. Nattel S, Dobrev D. Electrophysiological and molecular mechanisms of paroxysmal atrial fibrillation. *Nat Rev Cardiol* 2016,**13**:575-590.
10. Benjamin EJ, Levy D, Vaziri SM, D'Agostino RB, Belanger AJ, Wolf PA. Independent risk factors for atrial fibrillation in a population-based cohort. The Framingham Heart Study. *JAMA* 1994,**271**:840-844.
11. Lip GY, Kakar P, Watson T. Atrial fibrillation--the growing epidemic. *Heart* 2007,**93**:542-543.
12. Lip GY, Brechin CM, Lane DA. The global burden of atrial fibrillation and stroke: a systematic review of the epidemiology of atrial fibrillation in regions outside North America and Europe. *Chest* 2012,**142**:1489-1498.
13. Chugh SS, Havmoeller R, Narayanan K, Singh D, Rienstra M, Benjamin EJ, *et al.* Worldwide epidemiology of atrial fibrillation: a Global Burden of Disease 2010 Study. *Circulation* 2014,**129**:837-847.
14. Wolf PA, Benjamin EJ, Belanger AJ, Kannel WB, Levy D, D'Agostino RB. Secular trends in the prevalence of atrial fibrillation: The Framingham Study. *Am Heart J* 1996,**131**:790-795.
15. Go AS, Hylek EM, Phillips KA, Chang Y, Henault LE, Selby JV, *et al.* Prevalence of diagnosed atrial fibrillation in adults: national implications for rhythm management and stroke prevention: the AnTicoagulation and Risk Factors in Atrial Fibrillation (ATRIA) Study. *JAMA* 2001,**285**:2370-2375.
16. Miyasaka Y, Barnes ME, Gersh BJ, Cha SS, Bailey KR, Abhayaratna WP, *et al.* Secular trends in incidence of atrial fibrillation in Olmsted County, Minnesota,

1980 to 2000, and implications on the projections for future prevalence. *Circulation* 2006,**114**:119-125.

17. Andrade J, Khairy P, Dobrev D, Nattel S. The clinical profile and pathophysiology of atrial fibrillation: relationships among clinical features, epidemiology, and mechanisms. *Circ Res* 2014,**114**:1453-1468.
18. Schnabel RB, Yin X, Gona P, Larson MG, Beiser AS, McManus DD*, et al.* 50 year trends in atrial fibrillation prevalence, incidence, risk factors, and mortality in the Framingham Heart Study: a cohort study. *Lancet* 2015,**386**:154-162.
19. Sheikh A, Patel NJ, Nalluri N, Agnihotri K, Spagnola J, Patel A, *et al.* Trends in hospitalization for atrial fibrillation: epidemiology, cost, and implications for the future. *Prog Cardiovasc Dis* 2015,**58**:105-116.
20. Dorian P, Jung W, Newman D, Paquette M, Wood K, Ayers GM*, et al.* The impairment of health-related quality of life in patients with intermittent atrial fibrillation: implications for the assessment of investigational therapy. *J Am Coll Cardiol* 2000,**36**:1303-1309.
21. Aliot E, Botto GL, Crijns HJ, Kirchhof P. Quality of life in patients with atrial fibrillation: how to assess it and how to improve it. *Europace* 2014,**16**:787-796.
22. Thrall G, Lane D, Carroll D, Lip GY. Quality of life in patients with atrial fibrillation: a systematic review. *Am J Med* 2006,**119**:448 e441-419.
23. Wolf PA, Abbott RD, Kannel WB. Atrial fibrillation as an independent risk factor for stroke: the Framingham Study. *Stroke* 1991,**22**:983-988.
24. Healey JS, Connolly SJ, Gold MR, Israel CW, Van Gelder IC, Capucci A*, et al.* Subclinical atrial fibrillation and the risk of stroke. *N Engl J Med* 2012,**366**:120-129.

25. Wang TJ, Larson MG, Levy D, Vasan RS, Leip EP, Wolf PA, *et al.* Temporal relations of atrial fibrillation and congestive heart failure and their joint influence on mortality: the Framingham Heart Study. *Circulation* 2003,**107**:2920-2925.

26. Hart RG, Halperin JL. Atrial fibrillation and stroke : concepts and controversies. *Stroke* 2001,**32**:803-808.

27. Ling LH, Kistler PM, Kalman JM, Schilling RJ, Hunter RJ. Comorbidity of atrial fibrillation and heart failure. *Nat Rev Cardiol* 2016,**13**:131-147.

28. Benjamin EJ, Wolf PA, D'Agostino RB, Silbershatz H, Kannel WB, Levy D. Impact of atrial fibrillation on the risk of death: the Framingham Heart Study. *Circulation* 1998,**98**:946-952.

29. Stewart S, Hart CL, Hole DJ, McMurray JJ. A population-based study of the long-term risks associated with atrial fibrillation: 20-year follow-up of the Renfrew/Paisley study. *Am J Med* 2002,**113**:359-364.

30. Andersson T, Magnuson A, Bryngelsson IL, Frobert O, Henriksson KM, Edvardsson N, *et al.* All-cause mortality in 272,186 patients hospitalized with incident atrial fibrillation 1995-2008: a Swedish nationwide long-term case-control study. *Eur Heart J* 2013,**34**:1061-1067.

31. Bers DM. Cardiac excitation-contraction coupling. *Nature* 2002,**415**:198-205.

32. Bartos DC, Grandi E, Ripplinger CM. Ion Channels in the Heart. *Compr Physiol* 2015,**5**:1423-1464.

33. Nerbonne JM, Kass RS. Molecular physiology of cardiac repolarization. *Physiol Rev* 2005,**85**:1205-1253.

34. Berman MF, Camardo JS, Robinson RB, Siegelbaum SA. Single sodium channels from canine ventricular myocytes: voltage dependence and relative rates of activation and inactivation. *J Physiol* 1989,**415**:503-531.

35. Wang Z, Feng J, Shi H, Pond A, Nerbonne JM, Nattel S. Potential molecular basis of different physiological properties of the transient outward K+ current in rabbit and human atrial myocytes. *Circ Res* 1999,**84**:551-561.

36. Feng J, Xu D, Wang Z, Nattel S. Ultrarapid delayed rectifier current inactivation in human atrial myocytes: properties and consequences. *Am J Physiol* 1998,**275**:H1717-1725.

37. Nerbonne JM. Molecular basis of functional voltage-gated K+ channel diversity in the mammalian myocardium. *J Physiol* 2000,**525 Pt 2**:285-298.

38. Mancarella S, Yue Y, Karnabi E, Qu Y, El-Sherif N, Boutjdir M. Impaired Ca2+ homeostasis is associated with atrial fibrillation in the alpha1D L-type Ca2+ channel KO mouse. *Am J Physiol Heart Circ Physiol* 2008,**295**:H2017-2024.

39. Van Wagoner DR, Pond AL, Lamorgese M, Rossie SS, McCarthy PM, Nerbonne JM. Atrial L-type Ca2+ currents and human atrial fibrillation. *Circ Res* 1999,**85**:428-436.

40. Bou-Abboud E, Li H, Nerbonne JM. Molecular diversity of the repolarizing voltage-gated K+ currents in mouse atrial cells. *J Physiol* 2000,**529 Pt 2**:345-358.

41. Xu H, Li H, Nerbonne JM. Elimination of the transient outward current and action potential prolongation in mouse atrial myocytes expressing a dominant negative Kv4 alpha subunit. *J Physiol* 1999,**519 Pt 1**:11-21.

42. Schotten U, Verheule S, Kirchhof P, Goette A. Pathophysiological mechanisms of atrial fibrillation: a translational appraisal. *Physiol Rev* 2011,**91**:265-325.

43. Fabiato A. Calcium-induced release of calcium from the cardiac sarcoplasmic reticulum. *Am J Physiol* 1983,**245**:C1-14.

44. Scriven DR, Dan P, Moore ED. Distribution of proteins implicated in excitation-contraction coupling in rat ventricular myocytes. *Biophys J* 2000,**79**:2682-2691.

45. Cheng H, Lederer WJ. Calcium sparks. *Physiol Rev* 2008,**88**:1491-1545.

46. Bootman MD, Higazi DR, Coombes S, Roderick HL. Calcium signalling during excitation-contraction coupling in mammalian atrial myocytes. *J Cell Sci* 2006,**119**:3915-3925.

47. Bootman MD, Smyrnias I, Thul R, Coombes S, Roderick HL. Atrial cardiomyocyte calcium signalling. *Biochim Biophys Acta* 2011,**1813**:922-934.

48. Smyrnias I, Mair W, Harzheim D, Walker SA, Roderick HL, Bootman MD. Comparison of the T-tubule system in adult rat ventricular and atrial myocytes, and its role in excitation-contraction coupling and inotropic stimulation. *Cell Calcium* 2010,**47**:210-223.

49. Huser J, Lipsius SL, Blatter LA. Calcium gradients during excitation-contraction coupling in cat atrial myocytes. *J Physiol* 1996,**494 (Pt 3)**:641-651.

50. Mackenzie L, Bootman MD, Berridge MJ, Lipp P. Predetermined recruitment of calcium release sites underlies excitation-contraction coupling in rat atrial myocytes. *J Physiol* 2001,**530**:417-429.

51. Hatem SN, Benardeau A, Rucker-Martin C, Marty I, de Chamisso P, Villaz M, *et al.* Different compartments of sarcoplasmic reticulum participate in the excitation-contraction coupling process in human atrial myocytes. *Circ Res* 1997,**80**:345-353.

52. Kockskamper J, Sheehan KA, Bare DJ, Lipsius SL, Mignery GA, Blatter LA. Activation and propagation of Ca(2+) release during excitation-contraction coupling in atrial myocytes. *Biophys J* 2001,**81**:2590-2605.

53. Blatter LA, Kockskamper J, Sheehan KA, Zima AV, Huser J, Lipsius SL. Local calcium gradients during excitation-contraction coupling and alternans in atrial myocytes. *J Physiol* 2003,**546**:19-31.

54. Moe GK, Abildskov JA. Atrial fibrillation as a self-sustaining arrhythmia independent of focal discharge. *Am Heart J* 1959,**58**:59-70.

55. Engelmann T. Ueber den Einfluss der Systole auf der motorische Leitung in der Herzkammer, mit Bemerkungen zur Theorie allorhyth-mischer Herzstorungen. . *Archiv fur die Gesamte Physiologie* 1896,**62**:543-566.

56. Winterberg H. Studien über Herzflimmern. *Pflüger, Archiv für die Gesammte Physiologie des Menschen und der Thiere* 1907,**117**:223-256.

57. Haissaguerre M, Jais P, Shah DC, Takahashi A, Hocini M, Quiniou G, *et al.* Spontaneous initiation of atrial fibrillation by ectopic beats originating in the pulmonary veins. *N Engl J Med* 1998,**339**:659-666.

58. Kistler PM, Fynn SP, Haqqani H, Stevenson IH, Vohra JK, Morton JB, *et al.* Focal atrial tachycardia from the ostium of the coronary sinus: electrocardiographic and electrophysiological characterization and radiofrequency ablation. *J Am Coll Cardiol* 2005,**45**:1488-1493.

59. Lin WS, Tai CT, Hsieh MH, Tsai CF, Lin YK, Tsao HM, *et al.* Catheter ablation of paroxysmal atrial fibrillation initiated by non-pulmonary vein ectopy. *Circulation* 2003,**107**:3176-3183.

60. Tsai CF, Tai CT, Hsieh MH, Lin WS, Yu WC, Ueng KC, *et al.* Initiation of atrial fibrillation by ectopic beats originating from the superior vena cava: electrophysiological characteristics and results of radiofrequency ablation. *Circulation* 2000,**102**:67-74.

61. Nattel S, Dobrev D. The multidimensional role of calcium in atrial fibrillation pathophysiology: mechanistic insights and therapeutic opportunities. *Eur Heart J* 2012,**33**:1870-1877.

62. Katra RP, Laurita KR. Cellular mechanism of calcium-mediated triggered activity in the heart. *Circ Res* 2005,**96**:535-542.

63. January CT, Riddle JM. Early afterdepolarizations: mechanism of induction and block. A role for L-type Ca2+ current. *Circ Res* 1989,**64**:977-990.

64. Ming Z, Nordin C, Aronson RS. Role of L-type calcium channel window current in generating current-induced early afterdepolarizations. *J Cardiovasc Electrophysiol* 1994,**5**:323-334.

65. Mayer AG. Rhythmical pulsation in Scyphomedusae. In:
Carnegie Institution of Washington. Publication, no. 47; 1906. pp. 1-62.

66. Mines GR. On dynamic equilibrium in the heart. *J Physiol* 1913,**46**:349-383.

67. Allessie MA, Bonke FI, Schopman FJ. Circus movement in rabbit atrial muscle as a mechanism of tachycardia. III. The "leading circle" concept: a new model of circus movement in cardiac tissue without the involvement of an anatomical obstacle. *Circ Res* 1977,**41**:9-18.

68. Comtois P, Kneller J, Nattel S. Of circles and spirals: bridging the gap between the leading circle and spiral wave concepts of cardiac reentry. *Europace* 2005,**7 Suppl 2**:10-20.

69. Moe GK, Rheinboldt WC, Abildskov JA. A Computer Model of Atrial Fibrillation. *Am Heart J* 1964,**67**:200-220.

70. Allessie MA, Lammers W, Bonke FIM, Hollen J. Experimental evaluation of Moe's multiple wavelet hypothesis of atrial fibrillation. In: *Cardiac Electrophysiology and Arrhythmias*. Edited by Zipes DP, Jalife J: Grune {&} Stratton; 1985. pp. 265-276.

71. Konings KT, Kirchhof CJ, Smeets JR, Wellens HJ, Penn OC, Allessie MA. High-density mapping of electrically induced atrial fibrillation in humans. *Circulation* 1994,**89**:1665-1680.

72. Wijffels MC, Kirchhof CJ, Dorland R, Allessie MA. Atrial fibrillation begets atrial fibrillation. A study in awake chronically instrumented goats. *Circulation* 1995,**92**:1954-1968.

73. Daoud EG, Bogun F, Goyal R, Harvey M, Man KC, Strickberger SA, *et al.* Effect of atrial fibrillation on atrial refractoriness in humans. *Circulation* 1996,**94**:1600-1606.

74. Franz MR, Karasik PL, Li C, Moubarak J, Chavez M. Electrical remodeling of the human atrium: similar effects in patients with chronic atrial fibrillation and atrial flutter. *J Am Coll Cardiol* 1997,**30**:1785-1792.

75. Bosch RF, Zeng X, Grammer JB, Popovic K, Mewis C, Kuhlkamp V. Ionic mechanisms of electrical remodeling in human atrial fibrillation. *Cardiovasc Res* 1999,**44**:121-131.

76. Skasa M, Jungling E, Picht E, Schondube F, Luckhoff A. L-type calcium currents in atrial myocytes from patients with persistent and non-persistent atrial fibrillation. *Basic Res Cardiol* 2001,**96**:151-159.

77. Barana A, Matamoros M, Dolz-Gaiton P, Perez-Hernandez M, Amoros I, Nunez M, *et al.* Chronic atrial fibrillation increases microRNA-21 in human atrial myocytes decreasing L-type calcium current. *Circ Arrhythm Electrophysiol* 2014,**7**:861-868.

78. Lai LP, Su MJ, Lin JL, Lin FY, Tsai CH, Chen YS, *et al.* Down-regulation of L-type calcium channel and sarcoplasmic reticular Ca(2+)-ATPase mRNA in human atrial fibrillation without significant change in the mRNA of ryanodine receptor,

calsequestrin and phospholamban: an insight into the mechanism of atrial electrical remodeling. *J Am Coll Cardiol* 1999,**33**:1231-1237.

79. Van Gelder IC, Brundel BJ, Henning RH, Tuinenburg AE, Tieleman RG, Deelman L, *et al.* Alterations in gene expression of proteins involved in the calcium handling in patients with atrial fibrillation. *J Cardiovasc Electrophysiol* 1999,**10**:552-560.

80. Brundel BJ, van Gelder IC, Henning RH, Tuinenburg AE, Deelman LE, Tieleman RG, *et al.* Gene expression of proteins influencing the calcium homeostasis in patients with persistent and paroxysmal atrial fibrillation. *Cardiovasc Res* 1999,**42**:443-454.

81. Christ T, Boknik P, Wohrl S, Wettwer E, Graf EM, Bosch RF, *et al.* L-type Ca2+ current downregulation in chronic human atrial fibrillation is associated with increased activity of protein phosphatases. *Circulation* 2004,**110**:2651-2657.

82. Qi XY, Yeh YH, Xiao L, Burstein B, Maguy A, Chartier D, *et al.* Cellular signaling underlying atrial tachycardia remodeling of L-type calcium current. *Circ Res* 2008,**103**:845-854.

83. Greiser M, Halaszovich CR, Frechen D, Boknik P, Ravens U, Dobrev D, *et al.* Pharmacological evidence for altered src kinase regulation of I (Ca,L) in patients with chronic atrial fibrillation. *Naunyn Schmiedebergs Arch Pharmacol* 2007,**375**:383-392.

84. Carnes CA, Janssen PM, Ruehr ML, Nakayama H, Nakayama T, Haase H, *et al.* Atrial glutathione content, calcium current, and contractility. *J Biol Chem* 2007,**282**:28063-28073.

85. Gaborit N, Steenman M, Lamirault G, Le Meur N, Le Bouter S, Lande G, *et al.* Human atrial ion channel and transporter subunit gene-expression remodeling

associated with valvular heart disease and atrial fibrillation. *Circulation* 2005,**112**:471-481.

86. Yue L, Melnyk P, Gaspo R, Wang Z, Nattel S. Molecular mechanisms underlying ionic remodeling in a dog model of atrial fibrillation. *Circ Res* 1999,**84**:776-784.

87. Caballero R, de la Fuente MG, Gomez R, Barana A, Amoros I, Dolz-Gaiton P, *et al.* In humans, chronic atrial fibrillation decreases the transient outward current and ultrarapid component of the delayed rectifier current differentially on each atria and increases the slow component of the delayed rectifier current in both. *J Am Coll Cardiol* 2010,**55**:2346-2354.

88. Pandit SV, Berenfeld O, Anumonwo JM, Zaritski RM, Kneller J, Nattel S, *et al.* Ionic determinants of functional reentry in a 2-D model of human atrial cells during simulated chronic atrial fibrillation. *Biophys J* 2005,**88**:3806-3821.

89. Xia M, Jin Q, Bendahhou S, He Y, Larroque MM, Chen Y, *et al.* A Kir2.1 gain-of-function mutation underlies familial atrial fibrillation. *Biochem Biophys Res Commun* 2005,**332**:1012-1019.

90. Workman AJ, Kane KA, Rankin AC. The contribution of ionic currents to changes in refractoriness of human atrial myocytes associated with chronic atrial fibrillation. *Cardiovasc Res* 2001,**52**:226-235.

91. Brandt MC, Priebe L, Bohle T, Sudkamp M, Beuckelmann DJ. The ultrarapid and the transient outward K(+) current in human atrial fibrillation. Their possible role in postoperative atrial fibrillation. *J Mol Cell Cardiol* 2000,**32**:1885-1896.

92. Burstein B, Nattel S. Atrial fibrosis: mechanisms and clinical relevance in atrial fibrillation. *J Am Coll Cardiol* 2008,**51**:802-809.

93. Morillo CA, Klein GJ, Jones DL, Guiraudon CM. Chronic rapid atrial pacing. Structural, functional, and electrophysiological characteristics of a new model of sustained atrial fibrillation. *Circulation* 1995,**91**:1588-1595.

94. Nattel S. Defining "culprit mechanisms" in arrhythmogenic cardiac remodeling. *Circ Res* 2004,**94**:1403-1405.

95. Nguyen BL, Fishbein MC, Chen LS, Chen PS, Masroor S. Histopathological substrate for chronic atrial fibrillation in humans. *Heart Rhythm* 2009,**6**:454-460.

96. Chimenti C, Russo MA, Carpi A, Frustaci A. Histological substrate of human atrial fibrillation. *Biomed Pharmacother* 2010,**64**:177-183.

97. Goette A, Juenemann G, Peters B, Klein HU, Roessner A, Huth C, *et al.* Determinants and consequences of atrial fibrosis in patients undergoing open heart surgery. *Cardiovasc Res* 2002,**54**:390-396.

98. Saito T, Tamura K, Uchida D, Saito T, Togashi M, Nitta T, *et al.* Histopathological features of the resected left atrial appendage as predictors of recurrence after surgery for atrial fibrillation in valvular heart disease. *Circ J* 2007,**71**:70-78.

99. Xu J, Cui G, Esmailian F, Plunkett M, Marelli D, Ardehali A, *et al.* Atrial extracellular matrix remodeling and the maintenance of atrial fibrillation. *Circulation* 2004,**109**:363-368.

100. Nakajima H, Nakajima HO, Salcher O, Dittie AS, Dembowsky K, Jing S, *et al.* Atrial but not ventricular fibrosis in mice expressing a mutant transforming growth factor-beta(1) transgene in the heart. *Circ Res* 2000,**86**:571-579.

101. Verheule S, Sato T, Everett Tt, Engle SK, Otten D, Rubart-von der Lohe M, *et al.* Increased vulnerability to atrial fibrillation in transgenic mice with selective atrial fibrosis caused by overexpression of TGF-beta1. *Circ Res* 2004,**94**:1458-1465.

102. Li D, Fareh S, Leung TK, Nattel S. Promotion of atrial fibrillation by heart failure in dogs: atrial remodeling of a different sort. *Circulation* 1999,**100**:87-95.

103. Spach MS, Boineau JP. Microfibrosis produces electrical load variations due to loss of side-to-side cell connections: a major mechanism of structural heart disease arrhythmias. *Pacing Clin Electrophysiol* 1997,**20**:397-413.

104. Spach MS, Dolber PC. Relating extracellular potentials and their derivatives to anisotropic propagation at a microscopic level in human cardiac muscle. Evidence for electrical uncoupling of side-to-side fiber connections with increasing age. *Circ Res* 1986,**58**:356-371.

105. Davis LM, Kanter HL, Beyer EC, Saffitz JE. Distinct gap junction protein phenotypes in cardiac tissues with disparate conduction properties. *J Am Coll Cardiol* 1994,**24**:1124-1132.

106. Burstein B, Comtois P, Michael G, Nishida K, Villeneuve L, Yeh YH, *et al.* Changes in connexin expression and the atrial fibrillation substrate in congestive heart failure. *Circ Res* 2009,**105**:1213-1222.

107. Sawaya SE, Rajawat YS, Rami TG, Szalai G, Price RL, Sivasubramanian N, *et al.* Downregulation of connexin40 and increased prevalence of atrial arrhythmias in transgenic mice with cardiac-restricted overexpression of tumor necrosis factor. *Am J Physiol Heart Circ Physiol* 2007,**292**:H1561-1567.

108. Dupont E, Ko Y, Rothery S, Coppen SR, Baghai M, Haw M, *et al.* The gap-junctional protein connexin40 is elevated in patients susceptible to postoperative atrial fibrillation. *Circulation* 2001,**103**:842-849.

109. Nao T, Ohkusa T, Hisamatsu Y, Inoue N, Matsumoto T, Yamada J, *et al.* Comparison of expression of connexin in right atrial myocardium in patients with

chronic atrial fibrillation versus those in sinus rhythm. *Am J Cardiol* 2003,**91**:678-683.

110. Kostin S, Klein G, Szalay Z, Hein S, Bauer EP, Schaper J. Structural correlate of atrial fibrillation in human patients. *Cardiovasc Res* 2002,**54**:361-379.

111. Voigt N, Li N, Wang Q, Wang W, Trafford AW, Abu-Taha I, *et al.* Enhanced sarcoplasmic reticulum Ca2+ leak and increased Na+-Ca2+ exchanger function underlie delayed afterdepolarizations in patients with chronic atrial fibrillation. *Circulation* 2012,**125**:2059-2070.

112. Faggioni M, Savio-Galimberti E, Venkataraman R, Hwang HS, Kannankeril PJ, Darbar D, *et al.* Suppression of spontaneous ca elevations prevents atrial fibrillation in calsequestrin 2-null hearts. *Circ Arrhythm Electrophysiol* 2014,**7**:313-320.

113. Chelu MG, Sarma S, Sood S, Wang S, van Oort RJ, Skapura DG, *et al.* Calmodulin kinase II-mediated sarcoplasmic reticulum Ca2+ leak promotes atrial fibrillation in mice. *J Clin Invest* 2009,**119**:1940-1951.

114. El-Armouche A, Boknik P, Eschenhagen T, Carrier L, Knaut M, Ravens U, *et al.* Molecular determinants of altered Ca2+ handling in human chronic atrial fibrillation. *Circulation* 2006,**114**:670-680.

115. Lukyanenko V, Gyorke I, Gyorke S. Regulation of calcium release by calcium inside the sarcoplasmic reticulum in ventricular myocytes. *Pflugers Arch* 1996,**432**:1047-1054.

116. Satoh H, Blatter LA, Bers DM. Effects of [Ca2+]i, SR Ca2+ load, and rest on Ca2+ spark frequency in ventricular myocytes. *Am J Physiol* 1997,**272**:H657-668.

117. Zalk R, Lehnart SE, Marks AR. Modulation of the ryanodine receptor and intracellular calcium. *Annu Rev Biochem* 2007,**76**:367-385.

118. Voigt N, Heijman J, Wang Q, Chiang DY, Li N, Karck M, *et al.* Cellular and molecular mechanisms of atrial arrhythmogenesis in patients with paroxysmal atrial fibrillation. *Circulation* 2014,**129**:145-156.

119. Yeh YH, Wakili R, Qi XY, Chartier D, Boknik P, Kaab S, *et al.* Calcium-handling abnormalities underlying atrial arrhythmogenesis and contractile dysfunction in dogs with congestive heart failure. *Circ Arrhythm Electrophysiol* 2008,**1**:93-102.

120. Shan J, Xie W, Betzenhauser M, Reiken S, Chen BX, Wronska A, *et al.* Calcium leak through ryanodine receptors leads to atrial fibrillation in 3 mouse models of catecholaminergic polymorphic ventricular tachycardia. *Circ Res* 2012,**111**:708-717.

121. Vest JA, Wehrens XH, Reiken SR, Lehnart SE, Dobrev D, Chandra P, *et al.* Defective cardiac ryanodine receptor regulation during atrial fibrillation. *Circulation* 2005,**111**:2025-2032.

122. Zimmet JM, Hare JM. Nitroso-redox interactions in the cardiovascular system. *Circulation* 2006,**114**:1531-1544.

123. Murphy MP. How mitochondria produce reactive oxygen species. *Biochem J* 2009,**417**:1-13.

124. Kowaltowski AJ, de Souza-Pinto NC, Castilho RF, Vercesi AE. Mitochondria and reactive oxygen species. *Free Radic Biol Med* 2009,**47**:333-343.

125. Nishino T, Okamoto K, Eger BT, Pai EF, Nishino T. Mammalian xanthine oxidoreductase - mechanism of transition from xanthine dehydrogenase to xanthine oxidase. *FEBS J* 2008,**275**:3278-3289.

126. Kelley EE, Khoo NK, Hundley NJ, Malik UZ, Freeman BA, Tarpey MM. Hydrogen peroxide is the major oxidant product of xanthine oxidase. *Free Radic Biol Med* 2010,**48**:493-498.

127. Berry CE, Hare JM. Xanthine oxidoreductase and cardiovascular disease: molecular mechanisms and pathophysiological implications. *J Physiol* 2004,**555**:589-606.

128. Kim YM, Guzik TJ, Zhang YH, Zhang MH, Kattach H, Ratnatunga C, *et al.* A myocardial Nox2 containing NAD(P)H oxidase contributes to oxidative stress in human atrial fibrillation. *Circ Res* 2005,**97**:629-636.

129. Babior BM, Lambeth JD, Nauseef W. The neutrophil NADPH oxidase. *Arch Biochem Biophys* 2002,**397**:342-344.

130. Simon JN, Duglan D, Casadei B, Carnicer R. Nitric oxide synthase regulation of cardiac excitation-contraction coupling in health and disease. *J Mol Cell Cardiol* 2014,**73**:80-91.

131. Vasquez-Vivar J. Tetrahydrobiopterin, superoxide, and vascular dysfunction. *Free Radic Biol Med* 2009,**47**:1108-1119.

132. Fridovich I. Superoxide radical and superoxide dismutases. *Annu Rev Biochem* 1995,**64**:97-112.

133. McCord JM, Fridovich I. Superoxide dismutase. An enzymic function for erythrocuprein (hemocuprein). *J Biol Chem* 1969,**244**:6049-6055.

134. Santos CX, Anilkumar N, Zhang M, Brewer AC, Shah AM. Redox signaling in cardiac myocytes. *Free Radic Biol Med* 2011,**50**:777-793.

135. Ullrich V, Kissner R. Redox signaling: bioinorganic chemistry at its best. *J Inorg Biochem* 2006,**100**:2079-2086.

136. Mihm MJ, Yu F, Carnes CA, Reiser PJ, McCarthy PM, Van Wagoner DR, *et al.* Impaired myofibrillar energetics and oxidative injury during human atrial fibrillation. *Circulation* 2001,**104**:174-180.

137. Dudley SC, Jr., Hoch NE, McCann LA, Honeycutt C, Diamandopoulos L, Fukai T, *et al.* Atrial fibrillation increases production of superoxide by the left atrium and left atrial appendage: role of the NADPH and xanthine oxidases. *Circulation* 2005,**112**:1266-1273.

138. Reilly SN, Jayaram R, Nahar K, Antoniades C, Verheule S, Channon KM, *et al.* Atrial sources of reactive oxygen species vary with the duration and substrate of atrial fibrillation: implications for the antiarrhythmic effect of statins. *Circulation* 2011,**124**:1107-1117.

139. Zhang J, Youn JY, Kim AY, Ramirez RJ, Gao L, Ngo D, *et al.* NOX4-Dependent Hydrogen Peroxide Overproduction in Human Atrial Fibrillation and HL-1 Atrial Cells: Relationship to Hypertension. *Front Physiol* 2012,**3**:140.

140. Sakabe M, Fujiki A, Sakamoto T, Nakatani Y, Mizumaki K, Inoue H. Xanthine oxidase inhibition prevents atrial fibrillation in a canine model of atrial pacing-induced left ventricular dysfunction. *J Cardiovasc Electrophysiol* 2012,**23**:1130-1135.

141. Mayr M, Yusuf S, Weir G, Chung YL, Mayr U, Yin X, *et al.* Combined metabolomic and proteomic analysis of human atrial fibrillation. *J Am Coll Cardiol* 2008,**51**:585-594.

142. Antoniades C, Demosthenous M, Reilly S, Margaritis M, Zhang MH, Antonopoulos A, *et al.* Myocardial redox state predicts in-hospital clinical outcome after cardiac surgery effects of short-term pre-operative statin treatment. *J Am Coll Cardiol*,**59**:60-70.

143. Kim YM, Kattach H, Ratnatunga C, Pillai R, Channon KM, Casadei B. Association of atrial nicotinamide adenine dinucleotide phosphate oxidase activity with the

development of atrial fibrillation after cardiac surgery. *J Am Coll Cardiol* 2008,**51**:68-74.

144. Cai H, Li Z, Goette A, Mera F, Honeycutt C, Feterik K, *et al.* Downregulation of endocardial nitric oxide synthase expression and nitric oxide production in atrial fibrillation: potential mechanisms for atrial thrombosis and stroke. *Circulation* 2002,**106**:2854-2858.

145. Adam O, Frost G, Custodis F, Sussman MA, Schafers HJ, Bohm M, *et al.* Role of Rac1 GTPase activation in atrial fibrillation. *J Am Coll Cardiol* 2007,**50**:359-367.

146. Han W, Fu S, Wei N, Xie B, Li W, Yang S, *et al.* Nitric oxide overproduction derived from inducible nitric oxide synthase increases cardiomyocyte apoptosis in human atrial fibrillation. *Int J Cardiol* 2008,**130**:165-173.

147. Chang JP, Chen MC, Liu WH, Yang CH, Chen CJ, Chen YL, *et al.* Atrial myocardial nox2 containing NADPH oxidase activity contribution to oxidative stress in mitral regurgitation: potential mechanism for atrial remodeling. *Cardiovasc Pathol* 2011,**20**:99-106.

148. Youn JY, Zhang J, Zhang Y, Chen H, Liu D, Ping P, *et al.* Oxidative stress in atrial fibrillation: an emerging role of NADPH oxidase. *J Mol Cell Cardiol* 2013,**62**:72-79.

149. Carnes CA, Chung MK, Nakayama T, Nakayama H, Baliga RS, Piao S, *et al.* Ascorbate attenuates atrial pacing-induced peroxynitrite formation and electrical remodeling and decreases the incidence of postoperative atrial fibrillation. *Circ Res* 2001,**89**:E32-38.

150. Rodrigo R, Korantzopoulos P, Cereceda M, Asenjo R, Zamorano J, Villalabeitia E, *et al.* A randomized controlled trial to prevent post-operative atrial fibrillation by antioxidant reinforcement. *J Am Coll Cardiol* 2013,**62**:1457-1465.

151. Wolke C, Bukowska A, Goette A, Lendeckel U. Redox control of cardiac remodeling in atrial fibrillation. *Biochim Biophys Acta* 2015,**1850**:1555-1565.

152. Donoso P, Sanchez G, Bull R, Hidalgo C. Modulation of cardiac ryanodine receptor activity by ROS and RNS. *Front Biosci (Landmark Ed)* 2011,**16**:553-567.

153. Xu L, Eu JP, Meissner G, Stamler JS. Activation of the cardiac calcium release channel (ryanodine receptor) by poly-S-nitrosylation. *Science* 1998,**279**:234-237.

154. Cutler MJ, Plummer BN, Wan X, Sun QA, Hess D, Liu H, *et al.* Aberrant S-nitrosylation mediates calcium-triggered ventricular arrhythmia in the intact heart. *Proc Natl Acad Sci U S A* 2012,**109**:18186-18191.

155. Xie W, Santulli G, Reiken SR, Yuan Q, Osborne BW, Chen BX, *et al.* Mitochondrial oxidative stress promotes atrial fibrillation. *Sci Rep* 2015,**5**:11427.

156. Purohit A, Rokita AG, Guan X, Chen B, Koval OM, Voigt N, *et al.* Oxidized Ca(2+)/calmodulin-dependent protein kinase II triggers atrial fibrillation. *Circulation* 2013,**128**:1748-1757.

157. Rossi F, Zatti M. Biochemical aspects of phagocytosis in polymorphonuclear leucocytes. NADH and NADPH oxidation by the granules of resting and phagocytizing cells. *Experientia* 1964,**20**:21-23.

158. Babior BM, Kipnes RS, Curnutte JT. Biological defense mechanisms. The production by leukocytes of superoxide, a potential bactericidal agent. *J Clin Invest* 1973,**52**:741-744.

159. Bedard K, Krause KH. The NOX family of ROS-generating NADPH oxidases: physiology and pathophysiology. *Physiol Rev* 2007,**87**:245-313.

160. Cross AR, Segal AW. The NADPH oxidase of professional phagocytes--prototype of the NOX electron transport chain systems. *Biochim Biophys Acta* 2004,**1657**:1-22.

161. Martyn KD, Frederick LM, von Loehneysen K, Dinauer MC, Knaus UG. Functional analysis of Nox4 reveals unique characteristics compared to other NADPH oxidases. *Cell Signal* 2006,**18**:69-82.

162. Serrander L, Cartier L, Bedard K, Banfi B, Lardy B, Plastre O, *et al.* NOX4 activity is determined by mRNA levels and reveals a unique pattern of ROS generation. *Biochem J* 2007,**406**:105-114.

163. Rigutto S, Hoste C, Grasberger H, Milenkovic M, Communi D, Dumont JE, *et al.* Activation of dual oxidases Duox1 and Duox2: differential regulation mediated by camp-dependent protein kinase and protein kinase C-dependent phosphorylation. *J Biol Chem* 2009,**284**:6725-6734.

164. Dinauer MC, Orkin SH, Brown R, Jesaitis AJ, Parkos CA. The glycoprotein encoded by the X-linked chronic granulomatous disease locus is a component of the neutrophil cytochrome b complex. *Nature* 1987,**327**:717-720.

165. Volpp BD, Nauseef WM, Clark RA. Two cytosolic neutrophil oxidase components absent in autosomal chronic granulomatous disease. *Science* 1988,**242**:1295-1297.

166. Parkos CA, Allen RA, Cochrane CG, Jesaitis AJ. Purified cytochrome b from human granulocyte plasma membrane is comprised of two polypeptides with relative molecular weights of 91,000 and 22,000. *J Clin Invest* 1987,**80**:732-742.

167. Harper AM, Chaplin MF, Segal AW. Cytochrome b-245 from human neutrophils is a glycoprotein. *Biochem J* 1985,**227**:783-788.

168. Parkos CA, Dinauer MC, Walker LE, Allen RA, Jesaitis AJ, Orkin SH. Primary structure and unique expression of the 22-kilodalton light chain of human neutrophil cytochrome b. *Proc Natl Acad Sci U S A* 1988,**85**:3319-3323.

169. Kawahara T, Ritsick D, Cheng G, Lambeth JD. Point mutations in the proline-rich region of p22phox are dominant inhibitors of Nox1- and Nox2-dependent reactive oxygen generation. *J Biol Chem* 2005,**280**:31859-31869.

170. Parkos CA, Dinauer MC, Jesaitis AJ, Orkin SH, Curnutte JT. Absence of both the 91kD and 22kD subunits of human neutrophil cytochrome b in two genetic forms of chronic granulomatous disease. *Blood* 1989,**73**:1416-1420.

171. Lapouge K, Smith SJ, Groemping Y, Rittinger K. Architecture of the p40-p47-p67phox complex in the resting state of the NADPH oxidase. A central role for p67phox. *J Biol Chem* 2002,**277**:10121-10128.

172. Park JW, Benna JE, Scott KE, Christensen BL, Chanock SJ, Babior BM. Isolation of a complex of respiratory burst oxidase components from resting neutrophil cytosol. *Biochemistry* 1994,**33**:2907-2911.

173. Groemping Y, Lapouge K, Smerdon SJ, Rittinger K. Molecular basis of phosphorylation-induced activation of the NADPH oxidase. *Cell* 2003,**113**:343-355.

174. Sumimoto H, Hata K, Mizuki K, Ito T, Kage Y, Sakaki Y, *et al.* Assembly and activation of the phagocyte NADPH oxidase. Specific interaction of the N-terminal Src homology 3 domain of p47phox with p22phox is required for activation of the NADPH oxidase. *J Biol Chem* 1996,**271**:22152-22158.

175. Dusi S, Donini M, Rossi F. Mechanisms of NADPH oxidase activation: translocation of p40phox, Rac1 and Rac2 from the cytosol to the membranes in human neutrophils lacking p47phox or p67phox. *Biochem J* 1996,**314 (Pt 2)**:409-412.

176. Heyworth PG, Curnutte JT, Nauseef WM, Volpp BD, Pearson DW, Rosen H, *et al.* Neutrophil nicotinamide adenine dinucleotide phosphate oxidase assembly.

Translocation of p47-phox and p67-phox requires interaction between p47-phox and cytochrome b558. *J Clin Invest* 1991,**87**:352-356.

177. Koshkin V, Lotan O, Pick E. The cytosolic component p47(phox) is not a sine qua non participant in the activation of NADPH oxidase but is required for optimal superoxide production. *J Biol Chem* 1996,**271**:30326-30329.

178. Dang PM, Cross AR, Quinn MT, Babior BM. Assembly of the neutrophil respiratory burst oxidase: a direct interaction between p67PHOX and cytochrome b558 II. *Proc Natl Acad Sci U S A* 2002,**99**:4262-4265.

179. Koga H, Terasawa H, Nunoi H, Takeshige K, Inagaki F, Sumimoto H. Tetratricopeptide repeat (TPR) motifs of p67(phox) participate in interaction with the small GTPase Rac and activation of the phagocyte NADPH oxidase. *J Biol Chem* 1999,**274**:25051-25060.

180. Diekmann D, Abo A, Johnston C, Segal AW, Hall A. Interaction of Rac with p67phox and regulation of phagocytic NADPH oxidase activity. *Science* 1994,**265**:531-533.

181. Cross AR. p40(phox) Participates in the activation of NADPH oxidase by increasing the affinity of p47(phox) for flavocytochrome b(558). *Biochem J* 2000,**349**:113-117.

182. Ambasta RK, Kumar P, Griendling KK, Schmidt HH, Busse R, Brandes RP. Direct interaction of the novel Nox proteins with p22phox is required for the formation of a functionally active NADPH oxidase. *J Biol Chem* 2004,**279**:45935-45941.

183. Banfi B, Clark RA, Steger K, Krause KH. Two novel proteins activate superoxide generation by the NADPH oxidase NOX1. *J Biol Chem* 2003,**278**:3510-3513.

184. Takeya R, Ueno N, Kami K, Taura M, Kohjima M, Izaki T, *et al.* Novel human homologues of p47phox and p67phox participate in activation of superoxide-producing NADPH oxidases. *J Biol Chem* 2003,**278**:25234-25246.

185. Cheng G, Lambeth JD. NOXO1, regulation of lipid binding, localization, and activation of Nox1 by the Phox homology (PX) domain. *J Biol Chem* 2004,**279**:4737-4742.

186. Cheng G, Diebold BA, Hughes Y, Lambeth JD. Nox1-dependent reactive oxygen generation is regulated by Rac1. *J Biol Chem* 2006,**281**:17718-17726.

187. Ueyama T, Geiszt M, Leto TL. Involvement of Rac1 in activation of multicomponent Nox1- and Nox3-based NADPH oxidases. *Mol Cell Biol* 2006,**26**:2160-2174.

188. Kikuchi H, Hikage M, Miyashita H, Fukumoto M. NADPH oxidase subunit, gp91(phox) homologue, preferentially expressed in human colon epithelial cells. *Gene* 2000,**254**:237-243.

189. Cheng G, Ritsick D, Lambeth JD. Nox3 regulation by NOXO1, p47phox, and p67phox. *J Biol Chem* 2004,**279**:34250-34255.

190. Nakano Y, Longo-Guess CM, Bergstrom DE, Nauseef WM, Jones SM, Banfi B. Mutation of the Cyba gene encoding p22phox causes vestibular and immune defects in mice. *J Clin Invest* 2008,**118**:1176-1185.

191. Banfi B, Malgrange B, Knisz J, Steger K, Dubois-Dauphin M, Krause KH. NOX3, a superoxide-generating NADPH oxidase of the inner ear. *J Biol Chem* 2004,**279**:46065-46072.

192. Kiss PJ, Knisz J, Zhang Y, Baltrusaitis J, Sigmund CD, Thalmann R, *et al.* Inactivation of NADPH oxidase organizer 1 results in severe imbalance. *Curr Biol* 2006,**16**:208-213.

193. Clempus RE, Sorescu D, Dikalova AE, Pounkova L, Jo P, Sorescu GP, *et al.* Nox4 is required for maintenance of the differentiated vascular smooth muscle cell phenotype. *Arterioscler Thromb Vasc Biol* 2007,**27**:42-48.

194. von Lohneysen K, Noack D, Jesaitis AJ, Dinauer MC, Knaus UG. Mutational analysis reveals distinct features of the Nox4-p22 phox complex. *J Biol Chem* 2008,**283**:35273-35282.

195. Geiszt M, Kopp JB, Varnai P, Leto TL. Identification of renox, an NAD(P)H oxidase in kidney. *Proc Natl Acad Sci U S A* 2000,**97**:8010-8014.

196. Shiose A, Kuroda J, Tsuruya K, Hirai M, Hirakata H, Naito S, *et al.* A novel superoxide-producing NAD(P)H oxidase in kidney. *J Biol Chem* 2001,**276**:1417-1423.

197. Gorin Y, Ricono JM, Kim NH, Bhandari B, Choudhury GG, Abboud HE. Nox4 mediates angiotensin II-induced activation of Akt/protein kinase B in mesangial cells. *Am J Physiol Renal Physiol* 2003,**285**:F219-229.

198. Inoguchi T, Sonta T, Tsubouchi H, Etoh T, Kakimoto M, Sonoda N, *et al.* Protein kinase C-dependent increase in reactive oxygen species (ROS) production in vascular tissues of diabetes: role of vascular NAD(P)H oxidase. *J Am Soc Nephrol* 2003,**14**:S227-232.

199. Kuroda J, Ago T, Matsushima S, Zhai P, Schneider MD, Sadoshima J. NADPH oxidase 4 (Nox4) is a major source of oxidative stress in the failing heart. *Proc Natl Acad Sci U S A* 2010,**107**:15565-15570.

200. Banfi B, Molnar G, Maturana A, Steger K, Hegedus B, Demaurex N, *et al.* A Ca(2+)-activated NADPH oxidase in testis, spleen, and lymph nodes. *J Biol Chem* 2001,**276**:37594-37601.

201. Banfi B, Tirone F, Durussel I, Knisz J, Moskwa P, Molnar GZ, *et al.* Mechanism of Ca2+ activation of the NADPH oxidase 5 (NOX5). *J Biol Chem* 2004,**279**:18583-18591.

202. Prosser BL, Ward CW, Lederer WJ. X-ROS signaling: rapid mechano-chemo transduction in heart. *Science* 2011,**333**:1440-1445.

203. Kerr JP, Robison P, Shi G, Bogush AI, Kempema AM, Hexum JK, *et al.* Detyrosinated microtubules modulate mechanotransduction in heart and skeletal muscle. *Nat Commun* 2015,**6**:8526.

204. Best A, Ahmed S, Kozma R, Lim L. The Ras-related GTPase Rac1 binds tubulin. *J Biol Chem* 1996,**271**:3756-3762.

205. Donoso P, Finkelstein JP, Montecinos L, Said M, Sanchez G, Vittone L, *et al.* Stimulation of NOX2 in isolated hearts reversibly sensitizes RyR2 channels to activation by cytoplasmic calcium. *J Mol Cell Cardiol* 2014,**68**:38-46.

206. Prosser BL, Ward CW, Lederer WJ. X-ROS signalling is enhanced and graded by cyclic cardiomyocyte stretch. *Cardiovasc Res* 2013,**98**:307-314.

207. Zhang M, Prosser BL, Bamboye MA, Gondim AN, Santos CX, Martin D, *et al.* Contractile Function During Angiotensin-II Activation: Increased Nox2 Activity Modulates Cardiac Calcium Handling via Phospholamban Phosphorylation. *J Am Coll Cardiol* 2015,**66**:261-272.

208. Wagner S, Dantz C, Flebbe H, Azizian A, Sag CM, Engels S, *et al.* NADPH oxidase 2 mediates angiotensin II-dependent cellular arrhythmias via PKA and CaMKII. *J Mol Cell Cardiol* 2014,**75**:206-215.

209. Fauconnier J, Thireau J, Reiken S, Cassan C, Richard S, Matecki S, *et al.* Leaky RyR2 trigger ventricular arrhythmias in Duchenne muscular dystrophy. *Proc Natl Acad Sci U S A* 2010,**107**:1559-1564.

210. Ullrich ND, Fanchaouy M, Gusev K, Shirokova N, Niggli E. Hypersensitivity of excitation-contraction coupling in dystrophic cardiomyocytes. *Am J Physiol Heart Circ Physiol* 2009,**297**:H1992-2003.

211. Shiroshita-Takeshita A, Schram G, Lavoie J, Nattel S. Effect of simvastatin and antioxidant vitamins on atrial fibrillation promotion by atrial-tachycardia remodeling in dogs. *Circulation* 2004,**110**:2313-2319.

212. Zielonka J, Vasquez-Vivar J, Kalyanaraman B. Detection of 2-hydroxyethidium in cellular systems: a unique marker product of superoxide and hydroethidine. *Nat Protoc* 2008,**3**:8-21.

213. Dikalov S, Griendling KK, Harrison DG. Measurement of reactive oxygen species in cardiovascular studies. *Hypertension* 2007,**49**:717-727.

214. Fernandes DC, Goncalves RC, Laurindo FR. Measurement of Superoxide Production and NADPH Oxidase Activity by HPLC Analysis of Dihydroethidium Oxidation. *Methods Mol Biol* 2017,**1527**:233-249.

215. Roussel J, Champeroux P, Roy J, Richard S, Fauconnier J, Le Guennec JY, *et al.* The Complex QT/RR Relationship in Mice. *Sci Rep* 2016,**6**:25388.

216. Kmecova J, Klimas J. Heart rate correction of the QT duration in rats. *Eur J Pharmacol* 2010,**641**:187-192.

217. Shannon TR, Ginsburg KS, Bers DM. Quantitative assessment of the SR Ca2+ leak-load relationship. *Circ Res* 2002,**91**:594-600.

218. Sood S, Chelu MG, van Oort RJ, Skapura D, Santonastasi M, Dobrev D, *et al.* Intracellular calcium leak due to FKBP12.6 deficiency in mice facilitates the inducibility of atrial fibrillation. *Heart Rhythm* 2008,**5**:1047-1054.

219. Overend CL, O'Neill SC, Eisner DA. The effect of tetracaine on stimulated contractions, sarcoplasmic reticulum Ca2+ content and membrane current in isolated rat ventricular myocytes. *J Physiol* 1998,**507 (Pt 3)**:759-769.

220. Xu L, Jones R, Meissner G. Effects of local anesthetics on single channel behavior of skeletal muscle calcium release channel. *J Gen Physiol* 1993,**101**:207-233.

221. Tomek J, Burton RAB, Bub G. Ccoffinn: Automated Wave Tracking in Cultured Cardiac Monolayers. *Biophys J* 2016,**111**:1595-1599.

222. Sikkel MB, Francis DP, Howard J, Gordon F, Rowlands C, Peters NS, *et al.* Hierarchical statistical techniques are necessary to draw reliable conclusions from analysis of isolated cardiomyocyte studies. *Cardiovasc Res* 2017,**113**:1743-1752.

223. Bendall JK, Cave AC, Heymes C, Gall N, Shah AM. Pivotal role of a gp91(phox)-containing NADPH oxidase in angiotensin II-induced cardiac hypertrophy in mice. *Circulation* 2002,**105**:293-296.

224. Wallach TM, Segal AW. Analysis of glycosylation sites on gp91phox, the flavocytochrome of the NADPH oxidase, by site-directed mutagenesis and translation in vitro. *Biochem J* 1997,**321 (Pt 3)**:583-585.

225. Swaminathan PD, Purohit A, Soni S, Voigt N, Singh MV, Glukhov AV, *et al.* Oxidized CaMKII causes cardiac sinus node dysfunction in mice. *J Clin Invest* 2011,**121**:3277-3288.

226. Adam O, Lavall D, Theobald K, Hohl M, Grube M, Ameling S, *et al.* Rac1-induced connective tissue growth factor regulates connexin 43 and N-cadherin expression in atrial fibrillation. *J Am Coll Cardiol* 2010,**55**:469-480.

227. Sirtori CR. The pharmacology of statins. *Pharmacol Res* 2014,**88**:3-11.

228. Cicha I, Schneiderhan-Marra N, Yilmaz A, Garlichs CD, Goppelt-Struebe M. Monitoring the cellular effects of HMG-CoA reductase inhibitors in vitro and ex vivo. *Arterioscler Thromb Vasc Biol* 2004,**24**:2046-2050.

229. Laufs U, Kilter H, Konkol C, Wassmann S, Bohm M, Nickenig G. Impact of HMG CoA reductase inhibition on small GTPases in the heart. *Cardiovasc Res* 2002,**53**:911-920.

230. Antoniades C, Bakogiannis C, Tousoulis D, Reilly S, Zhang MH, Paschalis A, *et al.* Preoperative atorvastatin treatment in CABG patients rapidly improves vein graft redox state by inhibition of Rac1 and NADPH-oxidase activity. *Circulation* 2010,**122**:S66-73.

231. Patti G, Chello M, Candura D, Pasceri V, D'Ambrosio A, Covino E, *et al.* Randomized trial of atorvastatin for reduction of postoperative atrial fibrillation in patients undergoing cardiac surgery: results of the ARMYDA-3 (Atorvastatin for Reduction of MYocardial Dysrhythmia After cardiac surgery) study. *Circulation* 2006,**114**:1455-1461.

232. Zheng Z, Jayaram R, Jiang L, Emberson J, Zhao Y, Li Q, *et al.* Perioperative Rosuvastatin in Cardiac Surgery. *N Engl J Med* 2016,**374**:1744-1753.

233. Chopra V, Wesorick DH, Sussman JB, Greene T, Rogers M, Froehlich JB, *et al.* Effect of perioperative statins on death, myocardial infarction, atrial fibrillation, and length of stay: a systematic review and meta-analysis. *Arch Surg* 2012,**147**:181-189.

234. Fauchier L, Clementy N, Babuty D. Statin therapy and atrial fibrillation: systematic review and updated meta-analysis of published randomized controlled trials. *Curr Opin Cardiol* 2013,**28**:7-18.

235. Kuhn EW, Slottosch I, Wahlers T, Liakopoulos OJ. Preoperative statin therapy for patients undergoing cardiac surgery. *Cochrane Database Syst Rev* 2015:CD008493.

236. Luo JD, Zhang WW, Zhang GP, Zhong BH, Ou HJ. Effects of simvastatin on activities of endogenous antioxidant enzymes and angiotensin-converting enzyme in rat myocardium with pressure-overload cardiac hypertrophy. *Acta Pharmacol Sin* 2002,**23**:124-128.

237. Laufs U, La Fata V, Plutzky J, Liao JK. Upregulation of endothelial nitric oxide synthase by HMG CoA reductase inhibitors. *Circulation* 1998,**97**:1129-1135.

238. Kureishi Y, Luo Z, Shiojima I, Bialik A, Fulton D, Lefer DJ, *et al.* The HMG-CoA reductase inhibitor simvastatin activates the protein kinase Akt and promotes angiogenesis in normocholesterolemic animals. *Nat Med* 2000,**6**:1004-1010.

239. Wakili R, Voigt N, Kaab S, Dobrev D, Nattel S. Recent advances in the molecular pathophysiology of atrial fibrillation. *J Clin Invest* 2011,**121**:2955-2968.

240. Kumagai K, Nakashima H, Saku K. The HMG-CoA reductase inhibitor atorvastatin prevents atrial fibrillation by inhibiting inflammation in a canine sterile pericarditis model. *Cardiovasc Res* 2004,**62**:105-111.

241. Pinho-Gomes AC, Reilly S, Brandes RP, Casadei B. Targeting inflammation and oxidative stress in atrial fibrillation: role of 3-hydroxy-3-methylglutaryl-coenzyme a reductase inhibition with statins. *Antioxid Redox Signal* 2014,**20**:1268-1285.

242. Herron TJ, Lee P, Jalife J. Optical imaging of voltage and calcium in cardiac cells & tissues. *Circ Res*,**110**:609-623.

243. Efimov IR, Nikolski VP, Salama G. Optical imaging of the heart. *Circ Res* 2004,**95**:21-33.

244. Loew LM. Design and Use of Organic Voltage Sensitive Dyes. In: *Membrane Potential Imaging in the Nervous System: Methods and Applications*. Edited by Canepari M, Zecevic D. New York, NY: Springer New York; 2011. pp. 13-23.

245. DeSantiago J, Bare DJ, Varma D, Solaro RJ, Arora R, Banach K. Loss of p21-activated kinase 1 (Pak1) promotes atrial arrhythmic activity. *Heart Rhythm* 2018,**15**:1233-1241.

246. Margaritis M, Sanna F, Lazaros G, Akoumianakis I, Patel S, Antonopoulos AS, *et al.* Predictive value of telomere length on outcome following acute myocardial infarction: evidence for contrasting effects of vascular vs. blood oxidative stress. *Eur Heart J* 2017,**38**:3094-3104.

247. Laughner JI, Ng FS, Sulkin MS, Arthur RM, Efimov IR. Processing and analysis of cardiac optical mapping data obtained with potentiometric dyes. *Am J Physiol Heart Circ Physiol*,**303**:H753-765.

248. Kneller J, Zou R, Vigmond EJ, Wang Z, Leon LJ, Nattel S. Cholinergic atrial fibrillation in a computer model of a two-dimensional sheet of canine atrial cells with realistic ionic properties. *Circ Res* 2002,**90**:E73-87.

249. Di Diego JM, Antzelevitch C. High [Ca2+]o-induced electrical heterogeneity and extrasystolic activity in isolated canine ventricular epicardium. Phase 2 reentry. *Circulation* 1994,**89**:1839-1850.

250. Goette A, Arndt M, Rocken C, Spiess A, Staack T, Geller JC, *et al.* Regulation of angiotensin II receptor subtypes during atrial fibrillation in humans. *Circulation* 2000,**101**:2678-2681.

251. Sun M, Chen M, Dawood F, Zurawska U, Li JY, Parker T, *et al.* Tumor necrosis factor-alpha mediates cardiac remodeling and ventricular dysfunction after pressure overload state. *Circulation* 2007,**115**:1398-1407.

252. Yokoyama T, Sekiguchi K, Tanaka T, Tomaru K, Arai M, Suzuki T, *et al.* Angiotensin II and mechanical stretch induce production of tumor necrosis factor in cardiac fibroblasts. *Am J Physiol* 1999,**276**:H1968-1976.

253. Saba S, Janczewski AM, Baker LC, Shusterman V, Gursoy EC, Feldman AM, *et al.* Atrial contractile dysfunction, fibrosis, and arrhythmias in a mouse model of cardiomyopathy secondary to cardiac-specific overexpression of tumor necrosis factor-{alpha}. *Am J Physiol Heart Circ Physiol* 2005,**289**:H1456-1467.

254. Riley G, Syeda F, Kirchhof P, Fabritz L. An introduction to murine models of atrial fibrillation. *Front Physiol* 2012,**3**:296.

255. Cannell MB, Cheng H, Lederer WJ. The control of calcium release in heart muscle. *Science* 1995,**268**:1045-1049.

256. Hove-Madsen L, Llach A, Bayes-Genis A, Roura S, Rodriguez Font E, Aris A, *et al.* Atrial fibrillation is associated with increased spontaneous calcium release from the sarcoplasmic reticulum in human atrial myocytes. *Circulation* 2004,**110**:1358-1363.

257. Voigt N, Heijman J, Wang Q, Chiang DY, Li N, Karck M, *et al.* Cellular and molecular mechanisms of atrial arrhythmogenesis in patients with paroxysmal atrial fibrillation. *Circulation* 2014,**129**:145-156.

258. Neef S, Dybkova N, Sossalla S, Ort KR, Fluschnik N, Neumann K, *et al.* CaMKII-dependent diastolic SR Ca2+ leak and elevated diastolic Ca2+ levels in right atrial myocardium of patients with atrial fibrillation. *Circ Res* 2010,**106**:1134-1144.

259. Niggli E, Ullrich ND, Gutierrez D, Kyrychenko S, Polakova E, Shirokova N. Posttranslational modifications of cardiac ryanodine receptors: Ca(2+) signaling and EC-coupling. *Biochim Biophys Acta* 2013,**1833**:866-875.

260. Wehrens XH, Lehnart SE, Reiken SR, Marks AR. Ca2+/calmodulin-dependent protein kinase II phosphorylation regulates the cardiac ryanodine receptor. *Circ Res* 2004,**94**:e61-70.

261. Takasago T, Imagawa T, Furukawa K, Ogurusu T, Shigekawa M. Regulation of the cardiac ryanodine receptor by protein kinase-dependent phosphorylation. *J Biochem* 1991,**109**:163-170.

262. Huke S, Bers DM. Ryanodine receptor phosphorylation at Serine 2030, 2808 and 2814 in rat cardiomyocytes. *Biochem Biophys Res Commun* 2008,**376**:80-85.

263. Brillantes AB, Ondrias K, Scott A, Kobrinsky E, Ondriasova E, Moschella MC, *et al.* Stabilization of calcium release channel (ryanodine receptor) function by FK506-binding protein. *Cell* 1994,**77**:513-523.

264. Marengo JJ, Hidalgo C, Bull R. Sulfhydryl oxidation modifies the calcium dependence of ryanodine-sensitive calcium channels of excitable cells. *Biophys J* 1998,**74**:1263-1277.

265. Erickson JR, Joiner ML, Guan X, Kutschke W, Yang J, Oddis CV, *et al.* A dynamic pathway for calcium-independent activation of CaMKII by methionine oxidation. *Cell* 2008,**133**:462-474.

266. Cheng H, Lederer WJ, Cannell MB. Calcium sparks: elementary events underlying excitation-contraction coupling in heart muscle. *Science* 1993,**262**:740-744.

267. Santiago DJ, Curran JW, Bers DM, Lederer WJ, Stern MD, Rios E, *et al.* Ca sparks do not explain all ryanodine receptor-mediated SR Ca leak in mouse ventricular myocytes. *Biophys J* 2010,**98**:2111-2120.

268. Brochet DX, Xie W, Yang D, Cheng H, Lederer WJ. Quarky calcium release in the heart. *Circ Res* 2011,**108**:210-218.

269. Sobie EA, Guatimosim S, Gomez-Viquez L, Song LS, Hartmann H, Saleet Jafri M, *et al.* The Ca 2+ leak paradox and rogue ryanodine receptors: SR Ca 2+ efflux theory and practice. *Prog Biophys Mol Biol* 2006,**90**:172-185.

270. Terentyev D, Gyorke I, Belevych AE, Terentyeva R, Sridhar A, Nishijima Y, *et al.* Redox modification of ryanodine receptors contributes to sarcoplasmic reticulum Ca2+ leak in chronic heart failure. *Circ Res* 2008,**103**:1466-1472.

271. Bers DM. Cardiac sarcoplasmic reticulum calcium leak: basis and roles in cardiac dysfunction. *Annu Rev Physiol* 2014,**76**:107-127.

272. Mackenzie L, Roderick HL, Berridge MJ, Conway SJ, Bootman MD. The spatial pattern of atrial cardiomyocyte calcium signalling modulates contraction. *J Cell Sci* 2004,**117**:6327-6337.

273. Overend CL, Eisner DA, O'Neill SC. The effect of tetracaine on spontaneous Ca2+ release and sarcoplasmic reticulum calcium content in rat ventricular myocytes. *J Physiol* 1997,**502 (Pt 3)**:471-479.

274. Bode EF, Briston SJ, Overend CL, O'Neill SC, Trafford AW, Eisner DA. Changes of SERCA activity have only modest effects on sarcoplasmic reticulum Ca2+ content in rat ventricular myocytes. *J Physiol* 2011,**589**:4723-4729.

275. Zima AV, Bovo E, Bers DM, Blatter LA. Ca(2)+ spark-dependent and -independent sarcoplasmic reticulum Ca(2)+ leak in normal and failing rabbit ventricular myocytes. *J Physiol* 2010,**588**:4743-4757.

276. Terentyev D, Viatchenko-Karpinski S, Gyorke I, Terentyeva R, Gyorke S. Protein phosphatases decrease sarcoplasmic reticulum calcium content by stimulating calcium release in cardiac myocytes. *J Physiol* 2003,**552**:109-118.

277. Sanchez G, Escobar M, Pedrozo Z, Macho P, Domenech R, Hartel S, *et al.* Exercise and tachycardia increase NADPH oxidase and ryanodine receptor-2 activity: possible role in cardioprotection. *Cardiovasc Res* 2008,**77**:380-386.

278. Richards MA, Clarke JD, Saravanan P, Voigt N, Dobrev D, Eisner DA, *et al.* Transverse tubules are a common feature in large mammalian atrial myocytes including human. *Am J Physiol Heart Circ Physiol* 2011,**301**:H1996-2005.